POLITECNICO DI MILANO
DOCTORAL PROGRAMME IN MECHANICAL ENGINEERING

Uncertainty estimation and reduction in digital image correlation measurements

Doctoral Dissertation of:
Paolo Mazzoleni

Supervisor:
Prof. Emanuele Zappa

Tutor:
Prof. Massimiliano Gobbi

The Chair of the Doctoral Program:
Prof. Bianca Maria Colosimo

XXV cycle - 2013

Abstract

Digital image correlation is an increasingly widespread non-contact measurement technology for full field motion and strain estimation.

If, on one hand, the technique is attractive and exploited on and on in a variety of mechanical testing procedures, thanks to its characteristics of contact-less, handiness, flexibility and density of measurable points, on the other hand the approach can not still compete in terms of resulting measurement accuracy with standard state of the art pointwise strain measurements (typically performed through strain gauges). This generally represents a non negligible issue in case of elastic strain evaluation and brittle material testing, where the resulting signal to noise ratio may not be sufficient.

In this work, the problem of uncertainty minimization in digital image correlation measurements is faced from two different points of view is order to propose solutions able to reduce the expected data dispersion.

At first, image blurring is proposed as an effective tool to remove the high spatial frequency components in the acquired images, proven to be misinterpreted by state of the art image correlation algorithms and responsible of producing bias and increasing variability in the computed results.

In particular, the use of a Gaussian low pass filtering is introduced and tuned at first on synthetically generated data simulating increasingly complex motion and strain fields. The stability of the obtained results is numerically verified with respect to the main correlation analysis parameter, the noise level of the acquired data and the characteristic appearance of the framed area. Successively, the obtained results are experimentally validated in rigid motion, uniform deformation and more complex strain fields tests.

In the second part of the work, an innovative fast, cheap and highly repeatable technique for surface texturization, “toner transfer”, is proposed. Highly contrasted randomness in the surface intensity colours (generally referred to as “speckle pattern”) is required by the digital image correlation approach for the displacement and strain fields estimation; this is achieved in the proposed methodology transferring a numerically designed and printed speckle pattern on the final measurement surface by means of a thermo-mechanical process. The capability of the technique to improve the resulting measurement performances (in terms of resolution and accuracy) is quantitatively demonstrated. Furthermore, its flexibility in terms of tested materials, sizes, geometries as long as its suitability in high temperature measurement setup is presented. Thanks to the proposed technology, fully controlled speckle pattern can be generated and consequently the numerical optimization of the random pattern (in terms of minimization of the resulting measurement uncertainty) has been faced. The obtained results have been experimentally proven to be able to reduce the data

dispersion, in particular in case of low signal to noise ratio in the collected images.
Strain measurement uncertainty quantification is by itself a non trivial issue in case of digital image correlation measurements, due to the large number of variables, both in the test setup and in the processing software, strongly influencing this parameter.
In the last part of this work, a fast innovative procedure for “on the field” uncertainty quantification in case of two dimensional digital image correlation setups is presented. The procedure is base on the generation of known fictitious strain fields thanks to out of plane camera-specimen displacements and their fitting by a proper analytic model in order to readily quantify the resulting data dispersion.

Contents

CHAPTER 1

Introduction and state of the art

1.1 Present work: motivations

After about 30 years since the first works carried out in South Carolina, digital image correlation, DIC, is nowadays a widespread vision-based measurement technique for two- and three-dimensional motion and strain full field estimation. Nevertheless, the techniques can still be considered “young” and some work needs to be done in order to make a promising technology a state of the art measurement technique.

In this work, the problem of uncertainty in digital image correlation measurements is faced.

The reason is that data dispersion associated to DIC measurement can not still compete with other state of the art measurement techniques and this is generally a problem in case of elastic strain evaluation and brittle material testing, where the resulting noise level in the collected data is generally too high.

Two different approaches for uncertainty reduction will be presented, developed and validated in this work.

The first one is a preprocessing operation (image blurring) on the acquire data that will be proven to be an effective solution to increase state of the art algorithms performances.

The second approach is an innovative technique for speckle pattern (i.e. the characteristic surface textures of the measurement surface required by digital image correlation) realization. The new technique will be proven to lead to high quality resulting surface appearance, able to maximise the resulting measurement resolution and minimize the associate uncertainty.
On the other hand, the quantification of strain measurement uncertainty in DIC application is by itself a non-trivial, but obviously fundamental, aspect.
In the last part of this thesis an innovative procedure for 2D DIC uncertainty evaluation, based on the so-called fictitious strain method (in plane equivalent deformations resulting by rigid out of plane displacements), will be proposed.

1.2 State of the art: full field strain measurements

Material and structures state of strain quantification due to various static and dynamic mechanical and thermal loading is one of the fundamental tasks of experimental mechanics.
Traditional electric strain gauges are by far the most exploited technique in case local measurements are required, while recently developed fiber optics based transducers on one hand extended the applicability of local measurements in harsh environments and on the other hand introduced innovative solutions for the continuous evaluation of the strains along a 1-D profile (Brillouin technology).
In case full field strain estimation is required, vision based techniques have been developed and applied; these techniques compare a digital image of the measurement surface during the load application with a reference one of the unloaded surface in order to retrieve the surface state of strain.
These techniques can be macroscopically classified into two main groups: interferometric and correlation-based approaches [1].
In the firsts (e.g. holography interferometry, speckle interferometry and moiré interferometry, [2]), the measurement surface, usually characterized by uniform white texture, is lighted by means of structured light (using lasers or fringe projectors). The measure is performed processing the phase difference of the scattered light wave from the test object surface before and after the loading be means of fringe processing and phase analysis.
Digital image correlation, “DIC” [3], refers to a class of non-contacting methods that acquire images of an object, store images in digital format and perform image analysis to extract full-field shape, motion or deformation measurements. The technique, originally developed by a group of researches at the University of South Carolina in the ‘80s [4-9], is known in literature with different names, such as digital speckle correlation [10-11], texture correlation [12], computer-aided speckle interferometry [13,14] and electronic speckle photography [15-18]. In contrast to interferometric approaches, correlation based ones rely on the

inherent textures (naturally present of artificially realized) of the measurement surface and consequently do not require the use of structured light sources. In these methods, the surface deformation is analyzed comparing the gray intensity changes of the object surface in the acquired images.
In the last years, digital image correlation has been widely accepted and commonly used as a powerful and flexible tool for full field deformation measurement in the field of experimental solid mechanics. The technique is characterized, on one hand, by the simplicity of the required measurement setup, basically composed by only an imaging device, monocular in case of 2D DIC or stereo for 3D DIC (versus interferometric approaches, where a structured lighting device and vibration isolated optical platforms are required increasing the setup cost and complexity and strongly limiting field applications, [1]). On the other hand, digital image correlation offers huge flexibility both in terms of spatial resolution and dynamical performances: the same DIC code used to analyze a large scale specimen [19-21] can be applied to micro and nano scale problems, simply substituting the acquisition device (optical microscopes [22-24], laser scanning confocal microscopes [25-26], scanning electron microscopes [27-30], atomic force microscopy [31-33], scanning tunnel microscopes [34-36]) and, providing the availability of a sufficiently fast hardware, strain induced in dynamic and impact tests [37-40] can be quantified by the same algorithm exploited for static analyses. The measurable strain fields range from few tenth of µm/m up to deformation of the measurement surface much higher than 100% [41-44], far beyond the limit of every strain gauge) and, with the right cares, digital image correlation can be easily applied to high temperature tests as well [45-48]. Furthermore, with the constant emergence of high-spatial-resolution and high-time-resolution image acquisition equipment, the DIC method performances increase year by year as a simple consequence of the hardware development.
Nevertheless, digital image correlation still suffers some disadvantages [1]: at low strain level (hundreds of µm/m, such as the first part of elastic zone of a metal) the associated uncertainty can not be considered negligible and in particular can not compete with the one provided on one hand by traditional transducer and, on the other hand, by interferometric approaches. In the first part of this work, two independent and original approaches for uncertainty reduction in digital image correlation measurements will be presented: a theoretical study on the use of image blurring as a way to increase DIC accuracy is proposed and experimentally validated and a new technology to surface texturization (which will lead to the determination of an optimized design for uncertainty reduction) is described.
At the same time, the quantification of the measurement uncertainty itself is a non trivial issue: testing setup characteristics strongly influences the resulting accuracy (problem deeply faced in chapter 7) and, being the digital image

correlation a relative new technique, no standard procedure to quantify this parameter has not been yet introduced nor developed (issue widely discussed in the recent International Workshop on Strain Measurement in Extreme Environments held Glasgow, UK, Aug 2012). An innovative procedure to fast and cheap uncertainty estimation will be here proposed.
In the following of this chapter, the working principle of two-dimensional digital image correlation is described in detail and its generalization for 3D measurements is presented.

1.3 State of the art: two dimensional digital image correlation

The standard implementation of a two-dimensional digital image correlation measurement system is basically composed by three separate steps:

1. Specimen surface and measurement setup preparation
2. Image acquisition of the specimen before (reference) and after loading
3. Digital image processing to estimate the load induced strain

In the following, the setup required characteristics will be discussed and state of the art digital image correlation algorithms will be presented.

1.3.1 Testing layout

The standard measurement layout of a 2D DIC application is reported in Fig. 1-1.

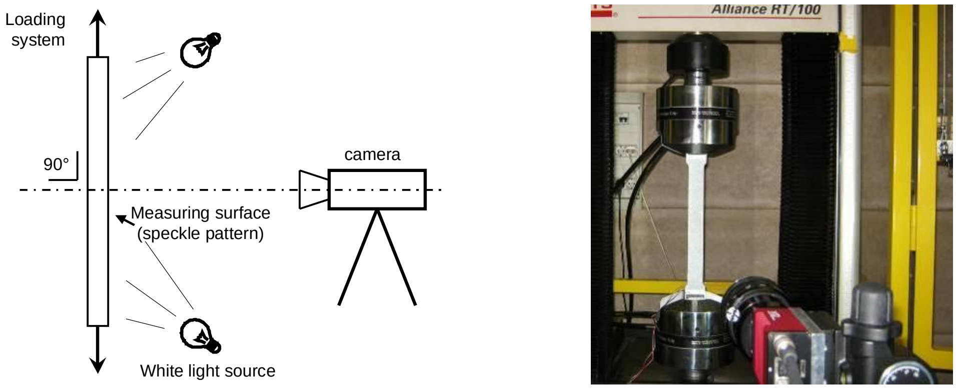

Fig. 1-1 Standard measurement layout for 2D DIC measurements

The flat specimen is mounted in a loading structure (e.g. a standard tensile machine) and lighted by means of white lights. A digital camera frame the specimen, collecting one reference image before the test begins and several image during the test, each of which will be independently analyzed in order the quantify the step by step the full field strain maps. The optical axis of the camera is perpendicular with respect to the measurement surface. This avoids issues related to the so called “fictitious strains” that will be deeply discussed in chapter 2 where an innovative application of pose estimation to camera positioning in digital image correlation tests will be presented.

1.3.2 Surface characteristics

Two-dimensional digital image correlation technique can be exploited only in planar problems: the specimen surface must be flat and no out of plane displacements or strains field can arise during the loading in order to have the method working properly [1, 3].

As mentioned in the introduction, digital image correlation relies on the surface textures of the measurement specimen: the analysis can retrieve the full field displacement map and consequently the surface state of strain comparing the gray intensity changes of the surface in the acquired images. A local point-by-point correspondence among acquired and reference images is estimated by the code in the whole analyzed area in order to compute the motion field.

It is generally not possible to find the correspondence of a single pixel in one image in a second one: the gray value associated to a single pixel can be found in thousands of other pixels in the second image with no unique correspondence. For this reason the analysis considers the correspondence of small neighbourhood around the pixel of interest, the so called “subsets”. In case the measurement surface does not presents textures in its appearance, the method can still not find a correspondence of the selected subset in the two image (the so-called “aperture problem”, [3]): it is the fundamental measurement surface to exhibit a textured appearance. At the same time, the correspondence have to be unique, i.e. the matching process have to find only one valid matching position (“correspondence problem”, [3]). Regular textures (e.g. ordinates grids) have consequently to be avoided.

As a result of the discussed issues, in order to be able to correctly apply digital image correlation, a randomly textured (flat) measurement surface is required. This characteristic can hardly be found in the tested materials and consequently random textures (generally called “speckle pattern”) are artificially applied on the specimen before the test is run (Fig. 1-2).

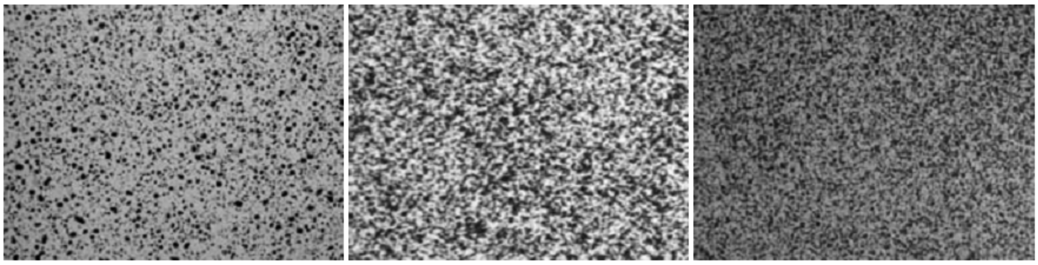

Fig. 1-2 Examples of typical speckle patterns

Spray painting is by far the most commonly exploited procedure to speckle pattern realization but many different techniques were proposed in the years to face particular different scale and material applications [3]. In some cases, the natural textures of the tested material are enough themselves to apply digital image correlation.

The characteristics of the realized speckle pattern deeply influence the quality of digital image correlation analyses results. This aspect will be analyzed in detail in chapter 5, where an innovative technique for speckle pattern realization is proposed and in chapter 6, where the numerical optimization of speckle pattern is faced.

1.3.3 Subset matching

In digital image correlation code, the measured surface displacement field results from the independent tracking of single discrete points. In this paragraph, the single point tracking is described while the full field displacement estimation will be faced in the next paragraph.

In Fig. 1-3 two images of a textured specimen are reported: the first one (reference image) is acquired with no loads applied on the specimen, the second one (deformed image) after uniaxial horizontal loading.

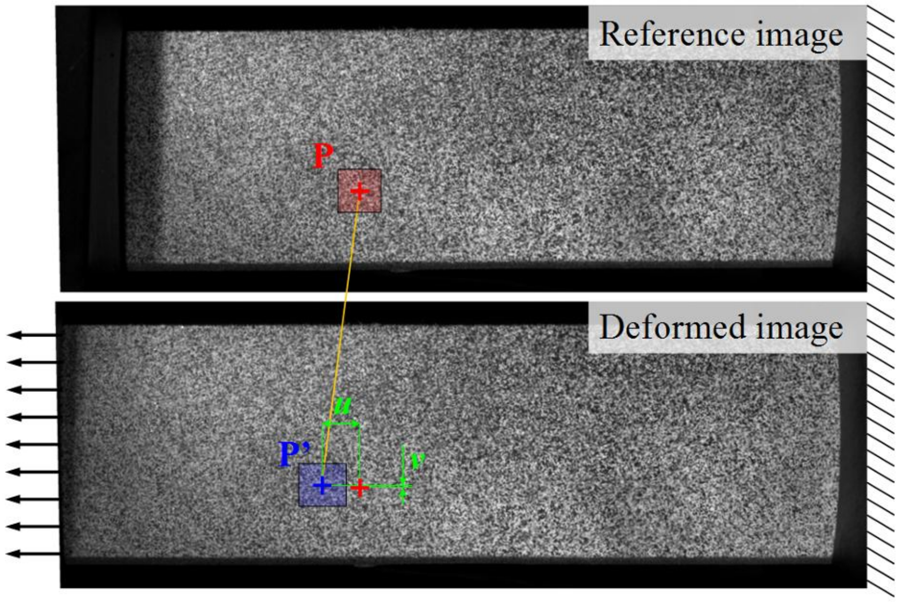

Fig. 1-3 Digital image correlation working principle: point tracking

The point P (centre of the red cross) in the reference is selected and its position in the deformed image (centre of the blue cross) has to be estimated. Once this operation is carried out, the horizontal u and vertical v displacements of the selected point can be easily computed.
As previously explained, in order to avoid the so-called aperture problem, the point P only (with its infinitesimal area) can not be tracked itself but the analysis has to be extended considering a small neighbourhood around. This area, “subset”, is the reported red square in the reference image. The point tracking is therefore an “area matching” problem: to find the new position P’ (after the loading is applied) of the original point P means to identify the area of the deformed image that most resemble the original subset. This area has to be unique, and it is now straightforward to understand the necessity of a random pattern on the measurement surface introduced in the previous paragraph.

Correlation criterions
A quantitative evaluation of the similarity between the original subset and any selected area of the deformed image has to be introduced in order to be able to identify P’ as the position that best matches P in the whole deformed image. This can be done by means of two different (but equivalent) approaches: P’ can be defined as the position that maximizes the cross correlation function between the original subset and the deformed image (CC - cross correlation criterion) or the position able to minimized an bidimensional error function (SSD - sum of squared differences criterion) [49-51].

In detail, being *f* the reference image and *g* the deformed one and (x_i,y_i) and (x'_i,y'_i) the coordinate in their reference system, the two criterion are defined as:

$$C_{CC} = \sum_{i=-M}^{M} \sum_{j=-M}^{M} \left[f(x_i, y_i) g(x_i^{'}, y_i^{'}) \right] \qquad \text{eq 1-1}$$

$$C_{SSD} = \sum_{i=-M}^{M} \sum_{j=-M}^{M} \left[f(x_i, y_i) - g(x_i^{'}, y_i^{'}) \right]^2 \qquad \text{eq 1-2}$$

for a given square subset of size (2M+1) x (2M+1) px.
The presented parameters are proven [3] to be sensitive linear scale in and offset in the environmental light, issues that may easily arise during a standard test, and consequently their normalized version (ZNCC – zero normalized cross correlation and ZNSSD – zero normalized sum of squared differences) are generally preferred:

$$C_{ZNCC} = \sum_{i=-M}^{M} \sum_{j=-M}^{M} \left\{ \frac{\left[f(x_i, y_i) - f_m \right] \times \left[g(x_i^{'}, y_i^{'}) - g_m \right]}{\Delta f \Delta g} \right\} \qquad \text{eq 1-3}$$

$$C_{ZNSSD} = \sum_{i=-M}^{M} \sum_{j=-M}^{M} \left[\frac{f(x_i^{'}, y_i^{'}) - f_m}{\Delta f} - \frac{g(x_i^{'}, y_i^{'}) - g_m}{\Delta g} \right]^2 \qquad \text{eq 1-4}$$

proven be able to successfully tackle lighting related issues.

Shape functions
Serious decorrelation effect may arise in case of high strain fields of specimen rotations in case the area matching is performed rigidly moving the original subset. For this reason, additional degrees of freedom are associated to a subset during the area matching process in addition to the simple in-plane translation.
In details, the original area can be deformed according to the so called “shape functions” [52] or “displacement mapping function” [53].

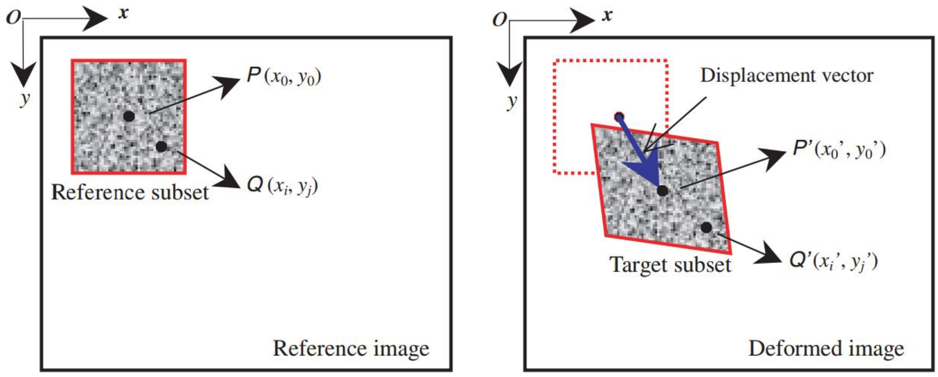

Fig. 1-4 Schematic illustration of a reference square subset before deformation and target (or deformed) subset after deformation [1]

In reference to Fig. 1-4, the subset deformation induced by a shape function can be defined as:

$$\begin{cases} x_i^{'} = x_i + \xi(x_i, yj) \\ y_j^{'} = y_j + \eta(x_i, y_j) \end{cases} \qquad (i, j = -M : M) \qquad \text{eq 1-5}$$

where the ξ and η identify the analytical formulations of the mapping functions. Polynomial second order shape functions, proposed in [53], are by far the most exploited ones; their equation can be expressed as:

$$\begin{cases} \xi(x_i, y_i) = u + u_x \Delta x + u_y \Delta y + \frac{1}{2} u_{xx} \Delta x^2 + \frac{1}{2} u_{yy} \Delta y^2 + u_{xy} \Delta x \Delta y \\ \eta(x_i, y_i) = v + v_x \Delta x + v_y \Delta y + \frac{1}{2} v_{xx} \Delta x^2 + \frac{1}{2} v_{yy} \Delta y^2 + v_{xy} \Delta x \Delta y \end{cases} \qquad \text{eq 1-6}$$

being *u* and *v* are the *x*- and *y*- directional displacement components of the reference subset centre, u_x, u_y, v_x, v_y the first order displacement gradients and u_{xx}, u_{xy}, u_{yy}, v_{xx}, v_{xy} and v_{yy} the second order ones.

Interpolation

The coordinates of point (x'_i, y'_i) in the deformed subset may locate at non-integer pixel positions (i.e. subpixel location). In order to apply a correlation criterion, interpolation of the subset intensity is consequently required. In literature, many different interpolation algorithms has been use to accomplish this task. However, high order interpolation scheme (bicubic or biquintic spline interpolation) has to be preferred [54-55] since they provide higher registration

accuracy and better convergence character of the algorithm with respect to simpler interpolation scheme.
Anyhow, the image interpolation is still a critical step of digital image correlations algorithms: high frequency components of the image intensity (i.e. sharp variations from black to white and vice versa in the speckle patter) may be misinterpreted during the interpolation and alias the measure: the image blurring proposed in chapter 3 and validate in chapter 4 is aimed to deeply investigate this problem and to propose an effective method to get rid of these effects.

Subset matching – initial guess

As mentioned, the goal of digital image correlation algorithm is to provide a motion estimation of the central point of the considered subset with subpixel accuracy. It is generally difficult that the same algorithm exploited to provide an accurate local matching can be able to macroscopically retrieve the position of the tracked area in the deformed image: the matching procedure is consequently split in two separate steps; at first, the macroscopic position of the subset is identified and successively this initial matching is refined in order to achieve subpixel accuracy. In other word, a proper initial guess needs to be provided to the subpixel registration algorithms. For example, iterative Newton-Raphson method (the most commonly used iterative spatial cross-correlation method) is proved to properly converge only if it is initialized not farther than 7 pixel from the right matching position [55].
Usually the relative deformation or rotation between the reference subset and deformed one is quite small. In this case, the initial guess can be easily estimate with 1 pixel accuracy using both spatial domain (e.g. grid methods or alternatively coarse to fine strategies or nested schemes [56] to speed up the operation) or frequency domain [13, 15, 57].
When, at the opposite, the single subset is subjected to large strains or rotations, more complex algorithms need to be exploited (modified nested coarse-fine searching scheme [58] or genetic algorithm [59]). The high computational cost of more complex schemes makes the manual initialization still a considered solution in nowadays codes in case of critical situations.

Subset matching – fine matching

A variety of fine matching algorithms for digital image correlation has been presented in the years in scientific literature [1].
Coarse-to-fine searching strategies, mentioned for the initial guess estimation, can be naturally extended to a subpixel accuracy simply changing the searching step from integer pixel values to fractional pixel values [4, 38]; nevertheless, image interpolation at subpixel values is always required in advance and this results in time consuming approaches.

To overcome this issue, that strongly limits the practical use of digital image correlation, *Peak finding algorithms* have been applied. In these approaches, the selected correlation criterion is computed only at integer pixel value and the interpolation is done on the resulting error (in case of SSD approaches) or cross correlation (when CC criterions are exploited) function, with different analytical fitting functions (biparabolic in [13], quadratic surface in [60], using Fourier expansion in [15]). The main issue related to peak-finding strategies is the intrinsic lack of deformational degrees of freedom of the subset: shape function can not be applied. For this reason they can be exploited only in case of pure rigid motion or very low strain magnitude in the analyzed field.
Iterative spatial domain cross-correlation algorithms are by far the most exploited fine-matching strategies exploited. In these algorithms, the previously presented shape functions are applied on the reference subset in order to iteratively deforming it until the convergence in the identified area of the deformed image is reached. Newton-Rapson method ([61] and [35], where a simplified version of the Hessian matrix is introduce to increase the computation efficiency) is the most used searching strategy, able to correctly tackle the non-linearities of the cost function resulting by the application of non constant mapping function [61].

1.3.4 Displacement field measurement

Once the single subset tracking can be done, its extension to full filed motion estimation is quite trivial. At first, an area to be analyzed (AOI, “area of interest” or “ROI”, region of interest) is manually selected on the reference image (green area in Fig. 1-5a). Within this area, a regular matrix of points to be tracked is identified (red dots of Fig. 1-5a): these points represent the centres of as many subsets. The points are equally spaced in both vertical and horizontal direction: the grid spacing is generally referred to as “step”. The step among subsets is independent from the subsets dimension: the regular grid is commonly built partially overlapping adjacent subsets in order to increase the analysis spatial resolution.
In theory, the previously presented subset tracking procedure (initialization + fine matching) can be applied on every subset and the motion of every point can be estimated (vectors in Fig. 1-5b).
For clarity purposes only few tracked subsets are represented in Fig. 1-5, but in digital image correlation analysis a huge number displacement vectors can be easily retrieve and the results are generally presented as the colour map of Fig. 1-5c where the estimated horizontal displacement is reported. For instance, with an 1Mpx camera (sensor of 1000x1000 pixel, a lot smaller than the standard scientific camera nowadays produced), subset size of 21x21 pixel and step of 7 pixel (which are reasonable DIC analysis parameters), a total of

(1000/7)x(1000/7) ~ 20000 subset are tracked (it is worth to notice that, as explained, this result is independent by the selected subset size).

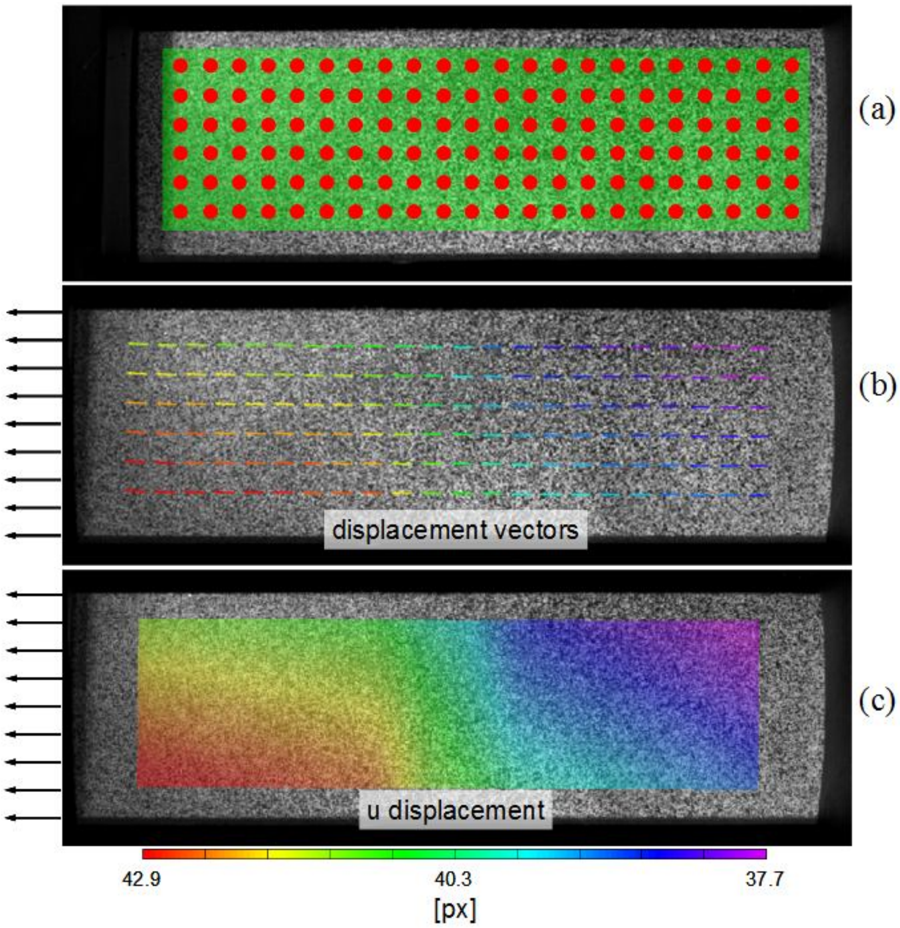

Fig. 1-5 Digital image correlation working principle: full field motion estimation

Due to the high number of subsets to be tracked, the initialization + fine matching procedure is in generally to slow to be applied. For this reason, the initialization is actually performed only on the first subset and the analysis is carried out by rows (or by columns) using a subset fine-matching result as initialization for the adjacent ones [1].

This approach can result critical in case of discontinuities in the displacement field (e.g. associated to cracks in the measurement surface) or high uncertainty the single subset estimated motion (due for example to local poor textures of the speckle pattern). To solve this issue, in [62] a so called “reliability guided” DIC is presented, where the calculation path is guided by the ZNCC coefficient itself: the subsets used to initialize the neighbourhoods are the ones characterized by the highest matching score in the correlation process (i.e. the most reliable ones).

1.3.5 Strain field estimation

With the described approach, the full field displacement of the measurement surface can be estimated with sub-pixel accuracy. However, in many testing applications, full filed strain distributions are more important and desirable.

Theoretically, strains can be estimated simply computing the partial derivatives of the displacements fields. The main issue of such an approach is related the resulting measurement uncertainty: the numerical differentiation process is considered as an unstable and risky operation [63-64], that amplifies the noise of the reference data, leading to measurements characterized by low accuracy (with such an approach DIC could be exploited starting from magnitude of the strain field grater than 1%, far beyond for instance the linear elastic limit of most of the metals [61]).

Smoothing of the computed displacement fields is consequently required before the differentiation process.

In [65] a technique that involves smoothing of the computed displacement fields with the penalty finite element method is proposed, successively improved in [66], while [67] introduced the use of the thin plate smoothing technique to. The noise level of the displacement field is significantly reduced by smoothing operations and consequently the accuracy of the computed strain fields increases. However, these approaches generally result in cumbersome procedures.

The more practical technique for strain estimation is the point-wise local least square fitting advocated in [68] and [69]. The estimated displacement fields are locally fitted by polynomial functions and the strains are estimated starting from the computed regression coefficients.

In a real application, the implementation of similar procedures, and in particular the selection of the width of the smoothing window, has to be carefully considered: from one hand, small windows are unable to properly suppress the noise of the displacement; on the other hand, large strain calculation windows may lead to unreasonable approximation of deformation within the strain calculation window.

1.4 State of the art: three-dimensional digital image correlation

Since two-dimensional digital image correlation requires predominantly in-plane displacements and strains, relatively small out-of-plane motion will change the magnification and introduce errors in the measured in-plane displacement [70, 71, 85]. For the same reason, non planar geometries are difficult to be analyzed using a 2D approach. To solve this limitation of the measurement technique, three-dimensional digital image correlation has been developed, merging the studies carried on in planar digital image correlation with the results of stereoscopy.

As early as the 1960s photogrammetry principles developed for shape and motion measurements were used to estimate plate deflections [72]. From 1970-1990, the concept of digital image correlation for use in photogrammetry was presented [73-76]; in [77] the use of multiple cameras with images of a deforming rectangular grid for surface motion estimation is discussed and in [78-79] a stereo vision system for the measurement of three-dimensional crack tip deformation is developed. Stereo vision methods were successively improved [80] to include the effects of perspective on subset shape and introducing appropriate constrains on the analysis to include the presence of epipolar lines. In parallel, many researches have been carried out in order to optimize the developed stereo system calibrating procedures for digital image correlation tests [81-83].

As a result of the development which have been occurred in recent years, three-dimensional digital image correlation now is being used for a wide range of applications on both large scale and small structures, wide temperature ranges and both static and dynamic tests in all the cases where 3D geometries or out of plane displacements have to be investigate. On the contrary, 2D DIC is nowadays the most widespread approach in all the situations where a plane approximation can be considered acceptable thanks to simplicity of the required measurement setup and the relatively low computational cost of the codes.

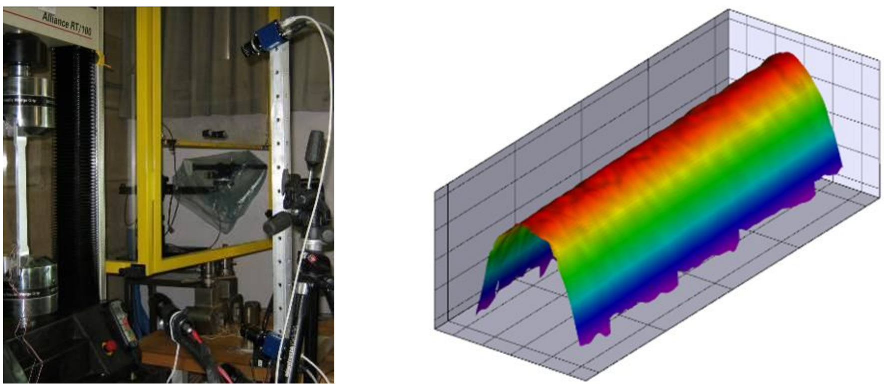

(a) **(b)**

Fig. 1-6 3D digital image correlation: measurement setup (a) and example of the results for a cylindrical specimen

The core of the algorithm, described in the previous paragraph, is shared by the two approaches and the main differences in case 3D systems are exploited are related to the introduction of stereoscopy in the measurement setup and data processing (Fig. 1-6).

1.5 Work layout

In the second chapter, two preliminary activities to the experimental tests of the following chapters will be presented: pose estimation algorithms are studied and qualified and their use in the setup preparation for digital image correlation measurements is proposed in order to assure the orthogonality between the optical axis of the camera and the specimen surface and avoid the rising of fictitious strains in the measurement process; the use of focus algorithms to optimally focus the acquisition hardware is suggested as well.

In chapter three an innovative theoretical study on the use of image blurring as a preprocessing operation to uncertainty reduction in digital image correlation is presented and tested simulating displacement and strain fields of increasing complexity. Furthermore, the stability of the obtained results with respect to data noise, speckle pattern characteristics and DIC analysis parameters is presented.

Chapter four provide the experimental verification of the image blurring preprocessing in two different experiments: rigid in plane motion and standard tensile tests, where the image averaging as an efficient noise reduction technique is also introduced.

In the fifth chapter, an innovative technique, “toner transfer”, for speckle pattern realization is presented: the technique is cheap, fast and flexible in terms of specimen dimensions and geometry, materials and testing temperature. The high quality of the obtained patterns is proven, thus the application of toner transfer is suggested as a way to increasing the signal to noise ratio of the acquired data.

In chapter six, the problem of numerical optimization of the speckle pattern (whose design is proven to be strictly limit measurement uncertainty and resolution in DIC measurements) is faced. Starting from a synthetic index of the quality of the measurement surface, an optimization of the pattern is theoretically carried out and the validity of the study is experimentally proven.

Finally, the last chapter introduces an innovative procedure for uncertainty quantification in two-dimensional digital image correlation setups. The uncertainty of DIC measures is strongly influenced by the testing condition and consequently the use of a fast and easy to apply procedure to quantify this metrological parameter before the execution of the test is suggested.

CHAPTER 2

Preliminary activities: pose estimation and camera focus

2.1 Introduction

Two different studies, preliminary to the experimental activities presented in the following chapters, are here introduced.

In paragraph 2.2 the problem related to the so-called “fictitious strains”, resulting by out of plane displacements in two-dimensional analyses, is described and it is shown how, even with purely planar geometries, it can rises as a result of misalignment of the setup. A procedure, able to assist the experimenter in the setup preparation and thus minimize the errors associated to this issue, is proposed and experimentally validated starting form state of the art pose estimation algorithms.

In paragraph 2.3 the camera focus, aspect that will be fundamental in the research activities describe in chapters 3 and 4, is faced. Starting from state of the art approaches, a software able to provide in real time a feedback on focusing to the experimenter is developed.

2.2 Pose estimation

2.2.1 Fictitious strains related to out-of-plane displacements

As explain in chapter 1, two-dimensional digital image correlation is by far the most widespread image correlation technique for motion and strain measurements. Furthermore, the 3D DIC derives directly from the 2D one and share with it most of its working principles. For this reason, many important studies can be carried out with a two-dimensional analysis, neglecting the complexities related to stereoscopy, and on one hand provide important information about a state of the art technique and, on the other hand, be easily generalized in case of three-dimensional analyses.

The main issue related to two-dimensional techniques is that only planar problems can be studied: the measurement surface has to be planar and, at the same time, motion and strain have to act in the same plane.

If this hypothesis is not verified, issues related to the so called "fictitious strains" arise: out-of-plane displacements are misinterpreted by the algorithm as in-plane strains. This issue can be easily understood by looking at the three images of Fig. 2-1.

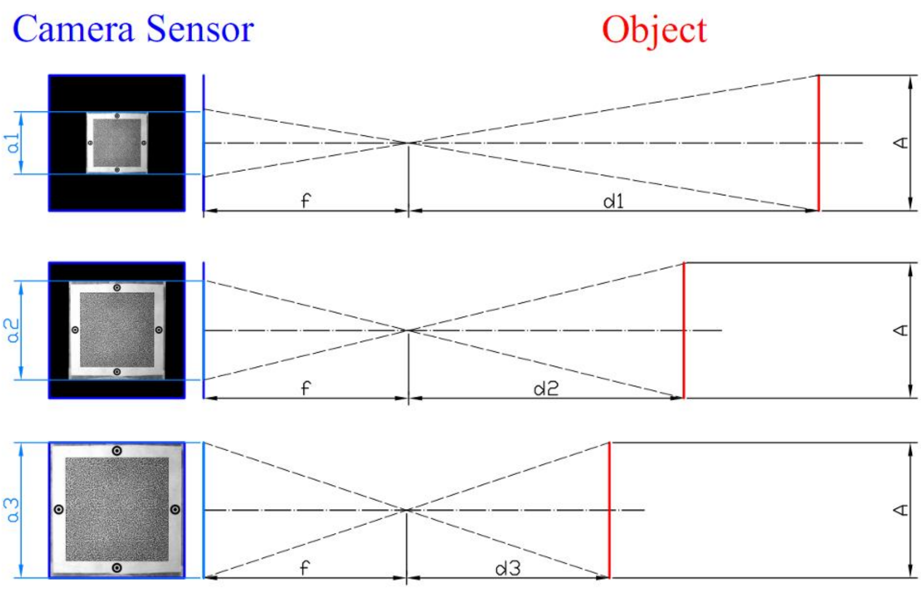

Fig. 2-1 Fictitious strains form out of plane rigid motion

The same object of size equal to $A x A$ mm is placed in front of a camera with a given sensor size and focal length f at three different distances ($f+d1$, $f+d2$, $f+d3$). The object is consequently projected on the sensor with three different scaling factors, resulting in three images where the size of the object framed by the camera decreases by increasing the working distance. The three acquire images are reported on the left of the figure: a 2D technique interprets the out-of-plain rigid motion between one image and the next as an in-plane deformation of the measurement surface.

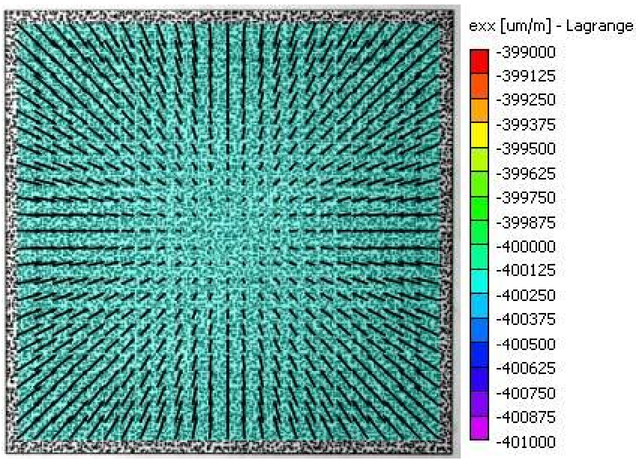

Fig. 2-2 Fictitious uniform strain field form out of plane rigid motion

In Fig. 2-2 the results of the comparison of the first image of Fig. 2-1 with respect to the last one by means of a two-dimensional DIC algorithm are reported: the vectors display an estimated radial motion field as a consequence of the out-of-plane translation and the colour map represents the associated uniform strain field along the horizontal direction. This represents just a simple example of a more complex problem that could arise not only in cases of rigid out-of-plane translation but also as a consequence of out-of-plain rotation and strains of the measurement surface.

This problem, intrinsically associated with two dimensional analyses, is well known in literature [84-88] and its order of magnitude can be easily computed, in case of rigid motion, as:

$$\varepsilon_{fictitious} = \frac{\delta}{D} \qquad \text{eq. 2-1}$$

where δ represents the local out-of-plane displacement between two images, D the working distance and $\varepsilon_{fictitious}$ the resulting fictitious strain computed by the DIC algorithm.

Different approaches have been proposed to partially compensate it for:

- direct measure of the out of plane displacement and analytical compensation of the DIC results [85];
- use of high focal optics in order to increase the working distance [3];
- specific knowledge of the tested material [87];
- use of a reference surfaces [87-88];
- use of multiple 2D hardware [87];

but the intrinsic bidimensionality of the investigated problem remains a hypothesis to fulfil in case of 2D measurements.
A less intuitive issue associated to this aspect and not specifically investigated in literature is the alignment between camera and measurement surface; even in an ideal case, where the problem is purely two-dimensional, the same considerations related to out-of-plane motion may arise if, in the setup preparation, the parallelism between the sensor of the camera and the measurement surface is not guarantee.

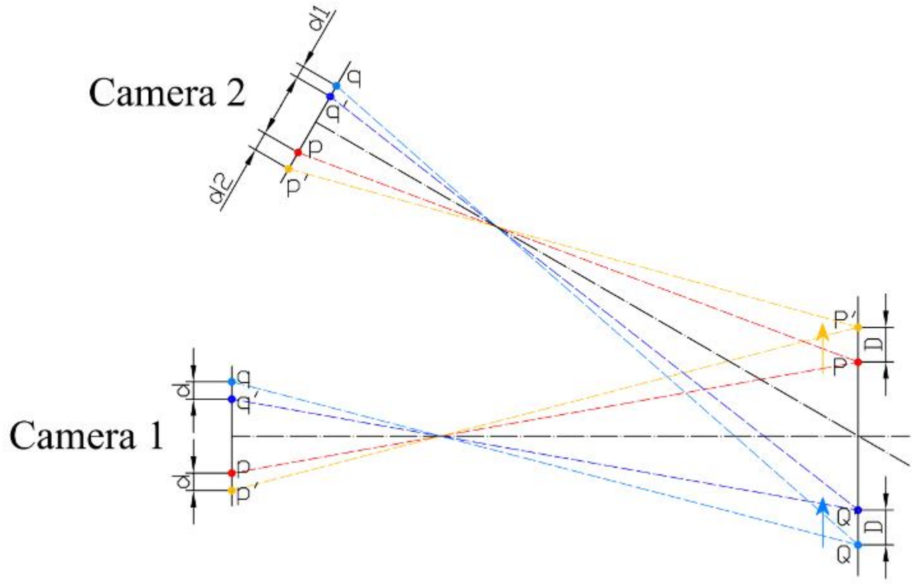

Fig. 2-3 In-plane motion: camera parallel and non-parallel to the measurement surface

The problem can be easily understood by looking the 1-D representation of Fig. 2-3; the measurement surface is planar and subjected to a rigid in plane motion along the vertical direction: all its points are subjected to the same amount of translation D. Two points are highlighted: point P that moves in P' and point Q that moves in Q'. The first camera is placed with the optical axis perfectly orthogonal to the measurement surface: the measured displacement is correctly equal to d for both the points. The second camera is titled with respect to the scene: in this case, the measured displacement of the point P (nearer to the camera) is greater than the one of point Q. Different points of the same rigid surface are subjected to different displacement, so a fictitious strain in seen by Camera 2.

In a real application, an a posteriori correction of this phenomenon is non trivial, considering also that the same problem can arise also on the other out-of-plane rotational axis and the resulting fictitious strains are merged together with the real ones.

At the same time, during the preparation of the measurement setup, it is hard to guarantee the planarity between the inspected surface and the sensor of the camera: for this reason, a tool is needed to be provided to the experimenter in order to ensure the sensor-surface parallelism.

2.2.2 Pose estimation

Pose estimation algorithms are a group of methods able to estimate the three-dimensional position and orientation of a rigid body of know geometry, “target”, with respect to the reference system of a camera framing the object itself [89]. A pose estimation algorithm is the core of the proposed vision based camera placing method: the code is used to instantaneously compute the 3D position of the camera with respect to a target planar with the measurement surface. The camera orientation is iteratively modified in order to minimize the out of plane rotational degrees of freedom and set the sensor parallel to the target, i.e. the measurement surface. To apply the code, coordinates of significant points of the target have to be defined with respect to the rigid body reference system and, at the same time, their positions have to be located on the image. Once the camera is calibrated [90], the characteristics of the vision system (sensor dimension, resolution and focal length of the optic) are known and the pose estimation code computes the 6 degrees of freedom (3 rotations and 3 translations) of the target reference system with respect to the camera one.

The application of the method is consequently composed by two separate steps:

- localization in the acquired images of the coordinates of the points of the target;
- evaluation of the target position and orientation.

In the following, first of all the chosen target will be presented (par. 2.2.3). Then the image processing algorithm, implemented to extract from the acquired images the significant target features, will be described (par. 2.2.4) and optical distortions due to non linearity in the camera lens will be corrected (par. 2.2.5). Three different pose estimation algorithms present in scientific literature will be tested, comparing measured and imposed target movements (par. 2.2.6). Finally, the results obtain by the most suitable code will be compared with the ones of a self developed algorithm as a final validation of the proposed measurement system (par. 2.2.7).

2.2.3 Chosen target

A planar target has been chosen to better fit the requirements associated to two-dimensional setups, even if 3D targets allow reducing measurement uncertainty and, furthermore, overcoming pose ambiguities problems (successively discussed).
The target consists in a rigid plate with four white blobs on a black background (Fig. 2-4); the blobs centroids are the significant points of the geometry. In a planar configuration, four points are the minimum amount information required to apply a pose estimation algorithm: the choice to use only four blobs is linked the will to maintain the target as simple as possible in order to be able to correctly identify its interesting features even in an application subjected to non ideal lighting conditions and, at the same time, allow a fast computation of the camera placement in order to be able to run on real time the code. The target will be fixed on the planar measurement surface in order to correctly orientate the camera.

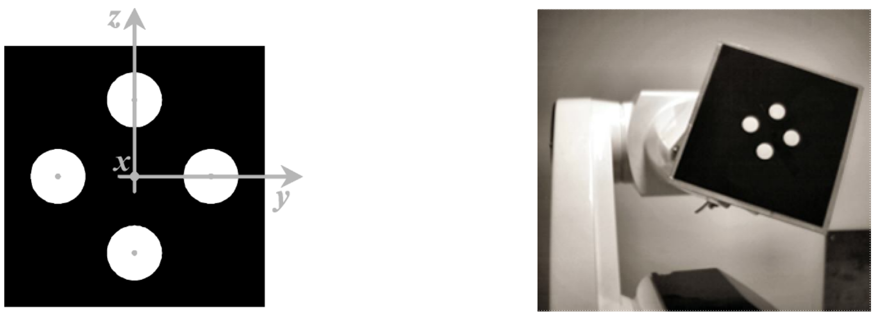

(a) **(b)**

Fig. 2-4 Target design with its reference system (a) and during algorithms testing (b)

2.2.4 Image processing

In order to extract coordinates of the blobs centroids, a blob analysis is performed on the acquired images. Blob analysis is a robust and relative simple image processing technique: once again, the measurement system development choice has been primary driven by the robustness of the approach and the speed of execution.

The acquired image (Fig. 2-5a) is first binarized (Fig. 2-5b). Then a series of filters are applied in order to extract the significant particles: the first one removes all the particles in touch with the image borders (Fig. 2-5c), in the hypothesis that the target is fully framed by the camera. The second filter preserves only those blobs whose area is inside a given range (Fig. 2-5d). The last one selects only ellipse-shaped blobs, thresholding the Heywood circularity factor of the particles (i.e. the ration between the contour perimeter of the blob to the circumference of a circle with identical area, Fig. 2-5e). The coordinates of the four significant points are computed as the geometric centre of gravities of the four blobs in Fig. 2-5e.

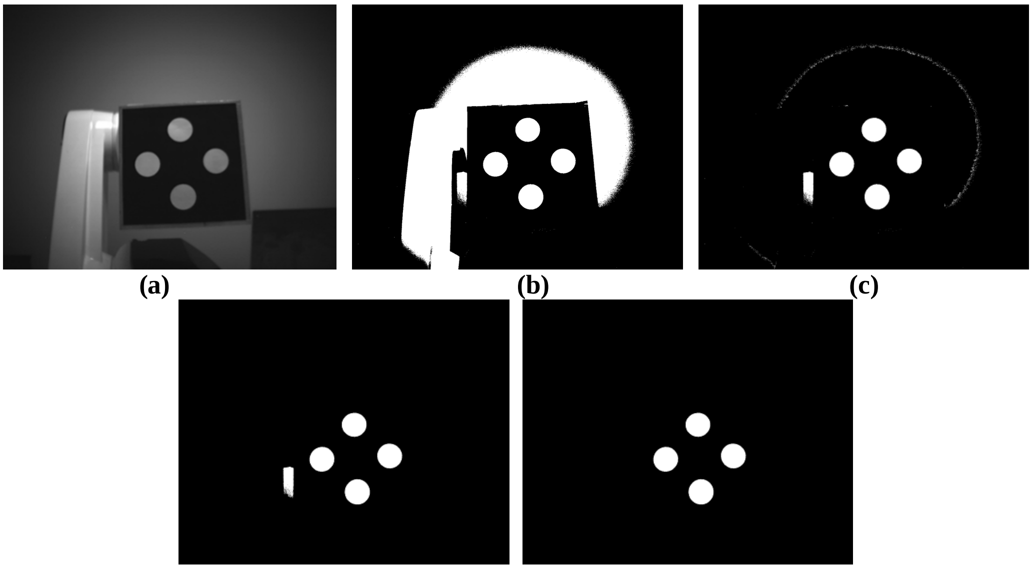

(a) (b) (c) (d) (e)

Fig. 2-5 Blob analysis steps

With the described approach, it is easily possible to tackle changes of the lighting in different setups simply tuning the threshold of the binarization process.

2.2.5 Distortions correction

Pose estimation algorithms are developed considering an ideal pinhole camera model [91]. Nevertheless, in a real application, the optic introduces non-linearity in the image projection. Zhang technique [90] is a state of the art camera calibration procedure, that allows the computation of the parameters to compensate for image distortions and thus it has been applied in order to correct the previously computed points coordinates (Fig. 2-6). Furthermore, optics focal length, a key parameter for the application of pose estimation algorithms, is estimated by Zhang calibration.

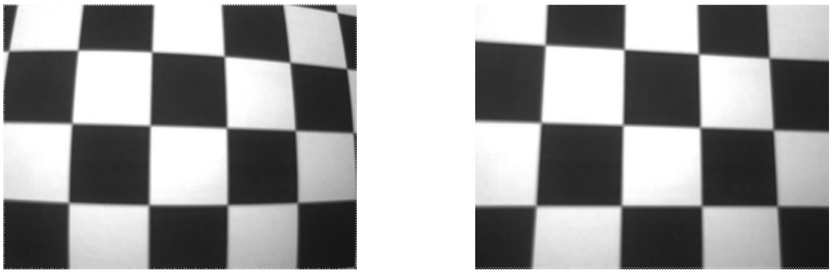

(a) (b)

Fig. 2-6 Calibration grid before (a) and after (b) optical distortion compensation

2.2.6 Pose estimation algorithms comparison

Many pose estimation algorithms are reported in literature; among those, three codes of different level of complexity have been chosen and tested in order to find the most suitable for the specific application. The results of the best one will be successively verified with a self-developed code.

The first algorithm is an iterative general-porpoise approach (i.e. suitable for both three-dimensional and planar targets) developed by Lu and Hager [92]. The algorithm initialization is given by a weak-perspective model as suggested in the work itself. The second tested code is a direct and fast method recently proposed by Pisinger and Mayer [93]. The third code uses the Pising-Mayer direct solution as initialization of the Lu-Hager code, as suggested in [93].

All algorithms were tested moving the chosen target through a 6 d.o.f. robot arm (Fig. 2-4b). In addition to some simply 1 d.o.f. tests, the motion of the robot has been programmed so that its end-effector, that is the target, would follow a motion law spanning through the all degrees of freedom. Fig. 2-7 shows the imposed time history for every degree of freedom of the robot arm (black dotted line) and the trajectory estimated by the Lu-Hager approach (green solid one). Considering the translation, the algorithm seems to be able to return a reliable estimation of the tracker position: the curves are nearly overlapped; the maximum discrepancy is about 1mm in case of in plane coordinates (y and z) and 4mm along the out of plane motion (x). Also in the case of in plane rotation, i.e. roll angle, the pose estimation code returns a meaningful trend: the difference between imposed and measure roll is less that 4°. Out of plane rotations are instead the degrees of freedom where this pose estimation code, not specifically developed for planar targets, shows its limitations and unsuitability: in approximately one half of the sampled points, the algorithm returns a completely wrong orientation of the target, although the estimated position is right. This is behaviour is associated to what is known in literature as “pose ambiguities” [94]: the cost function to be minimized by the algorithm presents local minima in its fitness landscape, where the code gets stuck, mainly associated to specular rotations of the target. In other words, the weak perspective approximation exploited by the code is not able, in this application, to provide an initialization sufficiently near to the global minimum.

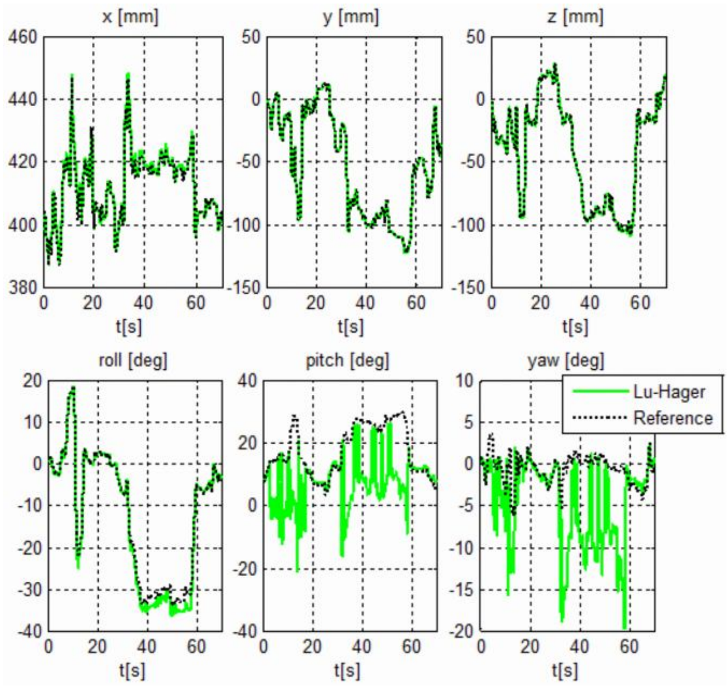

Fig. 2-7 Robot arm test: imposed and estimated (Lu-Hager method) target degrees of freedom

The pose ambiguities problems, just highlighted in the case of Lu-Hager method, are not detected in the remaining tested approaches. For this reason, in order to better characterize the algorithms behaviour, testing results are presented in terms of difference between estimated and imposed time histories (Fig. 2-8).

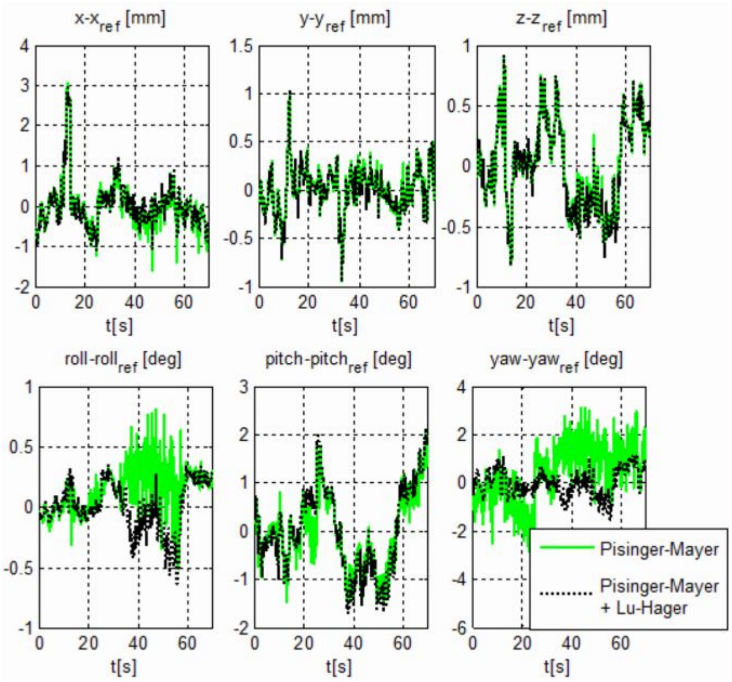

Fig. 2-8 Robot arm test: discrepancy between estimated (Pisinger-Mayer and Pisinger-Mayer+Lu-Hager) and imposed target degrees of freedom

Concerning the three translational degrees of freedom, the two approaches exhibit very similar performances. In case of in plane coordinates and the accuracy of the estimation can be evaluated in about 1 mm, while the maximum discrepancy for the x coordinate is equal to 3 mm. The two approaches manifest more significant differences in relation to the rotation estimation: globally the discrepancies in the roll angle, i.e. the in plane rotation, are limited in less that 1° while rises at 2° in the pitch and 3° in the yaw. Furthermore, the non iterative approach (Pisinger-Mayer, green solid curve in Fig. 2-8) seem to be characterized by higher discrepancies.
Table 1 shows the root mean squared discrepancy for each degree of freedom in case of both Pisinger-Mayer and Pisinger-Mayer + Lu-Hager approaches. Such a parameter can be considered an estimation of the measurement uncertainty.

	RMS ($x-x_{ref}$) [mm]	RMS ($y-y_{ref}$) [mm]	RMS ($z-z_{ref}$) [mm]	RMS ($roll-roll_{ref}$) [deg]	RMS ($pitch-pitch_{ref}$) [deg]	RMS ($yaw- yaw_{ref}$) [deg]
Pisinge-Mayer	0.61	0.24	0.36	0.24	0.88	1.3
Pisinge-Mayer + Lu-Hager	0.58	0.24	0.36	0.20	0.78	0.58

Table 2-1 Root Mean Squared Discrepancies between measured and references d.o.f. in case of Pisinger-Mayer and Pisinger-Mayer+Lu-Hager approaches

The higher measurement uncertainty of the simply Pisinger-Mayer approach is here confirmed, in particular concerning the out of plane target movements.

2.2.7 Comparison of the results with a self developed code

Even in an ideal condition where the coordinates of the points in the image is estimated with null uncertainty, the Pisinger-Mayer initialization is not able to guarantee the convergence to the global minimum of the cost function in 100% of the tests [93]. For this reason an alternative approach has been developed in order to understand if the previously presented discrepancies, or at least part of them, can be linked to pose ambiguities problems.
Starting from a random set of the six variables, the code rotates and translates the target in the space and successively projects it in the image plane. A general purpose non-linear constrained minimization algorithm (S.Q.P, sequential quadratic programming method, [95]) is exploited in order to find the optimal set of variables able to minimize the difference between projected and measured points coordinates, [x, y, z, roll, pitch, yaw]. Such a solution can still be affected by previously discussed pose ambiguities. In order to overcome this issue, the procedure is repeated three times initializing the minimization code with the three specular sets:

[x, y, z, roll, **-pitch**, yaw] [x, y, z, roll, pitch,**-yaw**] [x, y, z, roll, **-pitch**, **-yaw**]

Finally, the selected solution is the one among the results of the four minimizations that leads to the minimum residual error.
This approach is obviously time consuming (the minimization algorithm is not optimized for the problem and furthermore it is repeated four times), but it intrinsically solves pose ambiguities issues testing all the possible scenarios.
The maximum discrepancies between the results of the Lu-Hager+Pisinger-Mayer code and the self developed one are about 10^{-3} mm and 10^{-3} deg, so basically three orders of magnitude smaller that the ones presented in Fig. 2-8.

This proves that the Lu-Hager approach, initialized by the Pisinger-Mayer solution, is actually able to successfully tackle pose ambiguities in the present application. Furthermore, this result gives important information about where the main source of uncertainty is located in the whole measurement system: two completely different algorithms result in basically the same solutions, so it is not the pose estimation itself but the target design and the image processing part that need to be improved in an application where higher accuracy has to be achieved.

2.2.8 Pose estimation for camera placement: implemented algorithm

The self developed code, able, as explained, to provide the same accuracy of state of the art algorithms and correctly solve pose ambiguities, has been implemented in a real time software. Through this software, the experimenter is able to assess the orthogonality between the optical axis of the camera and the measurement surface.
The reference target is printed and fixed on the specimen (in Fig. 2-9 an application of the procedure on concrete beam testing) and the camera is approximately positioned freehand.

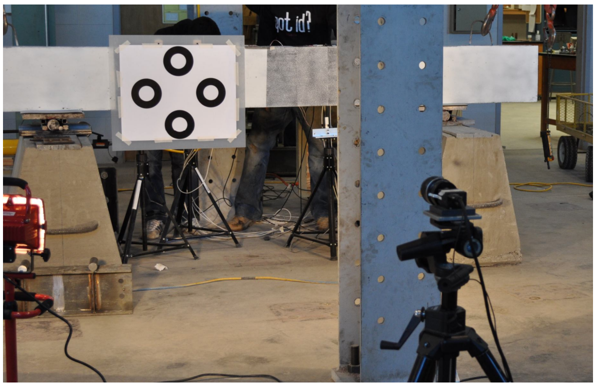

Fig. 2-9 Camera positioning during the setup preparation of DIC applied to concrete beams testing

The user is now requested to tune the image processing parameters in order to obtain a correct recognition of the geometry of the target (Fig. 2-10a).
After that, the target geometry and the calibration parameters (radial and tangential distortion coefficients, sensor-optical axis intersection coordinates and focal lengths) have to be loaded and the boundaries on the 6 degrees of freedom in the minimization set (Fig. 2-10b).

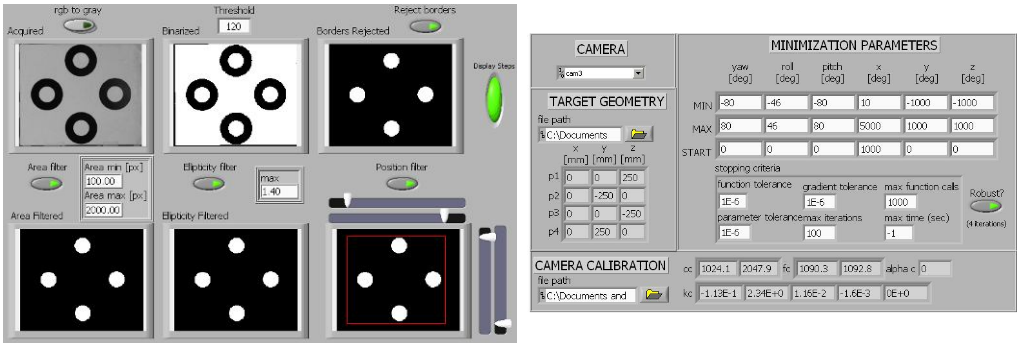

(a) **(b)**

Fig. 2-10 Camera positioning: image processing parameters (a) and software inputs (b)

The software is now able to estimate the position and orientation of the target with respect to the camera reference frame (Fig. 2-11).

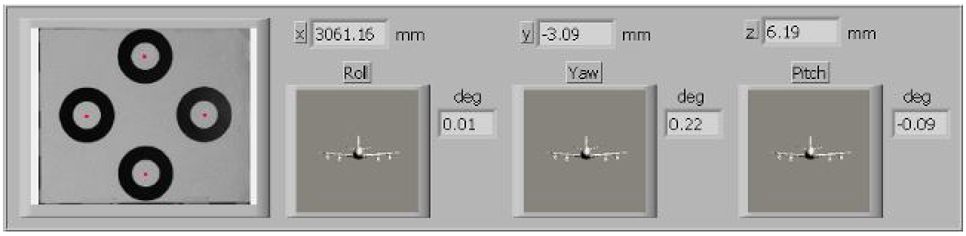

Fig. 2-11 Camera positioning: real time pose estimation

The user can now modify the camera placement (typically acting on the three degree of freedom of the head of the tripod) in order to bring to zero the out of plane angles (yaw and pitch).
The presented code has been exploited in all the experimental activities presented in the following chapters

2.2.9 Pose estimation: an application

As explained, pose estimation algorithms are able to quantify the relative position and orientation of a camera with respect to a target of known geometry. The presented system has been developed in order to correctly orientate the sensor with respect to a target planar with the measurement surface, but could be conversely exploited to estimate the motion of the target with respect to the camera reference system, i.e. as a 6 d.o.f. displacement and rotation transducer.
An application of this is the one reported in Fig. 2-12.

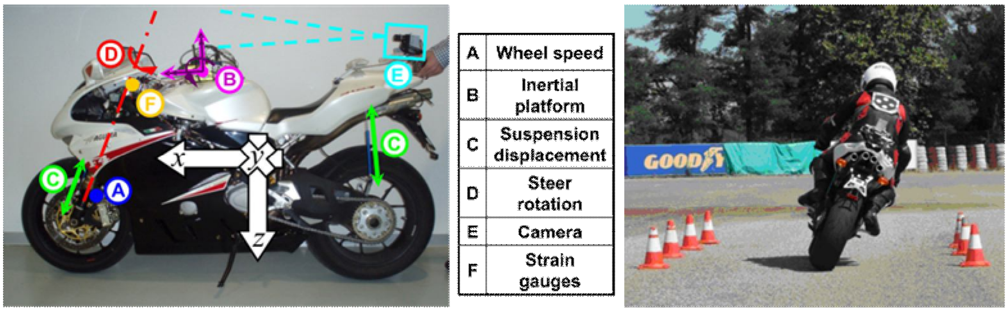

(a) (b)

Fig. 2-12 Pose estimation as displacement and rotation transducer: instrumented vehicle (a) and driver during a test (b)

A digital camera is mounted on an instrumented motorbike, fixed on its main frame, behind the driver's bust (Fig. 2-12a) and a target is fixed on the driver's back in correspondence of his trunk centre of gravity (Fig. 2-12b). The presented pose estimation system is exploited in order to estimate the relative motion of the driver's trunk with respect to the vehicle. Such information is fundamental to investigate the system dynamics, where the mass associated to the upper part of the body of the tester can not be considered negligible if compared to the vehicle one and its motion deeply influences the inertial and dynamic properties of the system.
The camera based transducer has been exploited in order to quantify the trunk displacement and rotation during several standard riding tests (steering pad, double line change, slalom), providing important information related to the human-vehicle interaction.

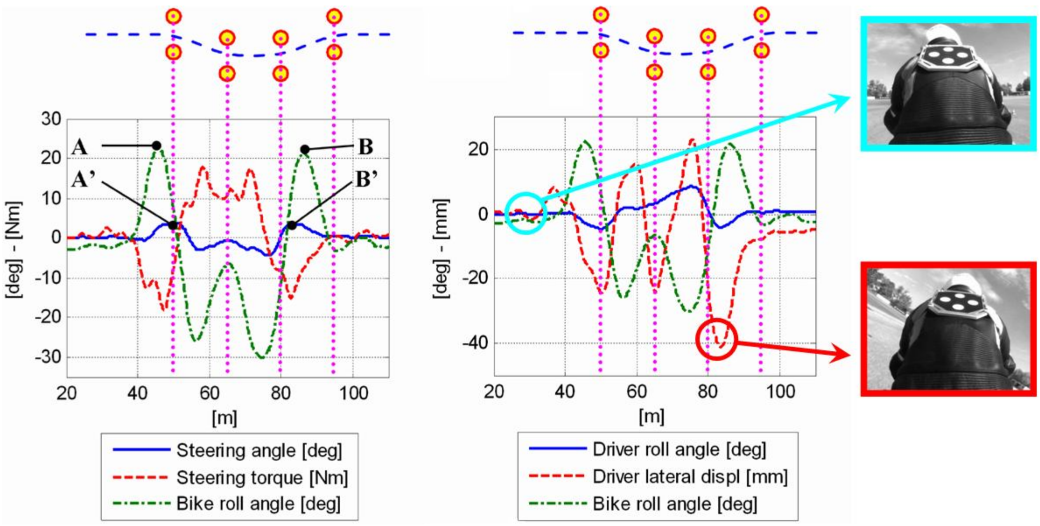

Fig. 2-13 Pose estimation as displacement and rotation transducer: driver's trunk roll and lateral displacement during a double line change manoeuvre

For instance, in Fig. 2-13, data related to a double line change manoeuvre are reported: the out-tracking phase, where the driver begins the curve, is clearly recognizable at 40 m. The steering torque is opposite to the motorbike roll angle in the whole manoeuvre: the pilot contrast and control the rotation of the steering. The steering angle is contrary to the steering torque and in agreement with the motorbike rolling, but shows a delay in the beginning (points A-A') and an advance (points B-B')in the last part of the double line change of about 5 m. This can be explained by thinking that during the out-tracking the driver needs to roll the bike, initially vertical, to start the curve, while in the second part the vehicle is already partially rolled and the driver's action is limited to the tuning of the roll angle through the steering angle. By looking at the motorbike roll angle, it can be notice that, with respect to the limits of the imposed trajectory, the driver advances the corner entry of about 5m and the exit of about 8m. The maximum values of the roll angle are reached before the beginning of the curve. This behaviour is present in both the line changes. The study of the driver's position is carried out considering the lateral displacement and the roll angle of the driver with respect to the vehicle; neglecting longitudinal dynamics (braking or speedup), the behaviour of the remaining four degrees of freedom is negligible. Driver's roll angle and lateral displacement are partially independent. Before the beginning of the first curve, the driver moves his body toward the centre of the curve to roll the bike, without rolling his trunk. When the bike rolling speed reaches its maximum, the driver moves his trunk in the opposite direction and counter-rotates it with respect to the vehicle's roll angle. At the of the change of direction, i.e. where the bike roll angle is equal to 0°, driver's rotation and translation reach their maxima to help the change of direction and so the roll variation.

In the last meters of the first line change, the driver's trunk translate but towards the outside of the curve to partially straighten up the vehicle. The driver's roll angle does not change.

In the second line change, the whole dynamic is repeated.

It can be stated concluded that the driver favours the variation in the bike roll angle by moving his trunk in the transversal opposite direction. In the considered test, the driver anticipates the trunk movement of about 7-8 m with respect to variation of the bike roll angle, i.e. of the trajectory. The associated body rotation is opposite to the bike one and in general slower and less pronounced. It is about 8-10m ahead of the curve.

2.3 Camera focus

In chapters 3 and 4, an extensive study on the effects of digital blurring applied to the acquired images before the digital image correlation analysis will be carried out. For this reason, it will be fundamental to start from images acquired with the highest achievable focus.
A focus estimation algorithm has been selected among the different codes present in literature and implemented to work in real time with a scientific digital camera.

2.3.1 Camera focus algorithms

Camera focusing is a deeply studied issue in scientific literature: nowadays, every commercial digital camera implements an autofocus algorithm able to assist the user in this operation. Regardless the details of the exploited methodology, all the focus procedures can be decomposed in three different steps:

- Definition of the **region of interest**, inside of the framed area, where the code has to work, i.e. which part of the image has to be focussed; this aspect is particularly relevant in case of high perspective scenes.

- Quantitative **measure of the focus** inside the region of interest at the given hardware configuration (i.e. lens-to-sensor distance).

- **Iterative procedure** to vary the lens-to-sensor distance, i.e. act on the focus control, in order to reach the highest achievable focus in the lowest number of steps.

Only the second aspect will be considered in this work: on one hand, the definition of the region of interest can easily be done manually selecting in the area framed by the camera the portion where the measurement surface is actually present (and no perspective has to be present in that area, as previously discussed), once and for all after the camera is placed. On the other hand, scientific cameras are not usually equipped with motorized control of the focus. The tuning has consequently to be done manually and the time required to perform the operation can not be considered an issue in the applications presented in this work, considering that it is a procedure done only once before the execution of the test. At the opposite, it is important to provide the operator a way to maximize the camera focus while tuning the lens-to-sensor distance, based on a quantitative real time evaluation of the focus level.

Regardless the details of the different algorithms, the focus is always measured evaluating in the acquired image the importance of the high frequency components, generally measured directly from spatial domain through convolution and averaged on the whole region of interest. All the performable measures are relative: it does not exist a way to quantify the absolute focus level of a hardware configuration without external references or exact knowledge of the frequency content of the scene (as in [96] to measure camera spatial frequency response, SFR), but it is always possible to compare two different images framing the same object acquired with different lens-to-sensor distances and state which is the one with a better focus.

One of the oldest, and most popular, ways to measure the camera focus is the so-called "Tenenbaum gradient" proposed in [97]. The method convolves the image region of interest with two (x and y) standard Sobel operators (3 by 3 kernel matrices that act basically as two orthogonal high pass filters) and then sums the square of the gradient vector components to calculate the focus measure.

In order to make this measure insensitive the noise level in the acquire image, in [98] the two Sobel filters are replaced by the Laplacian operators and the sums the square of the gradient is substitute by the square of the sum of the Laplacian absolute values (or , alternatively, by its energy in [99]). Alternative approaches can be found in [100], where the computation of the focus measure relies on the application of a non linear edge filter, or in [101] where a wavelet-based approach is proposed.

In [102] a new operator is introduced (mid frequency discrete cosine transform, MF-DCT). Its convolution matrix is a 4x4 symmetric kernel defined as:

$$MF - DCT = \begin{bmatrix} 1 & 1 & -1 & -1 \\ 1 & 1 & -1 & -1 \\ -1 & -1 & 1 & 1 \\ -1 & -1 & 1 & 1 \end{bmatrix} \qquad \text{eq 2-2}$$

and the respective focus measure can be computed as:

$$focus_{MF-DCT} = \sum_{x \in ROI} \sum_{y \in ROI} \left[Int(x,y) \bullet MF - DCT \right]^2 \qquad \text{eq 2-3}$$

where *Int(x,y)* represents the intensity value of the image at the generic coordinate and ● the convolution operator.

With respect to the previously introduce focus estimators, the MF-DCT is proven by authors to be able to estimate the optimal focus at the same lens-to-sensor distance but with increased sensitivity to slightly out of focus images: in other words, varying the lens-to-sensor distance the focus measure describes a curve and the position of its maximum represent the optimal distance. That position is basically the same regardless the implemented algorithm but the MF-DCT reaches this value with higher gradients, so the optimal tuning is easier to be identified.

2.3.2 Implemented code

For the explained reason, the MF-DCT algorithm has been selected and implemented on a real time application, in order to be able to assist the operator in the camera focusing.

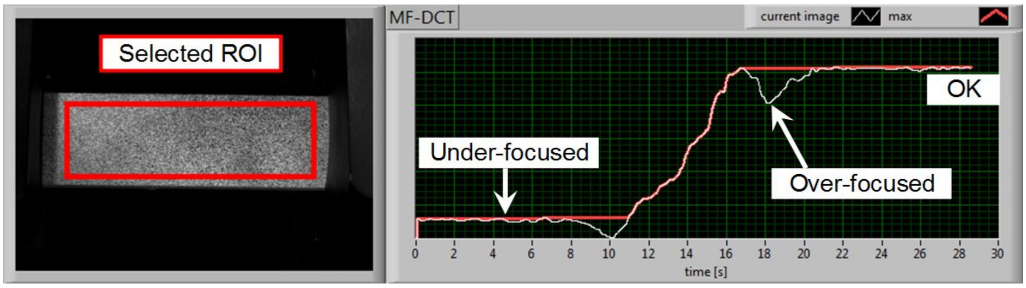

Fig. 2-14 Implemented MF-DCT algorithm

In Fig. 1-9 a screenshot of the implemented code is reported. On the left, the image currently framed by the camera is shown and the user is allowed to select the region of interest where the code computes the focus measure. The focus MF-DCT instantaneous value is graphed on the diagram on the right. The optics is, at the beginning, in a under focused position. Rotating the focus control, the operators can see how the resulting focus measure varies and tune the control to reach a maximum.

The presented code has been exploited in all the experimental activities presented in the following chapters

CHAPTER 3

Image filter pre-processing for uncertainty minimization in two-dimensional digital image correlation

3.1 Introduction

The design and implementation of effective speckle patterns on two-dimensional measurement surfaces are key to enhance the accuracy of digital image correlation (DIC), along with suitable displacement and strain field estimation algorithms [1, 61]. While mathematical formulations for tailored speckle patterns have not been formalized, relevant parameters are discussed in the literature, including mean speckle size and spacing. The accuracy of DIC measurements was studied as a function of mean speckle size and subset size, for which desirable ranges were reported [104, 105, 108, 112]. A range of techniques has been used to create speckle patterns, depending on the specimen dimensions and materials: spray paint or toner powders are typically used for larger specimens, whereas lithography is preferred for smaller patterns [3].

Irrespective of the technique, the resulting speckle patterns are characterized by non repetitiveness and high contrast between light and dark areas. As shown in [113], for translation in two directions, the form of the covariance matrix for the displacement vector, d, is written:

$$Var(d) \cong \sigma_I^2 \begin{bmatrix} \sum_{subset} (\partial I / \partial x)^2 & \sum_{subset} (\partial I / \partial x \bullet \partial I / \partial y) \\ \sum_{subset} (\partial I / \partial y \bullet \partial I / \partial x) & \sum_{subset} (\partial I / \partial y)^2 \end{bmatrix}^{-1} \qquad \text{eq 3-1}$$

d: displacement vector, (u,v), in x - direction and y - direction respectively
σ_I: standard deviation in intensity pattern noise (gray levels)
I(x,y,z): reconstructed deformed intensity pattern (gray levels)

If the gradients in both directions are independent, then the off-diagonal term tends to zero and the matrix is approximately diagonal. In this case, the standard deviation in each displacement component can be written:

$$\begin{cases} Var(u) \cong \dfrac{\sigma_I^2}{\sum_{subset} (\partial I / \partial x)^2} \Rightarrow \sigma_u = \dfrac{\sigma_I}{\sqrt{\sum_{subset} (\partial I / \partial x)^2}} \\ Var(v) \cong \dfrac{\sigma_I^2}{\sum_{subset} (\partial I / \partial y)^2} \Rightarrow \sigma_v = \dfrac{\sigma_I}{\sqrt{\sum_{subset} (\partial I / \partial y)^2}} \end{cases} \qquad \text{eq 3-2}$$

As shown in eq 3-2, “high contrast” corresponds to the summation of high gradients in intensity within a subset, increasing the denominator and reducing variability in the measured displacement. With maximum range between brightest and darkest regions, smooth transitions in intensity across the camera’s dynamic range can be accurately reconstructed by interpolation algorithms, offering the potential for high accuracy when performing subset matching with DIC algorithms. Thus, the gray level distribution within the speckle pattern may be used as a measure of the effectiveness of a speckle pattern [105]. Schreier et al. [55] proposed the implementation of low-pass image filters in the pre-processing stage to produce blurring, either by defocusing the camera’s optics prior to image acquisition or by applying digital filters on the acquired image data. The latter option is more attractive as it allows for better control of the parameters selected to produce blurring. In fact, digital filters are commonly used in image processing. For example, Berg et al. [114] and Cantatore et al. [115] implemented digital filters to produce image blurring, thereby improving the accuracy of algorithms for edge detection.
This chapter presents a study aimed at elucidating the effect of using digital filters to pre-process images, with emphasis on the uncertainty in two-

dimensional DIC displacement and deformation measurements. The methodology is based on numerical simulations where pre-processing using Gaussian low-pass (blurring) filters [116] is implemented. First, the effect of blurring filters on a numerically built speckle pattern is examined at varying values of the standard deviation of the Gaussian kernel (i.e., the filter cut-off frequency). The resulting patterns are used to quantify the resulting DIC measurement uncertainty for the case of constant, linear, quadratic and cubic displacement fields and the associated strain fields. The stability of the relation between Gaussian standard deviation and measurement uncertainty for the case of linear displacement (constant strain) fields is obtained via numerical simulations through use of various levels of image noise, subset size, and frequency content in the speckle pattern.

3.2 Implemented simulation strategy

The effect of pre-processing image blurring on the DIC measurement uncertainty is investigated by means of numerical simulations on a predefined speckle pattern. The methodology is summarized in Fig. 3-2. The simulations are implemented using the Matlab Image Processing Toolbox (The MathWorks, Inc., Natick, MA).

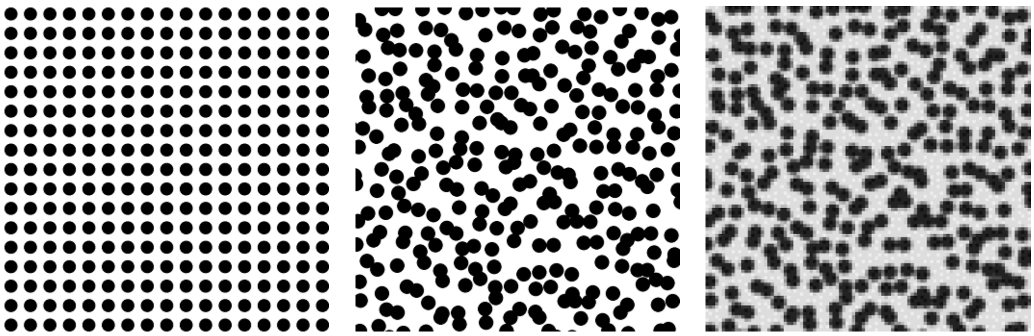

(a) (b) (c)

Fig. 3-1 Numerical simulation of speckle pattern: high-resolution ordinate grid, 1000×1000 pixel subset (a); high-resolution speckle pattern, 1000×1000 pixel subset (b); and low-resolution speckle pattern, 100×100 pixel subset (c)

A 4000×4000 pixel array with eight-bit quantization is numerically built and an ordinate grid of black circular speckles is superimposed (Fig. 3-1a). The speckles have a diameter of 45 pixels and an on-center spacing of 60 pixels along the horizontal, *x*, and vertical, *y*, directions in the coordinate grid. Then, each of the two-dimensional orthogonal coordinates, *x* and *y*, of the centroid of each speckle are perturbed by adding an integer (in order to avoid image re-sampling) displacement whose value is randomly extracted from a uniform distribution in the ±25 pixel range to render the high-resolution speckle pattern in Fig. 3-1b. The intensity pixel range in the resulting image is then narrowed from 0-255 (which identify the speckle and the background, respectively) to 30-225, thus following a routine practice to prevent pixel saturation in real-case scenarios. Fig. 3-1c shows the resulting 400×400 pixel low-resolution speckle pattern, which is produced by low-pass, anti-aliasing filtering and down-sampling by ten times the original high-resolution speckle pattern in Fig. 3-1b. The only noise contribution is introduced by the eight-bit image representation (quantization noise). In the low-resolution speckle pattern, the speckles have a diameter of 4.5 pixels and an average on-center spacing of 6 pixels. The resulting coverage factor, i.e., the percentage of dark pixels in the image, is 42%, which lies within the desirable 40-70% range to minimize measurement uncertainty [107].

The derivation of low-resolution images by down-sampling their high-resolution counterparts is pursuant to mimic a real-case scenario. This approach was carefully qualified by P. Reu in [117] with the aim of quantifying the errors in DIC using both experimental and numerical approaches but only for the case of rigid target shift simulation (i.e. no strain) and without focusing on image filtering for accuracy assessments, while these two aspects are analysed here. With the image down-sampling approach, any displacement and deformation of the speckle pattern may be imposed on the high-resolution image, which simulates an actual two-dimensional area where DIC measurements are performed, while the associated low-resolution image simulates the image acquired using a digital camera. It is noted that this procedure does not require the application of arbitrary interpolation of the final image, which would be necessary when simulating sub-pixel displacements and deformations directly in the final image. The implemented simulation strategy is summarized in Fig. 3-2**.**

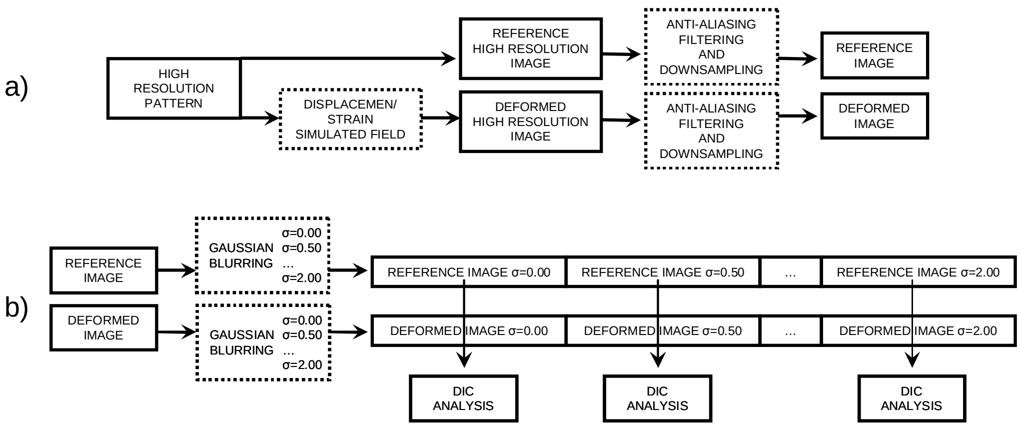

Fig. 3-2 Implemented simulation strategy

In this study, the selected displacement and strain fields are imposed on the high-resolution speckle pattern (Fig. 3-2a), and the associated low-resolution images are derived. For the case of simulated rigid motion, the imposed displacements are integer in the high resolution images and consequently result in a subpixel motion in the low resolutions ones. Conversely, when a non constant displacement field is imposed in order to simulate strains, bicubic image re-sampling of the high-resolution images is implemented [117]. The effect of pre-processing Gaussian filtering of the low-resolution images that simulate the acquired data is studied through a parametric analysis of the standard deviation of the Gaussian kernel vis-à-vis the DIC measurement uncertainty. Gaussian filters are two-dimensional filters [116] that have been previously used for image processing purposes. The impulse response of Gaussian filters is the well-known bell-shaped function whose smoothness enables the minimization of ringing, while binomial filtering enables to define computationally efficient Gaussian filters for Weierstrass transform [118]. In the space domain, the convolution matrix of Gaussian filters is rendered as a zero-mean Gaussian surface. In the frequency domain, different standard deviations of the Gaussian kernel describe a family of filters with different cut-off frequencies.

The values of standard deviation, σ, used in the parametric study range from 0 to 2 pixels, where the former indicates the absence of filters and increasing values are associated with filters that produce more blurring. For a given value of standard deviation, the filter is applied to all the low-resolution image matrices through their convolution with the Gaussian kernel (Fig. 3-2). This is illustrated in Fig. 3-3 for 30×30 pixel portions of the reference 400×400 pixel images, where the image spectra (FFT) amplitudes are also shown together with the superimposed FFT amplitude profile along the x direction; the mean value of the spectra is set to zero to facilitate graphical representation. The peak amplitude is associated with a frequency that corresponds to the average spacing of the speckles. It is noted that the main frequency content of the speckle pattern is in the f_x range below the main peak; by filtering with a lower blurring effect (say $\sigma \leq 1$), higher frequencies are reduced without noticeable perturbations in the main range, whereas increasing blurring results in the progressive attenuation of the main frequency content of the speckle pattern.

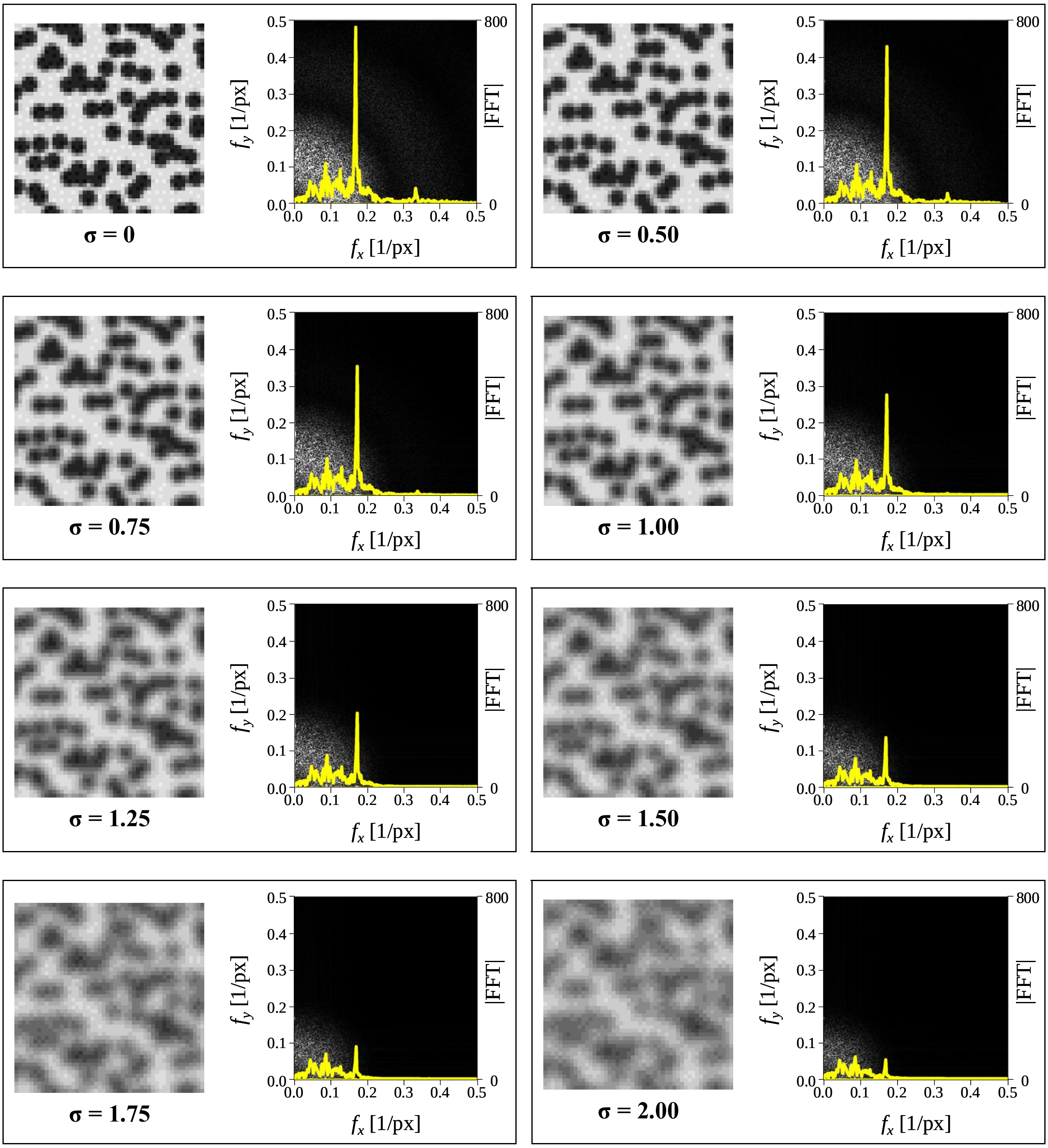

Fig. 3-3 Blurring effect of Gaussian filter on low-resolution speckle pattern (30×30 pixel subset) for different standard deviations, σ, and associated image spectra

The magnitudes of the frequency response functions of the tested filters are reported in Fig. 3-4. Image blurring is applied both on reference and deformed image before the DIC analysis (Fig. 3-2).

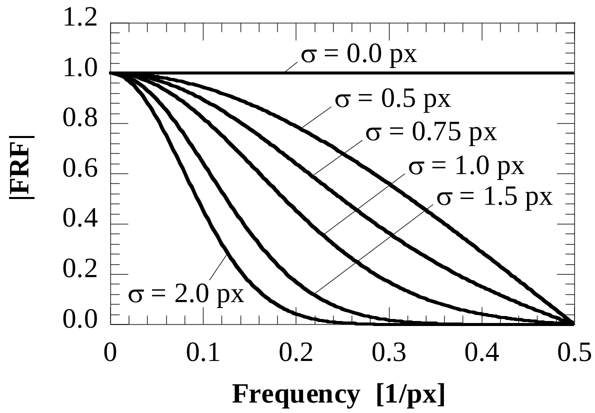

Fig. 3-4 Magnitude of the frequency response function of the tested Gaussian filters

The DIC analysis of the pre-processed (filtered) images is performed using the software Vic-2D 2009 (Correlated Solutions, Inc., Columbia, SC). A 15×15 pixel subset size and a step of 5 pixel (i.e., with a 10 pixel overlap) are considered. An eight-tap optimized interpolation method is implemented, a zero-normalized sum of squared difference correlation criterion is selected to compensate for the scaling and offset in the intensity pattern, thus mimicking real-case applications, and a 5×5 subset decay kernel matrix is enlisted to compute the strain values [3].

3.3 Effect of image filtering preprocessing

The results for the case of constant horizontal (along *x*) displacement and zero strain, and for the case of higher-order (linear, quadratic and cubic) displacement and non-zero strain fields are presented and discussed separately. In particular, the simulation of cubic displacement fields aims at testing the pre-processing filters when the subset matching cannot be exact, since the DIC software used implements a second-order matching shape function [3].

3.3.1 Constant displacement fields

The reference high-resolution (4000×4000 pixel) image is subjected to a constant horizontal displacement from 0 to 10 pixel in 1 pixel steps, thereby obtaining 11 images. The derived low-resolution (400×400 pixel) images having a displacement range from 0 to 1 pixel in 0.1 pixel steps are then pre-processed by applying the family of Gaussian filters introduced earlier.

The effect of image filtering on the bias of DIC measurements is illustrated in Fig. 3-5a, where the mean difference (error) between the displacement measured using Vic-2D 2009, $u_{\mathrm{DIC},ij}$, and the numerically imposed displacement, $u_{\mathrm{IMP},ij}$, is presented as a function of the imposed displacement for representative values of the Gaussian standard deviation, σ, and is computed per eq 3-3:

$$E_u = \frac{\sum_{i=1}^{N_R}\sum_{j=1}^{N_C}\left(u_{DIC,ij} - u_{IMP,ij}\right)}{N_R N_C} \qquad \text{eq 3-3}$$

where N_R and N_C indicate the number of rows and columns of the displacement matrix, respectively, and $u_{\mathrm{IMP},ij}$ is constant for any i and j since a constant displacement is imposed to the entire image.

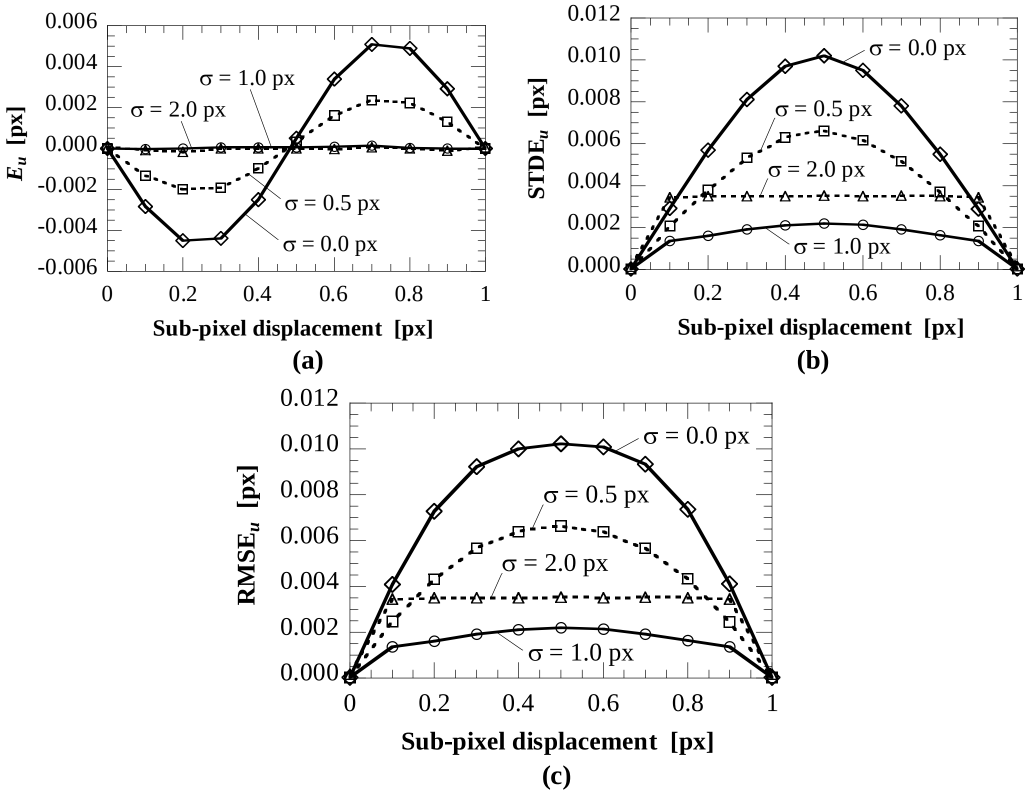

Fig. 3-5 Effect of image filtering on measurement bias and uncertainty for constant displacement: E_u (a), STDE$_u$ (b) and RMSE$_u$ (c) as function of imposed displacement

When the images are unfiltered (σ = 0 pixel), the typical trend of the interpolation bias is noted, where the error function E_u has a sinusoidal shape in the sub-pixel displacement range, and reduces to zero for integer pixel values [113]. The maximum error is reduced by more than half when a filter with a standard deviation σ of 0.5 pixel is applied. The increase in σ results in the progressive reduction of the bias to near-zero values throughout the entire sub-pixel displacement range, thus indicating that filtering enables to minimize the average sub-pixel interpolation bias for pure translation cases.
It is noted that a zero E_u indicates only that the measured displacement values are distributed around those of the imposed displacements without a systematic bias on measurements mean. On the other hand, data dispersion can be easily quantified computing the standard deviation of the measured displacement fields (Fig. 3-5b):

$$STD_u = \sqrt{\frac{\sum_{i=1}^{N_R}\sum_{j=1}^{N_C}\left(u_{DIC,ij} - \bar{u}_{DIC}\right)^2}{N_R \cdot N_C}} \qquad \text{eq 3-4}$$

where $\bar{u}_{DIC}$ represents the average measurement displacement.
With reference to the only bias contribution, it is worth noticing that the trend is deterministic as a consequence of the digital image correlation algorithm but, at the same time, its amplitude is non trivially predictable since it is strongly related to test conditions (in particular image noise and speckle pattern characteristics [117]). At the same time, in real tests the data variability is generally much larger than this effect: its trend becomes evident only as an average phenomenon.
As a consequence of these two aspects, the bias on the single subset estimated displacement can not be generally quantified and consequently it is not compensated for, giving therefore its contribution to the overall measurement uncertainty. For this reason it appears fundamental to include its contribution in the uncertainty estimation and therefore considering the root mean squared discrepancy as an index of the measurement uncertainty.
The effect of image filtering on the DIC measurement uncertainty, i.e., the dispersion of the measured displacements with respect to the imposed ones, is therefore assessed based on the root mean square error, $RMSE_u$, which is computed per eq 3-5:

$$RMSE_u = \sqrt{\frac{\sum_{i=1}^{N_R}\sum_{j=1}^{N_C}\left(u_{DIC,ij} - u_{IMP,ij}\right)^2}{N_R \cdot N_C}} = \sqrt{{E_u}^2 + {STD_u}^2} \qquad \text{eq 3-5}$$

where the two uncertainty contribution (bias and variability) are merged in a single parameter.
The measurement uncertainty of a calibrated (i.e., with no bias) transducer is defined as the standard deviation of repeated measurement data [119]. Here the effect of bias is integrated according to eq 3-5, where the square difference between measured and imposed values is used in lieu of that between mean and measured values.
The effect of image filtering on the uncertainty of DIC measurements is illustrated in Fig. 3-5c, where $RMSE_u$ is presented as a function of the numerically imposed displacement for representative values of σ. The zero $RMSE_u$ value in correspondence with integer pixel values (0, 1) of the imposed displacement reflects the fact that no noise is introduced in the simulated images. A similar trend is noted for σ = 0, 0.5 and 1 pixel, where the uncertainty is symmetrically distributed in a quasi-parabolic fashion with respect to its maximum value at a displacement of 0.5 pixel, and decreases at increasing levels of blurring. For larger values of σ (up to 2 pixel), the maximum uncertainty increases and remains nearly constant in the entire sub-pixel range. Therefore, for the case of constant displacements, the DIC measurement uncertainty is minimized when applying a Gaussian pre-processing image filter with a standard deviation (and associated cut-off frequency) near 1 pixel, whereas a higher uncertainty is attained with less or more blurring filters.

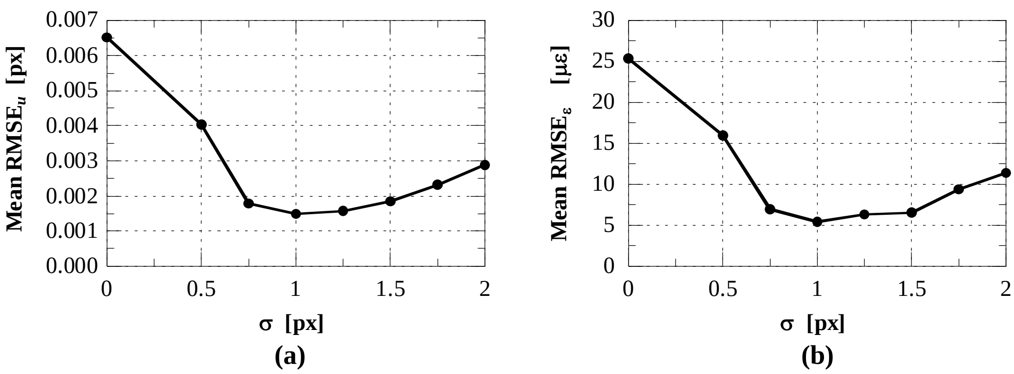

Fig. 3-6 Relation between measurement uncertainty and Gaussian standard deviation for constant displacement: mean RMSEu (a) and mean RMSEε (b) as function of σ

This finding is illustrated in Fig. 3-6a, where the mean $RMSE_u$ for each $RMSE_u$ curve for a given value of the Gaussian standard deviation σ (such as those in Fig. 3-5b) is plotted as a function of the associated σ to conveniently show the relation between measurement uncertainty and image blurring. Through the application of a blurring filter with σ = 1 pixel , the mean $RMSE_u$ is reduced by 77% with respect to that of the unfiltered set of images (σ = 0 pixel). Similar results are obtained for standard deviations in the indicative range 0.75-1.25

pixel, with a higher rate of increase in uncertainty for values below 0.75 pixel and above 1.25 pixel.

The observed relation between DIC measurement uncertainty and standard deviation of the Gaussian filter is also exhibited when simulating strain measurements. This is illustrated in Fig. 3-6b, where the condition of rigid target displacement is still considered (i.e. horizontal translation, no strain) and the horizontal strain estimated by the DIC algorithm is considered. The mean $\mathrm{RMSE}_\varepsilon$ for each curve of horizontal strain measured for a given σ is plotted as a function of the associated σ, with $\mathrm{RMSE}_\varepsilon$ for a given displacement being computed per eq :

$$\mathrm{RMSE}_\varepsilon = \sqrt{\frac{\sum_{i=1}^{N_R}\sum_{j=1}^{N_C}\left(\varepsilon_{DIC,ij} - \varepsilon_{IMP,ij}\right)^2}{N_R N_C}} \qquad \text{eq 3-6}$$

where the notation is similar to that of eq 3-5 and $\varepsilon_{\mathrm{IMP},ij} = 0$ for any *i* and *j* when a zero strain is imposed to the entire image. Again, image blurring with Gaussian filters having σ in the range 0.75-1.25 pixel enables to minimize the measurement uncertainty. As can be seen in Fig. 3-6 , the trend of $\mathrm{RMSE}_\varepsilon$ is very similar to the trend of RMSE_u; this is reasonable because the ε values are obtained as partial derivatives of the u ones.

3.3.2 Linear, quadratic and cubic displacement fields

The functions of the horizontal displacement and strain fields imposed are expressed via eq 3-7 through eq 3-9:

$$u(x) = \varepsilon_{\max} x,\;\; \varepsilon(x) = \varepsilon_{\max} \qquad \text{eq 3-7}$$

respectively, for the case of linear displacement and constant strain,

$$u(x) = \frac{\varepsilon_{\max}}{2L} x^2,\;\; \varepsilon(x) = \frac{\varepsilon_{\max}}{L} x \qquad \text{eq 3-8}$$

respectively, for the case of quadratic displacement and linear strain, and

$$u(x) = \frac{\varepsilon_{\max}}{3L^2} x^3,\;\; \varepsilon(x) = \frac{\varepsilon_{\max}}{L^2} x^2 \qquad \text{eq 3-9}$$

respectively, for the case of cubic displacement and quadratic strain, where *L* is the length of the low-resolution image in the horizontal (*x*) direction (400 pixel), and ε_{max} is the maximum horizontal strain imposed by means of numerical simulation. The results from simulations with maximum horizontal tensile strains between 250 and 20000 με are presented herein; however, it is noted that similar results were attained when simulating compression strain fields with minimum horizontal strain between −250 and −20000 με. These values of $|\varepsilon_{max}|$ cover a relevant range for representative structural materials subjected to service and ultimate stress levels, such as concrete and masonry (ultimate tensile strain ~10^2 με, ultimate compression strain ~10^3 με), steel and aluminium (tensile yield strain ~10^3 με), and fiber reinforced polymer composites (ultimate tensile strain ~10^4 με).

Linear displacement fields

For the case of linear displacement, the horizontal strain imposed is constant (i.e, ε_{max} = ε) and the DIC strain measurement uncertainty is uniformly distributed in the horizontal direction. For strains ε between 250 and 20000 με, Fig. 3-7 shows the (mean) $RMSE_\varepsilon$ per eq 3-6 for all 15×15 pixel subsets for each constant strain profile measured for a given σ, plotted as a function of the associated σ.

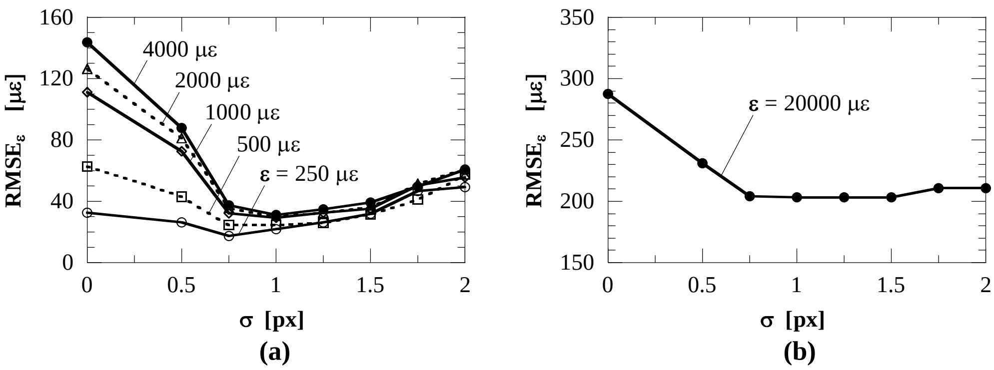

Fig. 3-7 Relation between measurement uncertainty and Gaussian standard deviation for linear displacement and constant strain, ε: RMSEε as function of σ for 250 ≤ ε ≤ 4000 με (a) and for ε = 20000 με (b)

Similar to the case of constant displacement (Fig. 3-6), the uncertainty for unfiltered images rapidly decreases as more blurring filters are applied until it is minimized for filters with a standard deviation in the indicative range 0.75-1.25 pixel. The lower bound (σ = 0.75 pixel) is more effective at relatively smaller strains (ε < 1000 με). For linear displacement fields with strain ~10^2 and 10^3 με (up to ε = 4000 με for the data presented), past the upper bound (σ = 1.25 pixel) the uncertainty increases and tends to converge to similar values irrespective of the deformation imposed and level of image blurring, as illustrated in Fig. 3-7a.

Fig. 3-7b shows that for relatively larger strains (ε = 20000 $\mu\varepsilon$ for the data presented), the application of a blurring filter with σ in the range 0.75-1.25 pixel results in a significant drop in the uncertainty value, albeit not as large as for $\varepsilon \sim 10^3$ $\mu\varepsilon$, whereas a higher level of blurring marginally increases the uncertainty. This result is attributed to the fact that the contribution of filtering to reduce the uncertainty in the sub-pixel range is predominant compared to that in larger ranges that are associated with larger deformations, i.e., the reduction of the uncertainty in the sub-pixel range has a smaller impact on the $\mathrm{RMSE}_\varepsilon$ values in Fig. 3-7b compared with those in Fig. 3-7a.

Quadratic and cubic displacement fields

For the case of quadratic, cubic and higher-order displacement fields, the uncertainty of DIC horizontal strain measurements using unfiltered images is a function of the strain imposed, and thus varies along the *x* direction. To facilitate the graphical representation of the uncertainty as a function of the horizontal coordinate in the domain $0 \leq x \leq 400$ pixel, and for displacement fields with different maximum strain, the parameter $\mathrm{RMSE}_\varepsilon(x)$ is introduced in eq 3-10:

$$\mathrm{RMSE}_\varepsilon(x) = \sqrt{\frac{\sum_{j=1}^{N_C}\left(\varepsilon_{DIC,j} - \varepsilon_{IMP,j}\right)^2}{N_C}} \qquad \text{eq 3-10}$$

where, compared with eq 3-6, the averaging operation is performed only along the vertical (y) direction for $1 \leq j \leq N_C$ (i.e., considering the columns of the displacement matrix), thus rendering $\mathrm{RMSE}_\varepsilon$ as a function of x, which is instead associated with the index i in eq 3-6.

For the case of quadratic displacement and linear strain with different ε_{max}, the function $\mathrm{RMSE}_\varepsilon(x)$ is presented for a representative unfiltered (σ = 0 pixel) and filtered (σ = 1 pixel) set of images in Fig. 3-8.

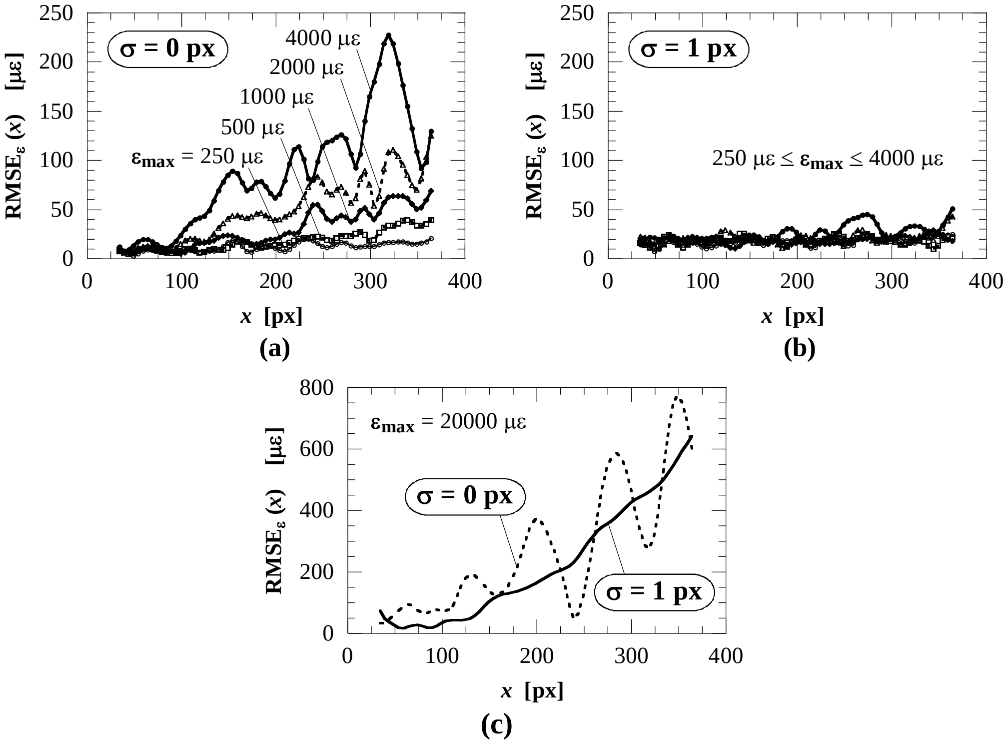

Fig. 3-8 Relation between measurement uncertainty and Gaussian standard deviation for quadratic displacement and linear strain: RMSE$_\varepsilon$ (*x*) for 250 ≤ ε_{max} ≤ 4000 με from unfiltered (a) and filtered (b) images; and RMSE$_\varepsilon$ (*x*) for ε_{max} = 20000 με from unfiltered and filtered images (c). Image filtering based on σ = 1

The outermost 34 pixel portions of the *x* domain having a length *L* = 400 pixel are neglected to eliminate boundary effects that may arise from the numerical computation of strain from displacement fields. The uncertainty of DIC measurements using unfiltered images varies with the strain imposed and exhibits an increasing trend as *x* increases towards more deformed areas, as shown for 250 ≤ ε_{max} ≤ 4000 με and ε_{max} = 20000 με in Fig. 3-8a and Fig. 3-8c, respectively. For linear strain fields with ε_{max} ~10^2 and 10^3 με (up to 4000 με for the data presented), Fig. 3-8b shows that image filtering enables to significantly reduce the uncertainty especially in more deformed areas; for example, for ε_{max} = 4000 με, the peak uncertainty is reduced from 228 με at *x* = 319 pixel to 51 με at *x* = 364 pixel. For linear strain fields with ε_{max} ~10^4 με (20000 με for the data presented), Fig. 3-8c shows that image filtering becomes less effective in more deformed areas (*x* > 150 pixel). However, filtering enables to essentially eliminate the noticeable negative influence of the sub-pixel interpolation bias by reducing the RMSE$_\varepsilon$ (x) function from a sinusoidal shape (σ = 0 pixel) to a more regular and desirable shape (σ = 1 pixel).

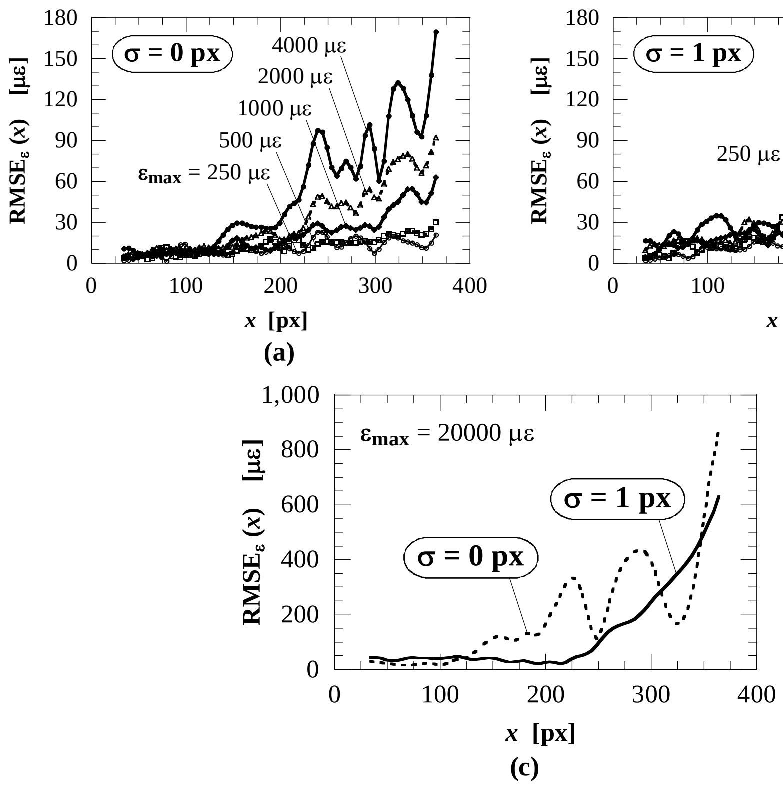

Fig. 3-9 Relation between measurement uncertainty and Gaussian standard deviation for cubic displacement and quadratic strain: RMSE$_\varepsilon$ (x) for 250 ≤ ε_{max} ≤ 4000 με from unfiltered (a) and filtered (b) images; and RMSE$_\varepsilon$ (x) for ε_{max} = 20000 με from unfiltered and filtered images (c). Image filtering based on σ = 1

These findings are consistent with those for the case of cubic displacement and quadratic strain fields, as illustrated for 250 ≤ ε_{max} ≤ 4000 με using an unfiltered and a filtered (σ = 1 pixel) set of images in Fig. 3-9a and Fig. 3-9b, respectively, and for ε_{max} = 20000 με in Fig. 3-9c to facilitate a direct comparison of the RMSE$_\varepsilon$ (x) functions generated with and without image filtering.

3.3.3 Interpretation of the results

The parametric study discussed herein shows that pre-processing image blurring by means of Gaussian filters with a well defined range of standard deviations (approximately 0.75-1.25 pixel) results in the overall reduction of the DIC measurement uncertainty irrespective of the degree of the polynomial

displacement and strain functions. For strain fields with ε_{max} ~10^3 με, a significant decrease in uncertainty is attained as deformations increase; this finding is of practical significance since such level of ε_{max} is associated with critical deformations under service or ultimate stresses for most structural materials. For larger maximum strains (ε_{max} ~10^4 με), the reduction in uncertainty is essentially limited to that attributed to the sub-pixel interpolation bias, which notably affects DIC measurements; this finding is of practical significance since at such level of ε_{max} accurate local measurements can hardly be obtained with more conventional means such as strain gauges and extensometers.
The fact that the range of standard deviations where Gaussian filtering is most effective is largely independent of the displacement and strain functions suggests that it is primarily dependent on the DIC algorithm. In fact, unfiltered images are characterized by steep transients between the dark speckles and the light background with associated high frequency content in the image spectra (Fig. 3-5), which cannot be closely represented by the polynomial interpolation of the intensity pattern that follows the subset deformation according to a given shape function. When these contributions are not filtered, they produce an aliasing effect on the subset interpolation. Filtering becomes effective when the spectral portion having a higher frequency content than that of the interpolation function is minimized, whereas more blurring may result in the loss of frequency content that can be effectively described by the interpolation function, thereby increasing the measurement uncertainty.

3.4 Stability of effect of image filter pre-processing

Following a similar methodology to that of the numerical study presented earlier, numerical simulations are performed for the representative case of linear displacement and constant strain (1000, 4000 and 20000 με) to test the stability of the effect of Gaussian blurring on the uncertainty of DIC measurements by assessing the influence of subset size, image noise, and frequency content of the speckle pattern. The strain measurement uncertainty is quantified by means of $RMSE_{\varepsilon}$, which is computed per eq 3-6 accounting for all 15×15 pixel subsets for each constant strain profile measured for a given σ, similar to Fig. 3-7.

3.4.1 Influence of image noise

A random amount of uncorrelated noise is present in the camera output analog signal for a given pixel. The influence of noise can be minimized by averaging the displacement matrices of multiple images, which must be taken while no additional deformations are imposed; this method is thus not applicable when performing dynamic measurements.

Random noise is simulated by means of the percent additive noise [113], Γ, in eq 3-11:

$$\Gamma = \frac{s}{\Delta I} 100\% \qquad \text{eq 3-11}$$

For a predefined value of Γ, s is the standard deviation of a normal distribution from which a random amount is extracted and added to each pixel, and ΔI is the image intensity pixel range (equal to 225 – 30 for this study). The simulated Γ ranges from 0% (no noise) to 5%, where 0.5% is a reasonable value for a typical camera.

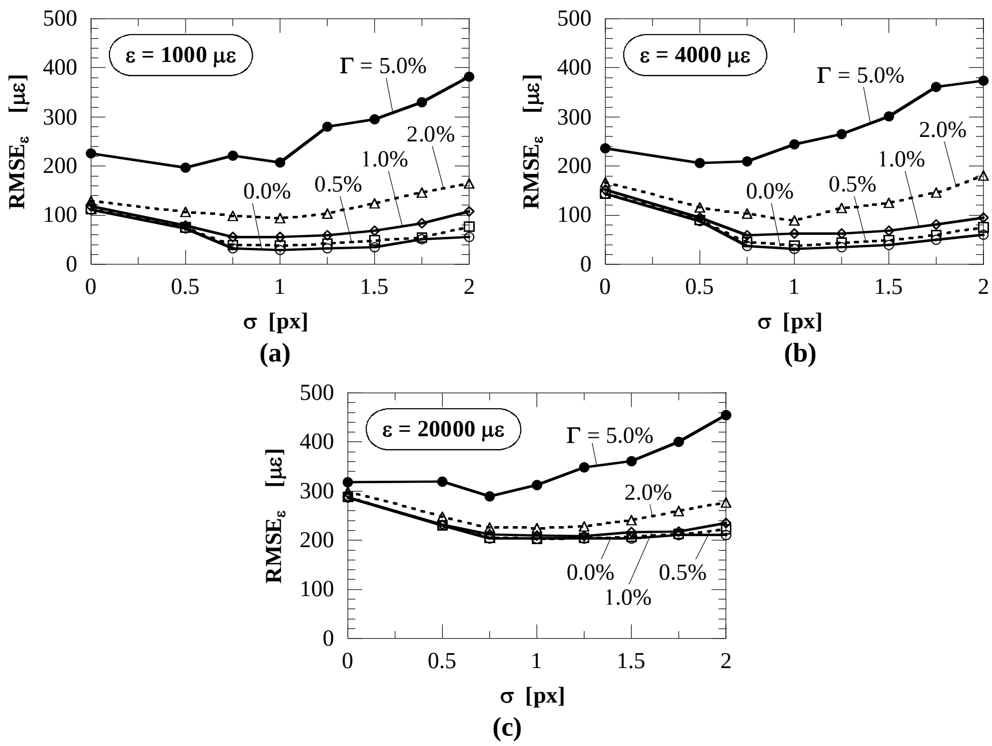

Fig. 3-10 Influence of image noise for constant strain: RMSEε as function of σ for ε = 1000 με (a), 4000 με (b) and 20000 με (c) for 0 ≤ Γ ≤ 5%

Representative $RMSE_\varepsilon$ values are plotted for different levels of noise as a function of the associated σ, for a constant strain ε of 1000 με, 4000 με and 20000 με in Fig. 3-10a, Fig. 3-10b and Fig. 3-10c, respectively. At relatively low levels of noise (Γ = 0.5-1 %), the range of standard deviations at which the uncertainty is minimized is not affected. At relatively high levels of noise (Γ = 5%), the influence of noise is predominant and blurring filters are no longer effective.

3.4.2 Influence of subset size

The low-resolution images from the constant strain simulation are analyzed with different subset sizes: 9×9, 15×15, 33×33 and 63×63 pixel, which is reasonably considered a large subset [110].

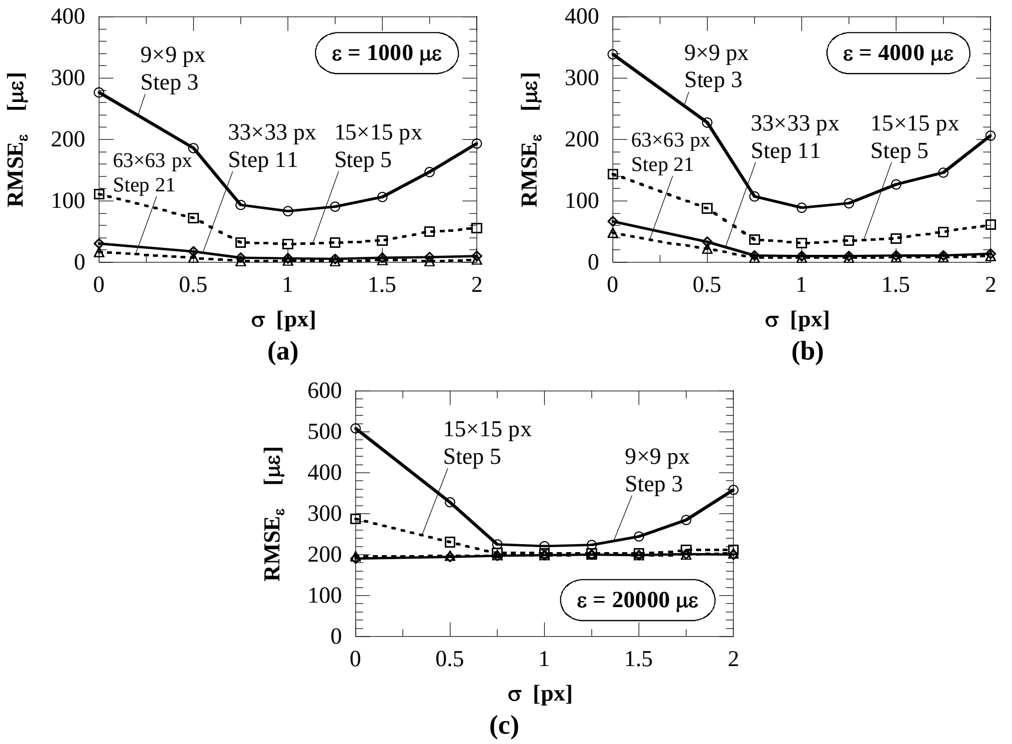

Fig. 3-11 Influence of subset size for constant strain: RMSEε as function of σ for ε = 1000 με (a), 4000 με (b) and 20000 με (c) for 9×9, 15×15, 33×33 and 63×63 pixel subset size

Representative RMSE$_\varepsilon$ values are plotted for different subset sizes as a function of the associated σ, for a constant strain ε of 1000 με, 4000 με and 20000 με in Fig. 3-11a, Fig. 3-11b and Fig. 3-11c, respectively. The subset size does not affect the range of standard deviations at which the uncertainty is minimized. The sensitivity to relatively large levels of blurring decreases at increasing subset size. However, it should be noted that an increase in subset size negatively affects the spatial resolution, which prompts to the need to compromise between uncertainty and resolution when designing a DIC setup.

3.4.3 Influence of frequency content of speckle pattern

Constant strain fields and DIC measurements are simulated on low-resolution images for each of the four different speckle patterns in Fig. 3-12.

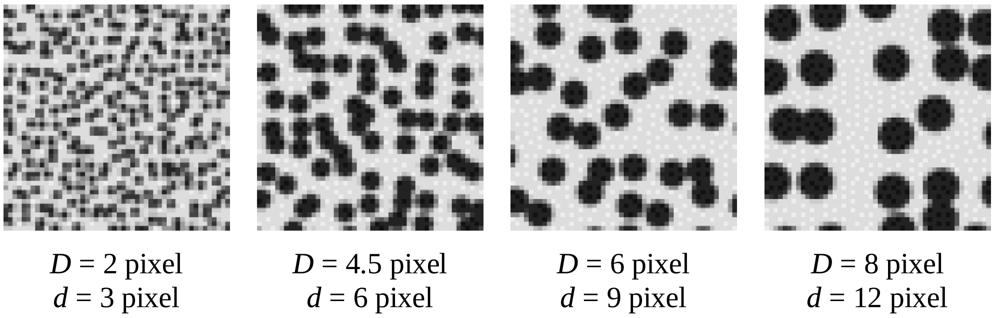

Fig. 3-12 Numerically simulated speckle patterns: 50×50 pixel samples with *D* = speckle diameter, and *d* = average speckle on-center spacing

Different frequency contents are rendered by varying the speckle diameter, D (between 2 and 8 pixel), and the average distance between adjacent speckles, d (between 3 and 12 pixel). Representative $RMSE_{\varepsilon}$ values are plotted for different subset sizes as a function of the associated σ, for a constant strain ε of 1000 με, 4000 με and 20000 με in Fig. 3-13a, Fig. 3-13b and Fig. 3-13c, respectively.

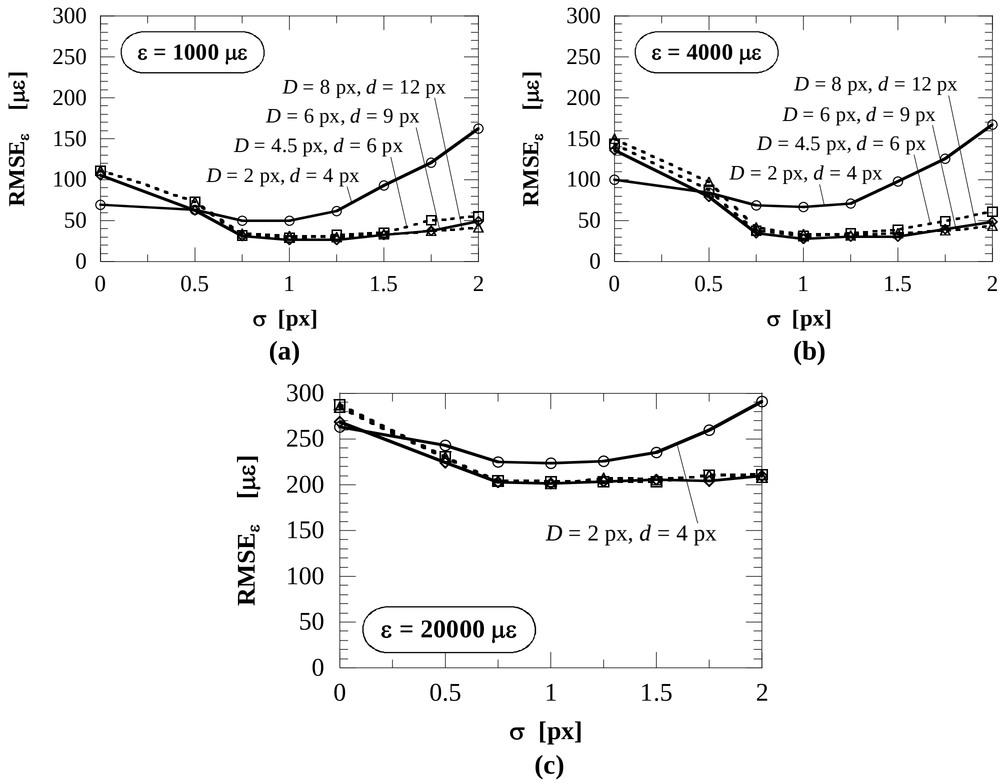

Fig. 3-13 Influence of frequency content of speckle pattern for constant strain: RMSEε as function of σ for ε = 1000 με (a), 4000 με (b) and 20000 με (c) for simulated speckle patterns

When using unfiltered images ($\sigma = 0$), smaller speckles and distances ($D = 2$ pixel, $d = 3$ pixel) enable to better reduce the uncertainty. However, filtering results in an improved reduction of the uncertainty for larger speckles and distances, with no significant increase for relatively strong Gaussian blurs. The range of standard deviations at which the uncertainty is minimized does not change irrespective of the frequency content; in fact, effective blurring affects the areas of steep transition between speckles (of any size and spacing) and background, which are associated with relatively high frequency components and provide a negligible contribution to the frequency content of speckle patterns.

3.5 Concluding remarks

The first part of this paper presents a parametric study where the effect of pre-processing image blurring on the uncertainty of DIC measurements is investigated by means of numerical simulations using Gaussian filters with varying standard deviation. Based on the evidence presented, the following conclusions are drawn:

- Pre-processing image blurring by means of Gaussian filters with a well defined range of standard deviations (indicatively 0.75-1.00 pixel) results in the minimization of the DIC measurement uncertainty irrespective of the degree of the polynomial functions that describe the horizontal displacement and strain fields imposed.

- The effectiveness of a given standard deviation depends primarily on the DIC algorithm. The measurement uncertainty is minimized by using blurred images resulting from the filtering of high-frequency components that cannot be effectively interpolated.

- For constant displacement (zero strain) fields, a major reduction of the uncertainty is attained in the sub-pixel range, where it is more of concern.

- For strain fields with maximum strain ~10^2 and 10^3 $\mu\varepsilon$, either in tension or compression, a significant decrease in uncertainty is attained as deformations increase; this finding is of practical significance since the maximum strain is associated with critical deformations under service or ultimate stresses for most structural materials.

- For strain fields with maximum strain ~10^4 $\mu\varepsilon$, either in tension or compression, the reduction in uncertainty is essentially limited to that attributed to the sub-pixel interpolation bias, which notably affects DIC measurements; this finding is of practical significance since at such level of maximum strain accurate local measurements can hardly be obtained with more conventional means such as strain gauges and extensometers.

In the second part of the chapter, the stability of the effect of Gaussian blurring is tested at varying ε_{max} vis-à-vis image noise, subset size used in the DIC analysis, and frequency content of the speckle pattern. It is concluded that the identified range of Gaussian standard deviations at which the uncertainty is minimized does not change except for extreme levels of noise.

CHAPTER 4

Gaussian blurring: experimental validation

4.1 Introduction

In the previous chapter, image blurring performed through low-pass Gaussian filtering has been introduced and presented as an effective preprocessing operation to remove the highest spatial frequency components in the acquired images responsible of digital image correlation performances worsening.
In this chapter, the experimental validation of the suggested procedure will be provided; the aim of the this chapter is not so much the verification of all the results obtained in the previous chapter as the validation of the implemented simulation strategy presented in paragraph 3.2.
In particular, the uncertainty reduction associated to image blurring is verified at first through rigid motion tests of a physical two-dimensional speckle pattern (paragraph 4.2) subjected to known rigid in plane displacements applied by mean of a Cartesian robot.
Successively (paragraph 4.3), tensile tests on aluminium specimens are carried out and the DIC results compared with finite element models, locally validated by means of strain gauges, in order to confirm the capability of the proposed image blurring procedure to decrease the measurement uncertainty both in case of constant and more complex strain fields. Furthermore, image averaging has been exploited in order to test two different noise levels in the acquired data.

4.2 Rigid motion test

Experiments for the case of constant displacement fields are performed to verify the simulation strategy presented in the previous chapter. The speckle pattern of Fig. 3-1b is printed and affixed onto the smooth surface of a rigid plate, which is mounted on a coordinate measuring machine (CMM, Fig. 4-1).

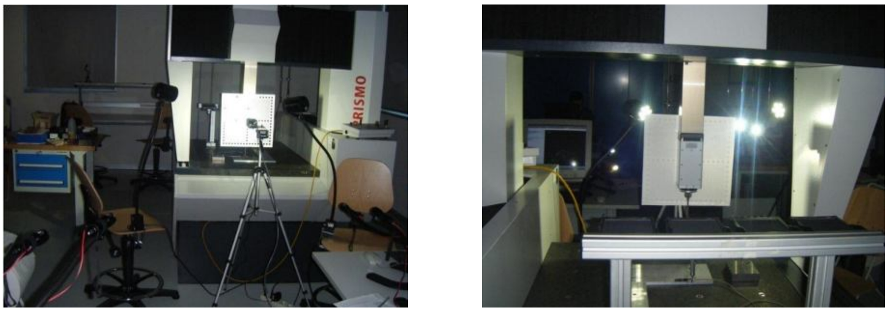

Fig. 4-1 Image blurring experimental validation: rigid motion tests

The pattern is framed by the 400×400 pixel sub-area of a digital camera with resolution of 640×480 pixel (Prosilica GE680, Allied Vision Technologies GmbH, Stadtroda, Germany) and equipped with a lens having 8 mm of nominal focal length. Each side of the square pattern is 160 mm long. The distance between the image plane and the speckle pattern has been tuned to reach a conversion factor of approximately 2.5 pixel/mm, where the actual value is estimated via a two-dimension camera calibration. The position of the camera is assessed using the pose estimation code introduced in paragraph 2.2 and the MF-DCT algorithm of paragraph 2.3 is exploited in order to maximize the camera focus. Constant horizontal displacements from 0 to 1 pixel are imposed with 0.1 pixel steps using the CMM. The uncertainty of the CMM displacement is 2 µm (i.e., 0.005 pixel).
The acquired images have been pre-processed by applying the Gaussian filters similar to the simulations shown in Fig. 3-5, and then analyzed using Vic-2D 2009 and considering a 15×15 pixel subset size and a step of 5 pixel.

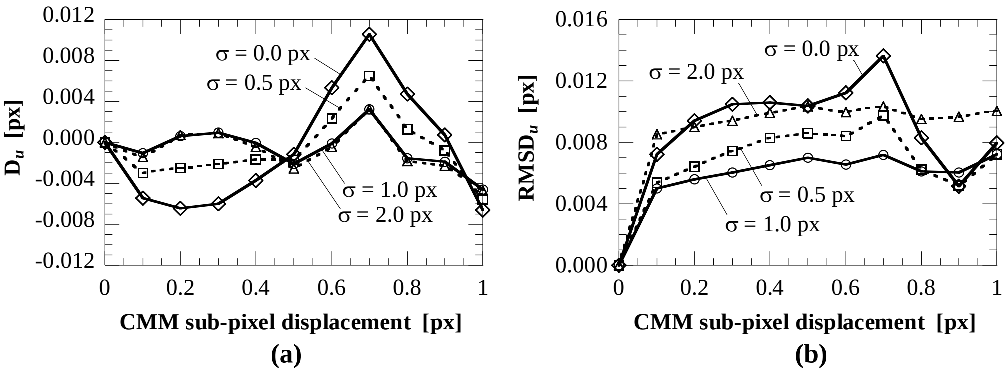

Fig. 4-2 Relation between measurement uncertainty and Gaussian standard deviation for constant displacement: mean RMSE$_u$ (a) and mean RMSE$_\varepsilon$ (b) as function of σ

The effect of image filtering on the discrepancy between of DIC measurements is illustrated in Fig. 4-2a, where the mean discrepancy, D_u, between the measured displacement and that imposed by the CMM is presented as a function of the latter for representative values of the standard deviation, σ. The mean discrepancy values are computed similar to E_u per eq 3-3, where the values of the CMM displacements are used in lieu of those of the numerically imposed displacements. The results show a reasonable agreement with those from the numerical simulations in Fig. 3-5 both in terms of sub-pixel (sinusoidal) trend and decrease in bias at increasing σ. The inevitably larger absolute values, in particular for CMM displacements ranging between 0.7 and 1.0 pixel, are reasonably attributed to vibrations of the camera and its non isolated support, along with the uncertainty of the movements imposed via the CMM.

The effect of image filtering on the uncertainty of DIC measurements is illustrated in Fig. 4-2b, where the root mean square displacement discrepancy, RMSD$_u$, is presented as a function of the CMM displacement for representative values of σ. The RMSD$_u$ values are computed similar to RMSE$_u$ per eq 3-4, where the value of the CMM displacements are used in lieu of those of the imposed displacements. The uncertainty is zero at a zero CMM displacement since the reference image is compared with itself. For non-zero CMM displacements, the uncertainty is minimized by applying a filter with a standard deviation in the vicinity of 1 pixel, thus validating the results from the numerical simulations in Fig. 3-5b.

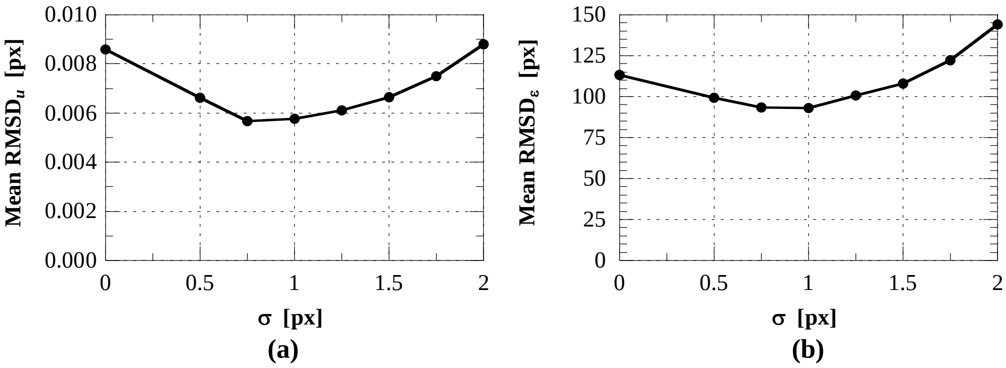

Fig. 4-3 Relation between measurement uncertainty and Gaussian standard deviation for constant CMM displacement: Mean RMSD$_u$ (a) and Mean RMSD$_\varepsilon$ (b) as function of σ

The experimental verification is concluded by assessing the experimental mean RMSD$_u$ and the mean root mean square strain discrepancy, RMSD$_\varepsilon$, vis-à-vis the Gaussian standard deviation, as illustrated in Fig. 4-3a and Fig. 4-3b, respectively. The RMSD$_\varepsilon$ values are computed similar to RMSE$_\varepsilon$ per eq 3-6, where the value of the CMM strains are used in lieu of those of the imposed strains. The measurement uncertainty is minimized when applying filters having σ in the range 0.75-1.25 pixel, whereas lower or higher levels of blurring result in an increase in uncertainty. These findings corroborate those from the numerical simulations presented in Fig. 3-6a and Fig. 3-6b even if the effect of filtering is stronger in case of numerically generated images that in the case of real ones. The differences in the case of low σ values are likely due to the fact that the real images are actually affected by a moderate blurring, due to the real optics effect.

4.3 Constant and complex strain fields tests

In this paragraph, the final validation of the use of Gaussian blurring as a way to increase the measurement accuracy in digital image correlation analyses is presented. Uniaxial tensile tests on four different plate specimens, i.e. a situation where digital image correlation is commonly exploited, are designed and carried out. Two of them are standard dog bone specimens, characterize by a nominally constant strain field in the central area; the other two are designed in order to provide more complex strain fields. The elastic loading range of every plate is divided in ten different steps, and ten images are acquired at each loading step. In this way, not only the effect of the image filtering can be validated but also the image averaging as a way to decrease noise in acquired data is presented. The results of the digital image correlation analyses on the acquired data are compared with finite element models of the plates, locally validated during the experiments by means of strain gauges measurements. In this way, accuracy related to singly acquired images, singly acquired filtered images, averaged images and averaged filtered images is quantified. The comparisons among these results validate the use of image blurring both in case of singly acquired images and averaged images, with a decrease of the measurement uncertainty associated to noise reduction in the second case.

4.3.1 Specimens

Four different specimens are designed for the tests (Fig. 4-4), each with a characteristic geometry. The specimens are plate, in order to respect the planarity required by a 2D analysis (see paragraph 2.2.1).

In the first one, the width (and consequently the area of the resistant section) hyperbolically varies along the longitudinal abscissa: this design, combined with the symmetry of the geometry, creates theoretically (far from the border effects) a linear monoaxial variation of the strain field along the vertical axis of symmetry during the tension test. The remaining parts of the surface are characterized by a more complex, bidimensional, state of strain. The second specimen is design with the same approach but different gradient in the reduction of the section, in order to test two different situations of the same phenomenon.

The third and the fourth specimens are classical dog-bone specimens for tensile test, characterized by a filleted constant area which is able to provide constant strain fields. In particular, the number 4 has been design according the U.S. standards [120].

All the specimens have been cut from the same direction of the same plate, in order to guarantee uniformity in the material properties. The selected metal is a 6061-T6 (solutionized and artificially aged) aluminium alloy: this material present higher elastic range with respect to traditional aluminium and thus easily allows the study of relatively high strain (up to about 4000 µm/m) preserving the hypotheses of a linear problem. The nominal mechanical properties of the selected alloy are summarized in Table 4-1.

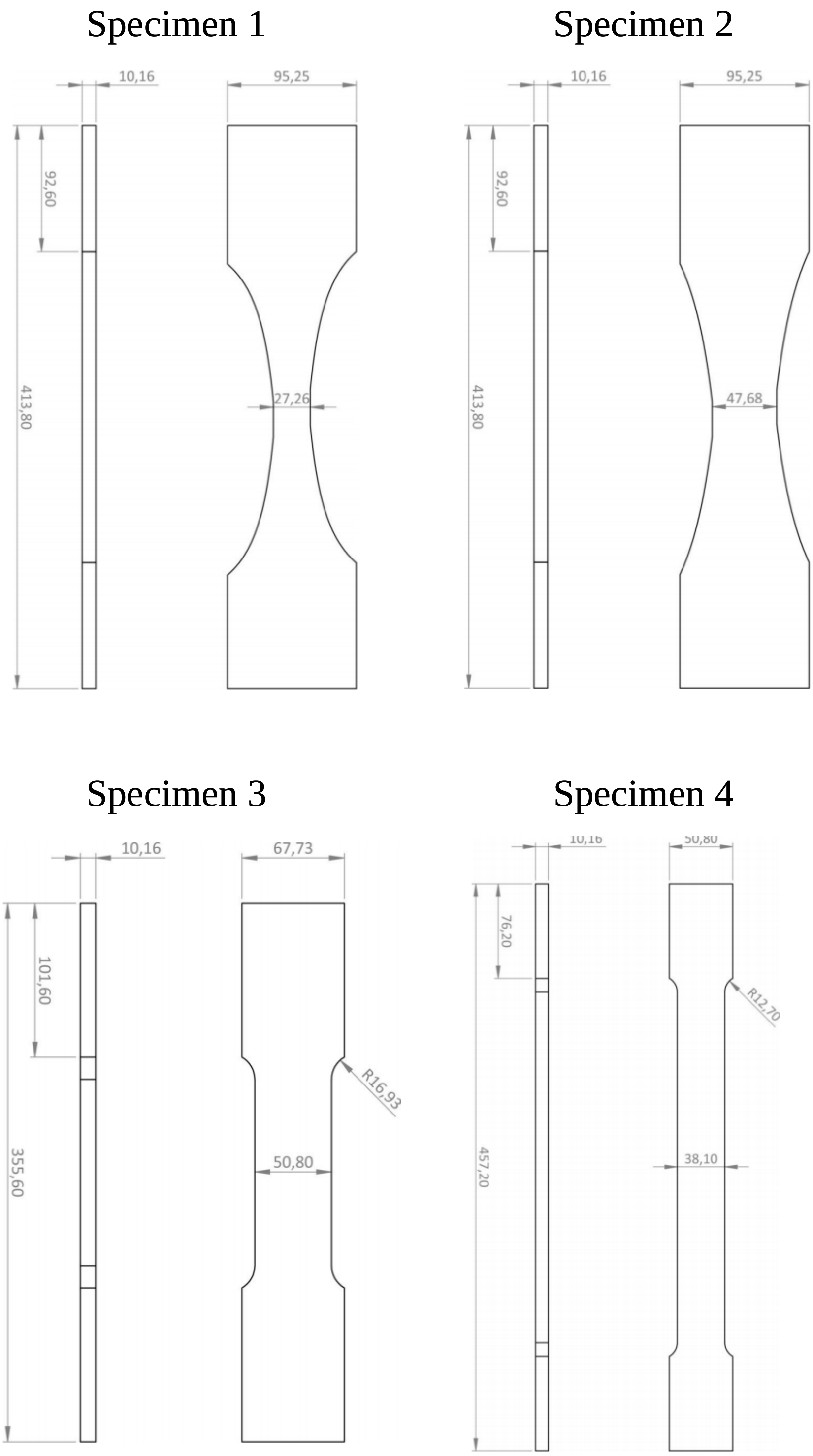

Fig. 4-4 Tested specimens

Young modulus E	68.9 GPa
Poisson's ratio ν	0.33
Yield stress R_y	276 Mpa
Ultimate tensile strength UTS	310 Mpa

Table 4-1 Al 6061-T6: nominal mechanical properties

4.3.2 Speckle pattern realization

In order to perform digital image correlation measurements, a speckle pattern has to be created on the surfaces of the specimens. At first, the surface of all the plates has been spray painted with a light film of white opaque enamel to increase the resulting pattern contrast and avoid specular reflection on the measurement surface.

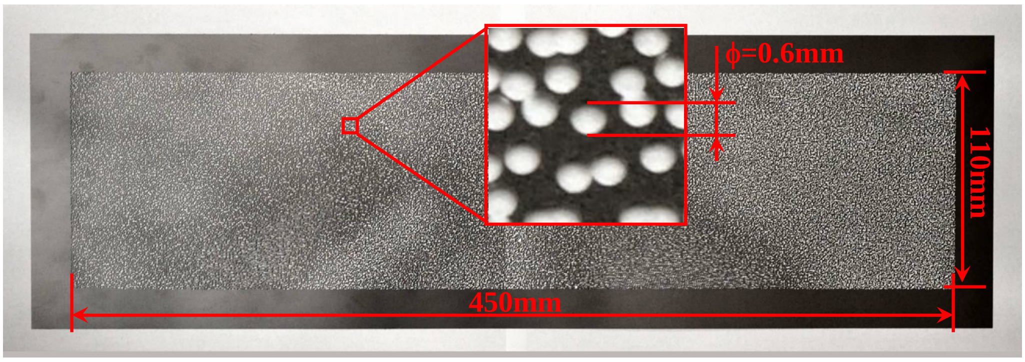

Fig. 4-5 Stencil for speckle pattern realization

To realize the speckles, a stencil has been prepared (Fig. 4-5). A 0.2 mm thick stainless steel sheet is micro-drilled by mean of chemical machining starting from the same pattern design exploited in paragraph 3.2. One hole is realized in the metal sheet in correspondence of every speckle, with a 0.75 px/mm scaling factor (speckles of 0.6 mm diameter each from a 4.5 px diameter design). Leaning the stencil on the measurement surface of the plates and spraying it with an airbrush it is easily possible to create the speckle pattern. Black opaque enamel has been used.

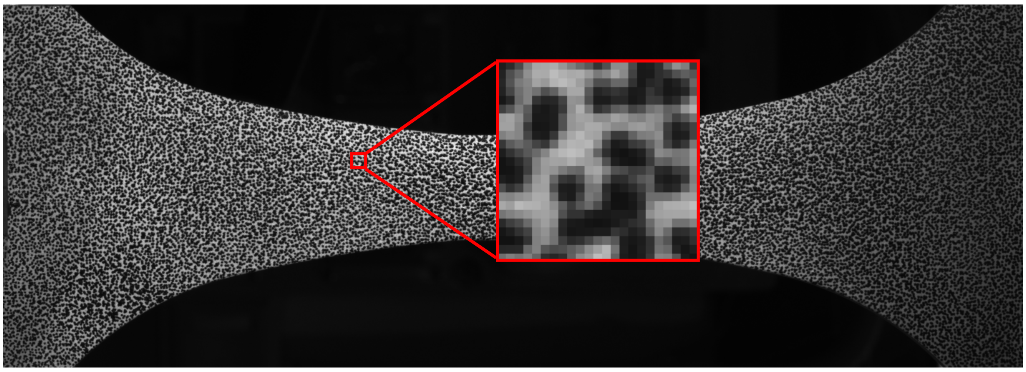

Fig. 4-6 Specimen 1 after speckle pattern realization

In Fig. 4-6 the resulting speckle pattern, as actually framed by the camera during the test, is reported in case of Specimen 1.

4.3.3 Reference: finite element model and strain gauges

A linear elastic finite element model of every specimen has been created starting from the nominal mechanical properties of the alloy of Table 4-1. The analyses are carried out in Abaqus, using a 3D model of every plate meshed with C3D20D elements (general purpose quadratic brick elements). These models will provide the reference strain field to be compared with digital image correlation results in order to quantify the measurement uncertainty in the four different tested conditions (single image, single filtered image, average image, and average filtered image).

The simulated plates aimed to model a very simple problem (linear elastic loading of an isotropic homogeneous material) and are consequently expected to provide an accurate reference.

Nevertheless, strain gauges are applied on the surface of the specimens opposite with respect to the one framed by the camera to measure the local strain during the tests: the acquired data will be used to locally validate the f.e. models. The selected electric strain gauges are compensated in temperature for aluminium materials and present a monoaxial 3 mm sensible grid length. The acquisition is done in half bridge configuration with a temperature compensator for every sensor. All the gauges are applied on the longitudinal axes of symmetry of the specimens (y=0 in the sketch of Fig. 4-7), where a monoaxial state of strain is expected as a consequence of the specimens symmetry.

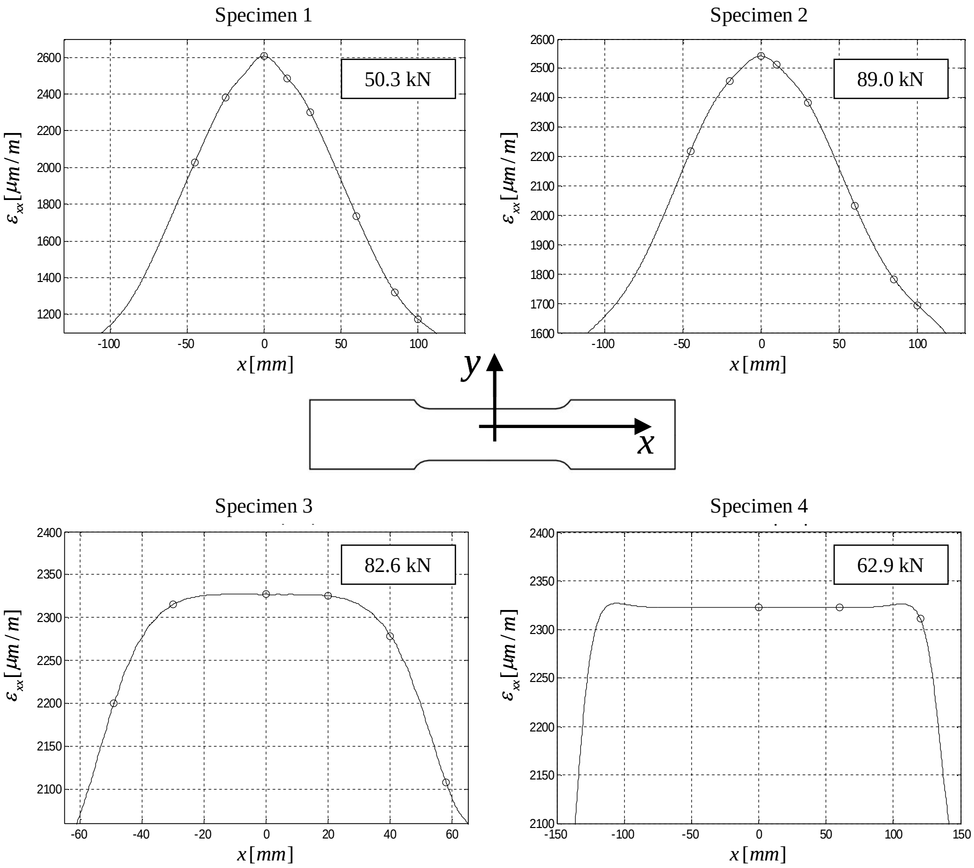

Fig. 4-7 Expected strain profile along the y=0 axis and strain gauges selected positions

The position of the gauges on every plate has been chosen starting from the finite element analysis of the specimens on the y=0 axis and is reported in Fig. 4-7 (strain curve referred to maximum elastic load discussed in the following paragraph).

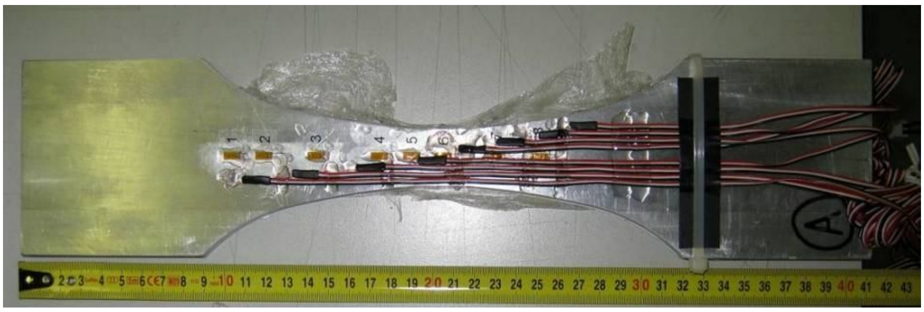

Fig. 4-8 Strain gauges applied on Specimen 1

Fig. 4-8 the Specimen 1 surface with the gauges applied is reported.

4.3.4 Testing procedure and setup

Starting from a finite element analysis, the loads able to induce in the central section of every plate a strain field of about 400 µm/m (i.e. a sufficient magnitude of the strain filed for digital image correlation measurements) are quantified: these loads represents the forces apply to the specimens at the first step of the tensile tests. Successively, f.e. models are exploited in order to estimate the maximum elastic loads, i.e. the forces that induced in correspondence of geometry discontinuities strains close to the linear elastic limit of the Al 6061-T6 alloy: these loads are the last steps of the tensile tests and are reported in the text boxes of Fig. 4-7. The curves of Fig. 4-7 actually represent the strain profile in the y=0 axis when these limit loads are applied to the specimens according to the f.e. model. Among these two boundaries, ten equally spaced loads are selected and each of them is a step of the tensile tests.

Fig. 4-9 Tensile test setup

In Fig. 4-9 the testing layout is reported. The specimen is fixed on the tensile machine and lighted by means of led lights (i.e. cold lights, in order to avoid distortions in the acquired image related to hot air waves). The camera, after the calibration, is placed in front of the specimen: the position is assessed using the pose estimation code introduced in paragraph 2.2 and the MF-DCT algorithm of paragraph 2.3 is exploited in order to maximize the camera focus. The strain gauges on the specimens and the load cell of the tensile machine are acquired synchronously with the images framed by the camera.

The tensile machine is force-controlled. At first, with no loads applied to the specimens, ten images of the tested-plate are acquired. These data represents the

reference images of the digital image correlation analysis. Successively, the load increases to the first step, the machine stops and a new set of 10 images is acquired. The procedure is repeated for the remaining 9 steps, crossing the whole elastic range of every specimen. In order to avoid a significant relaxation of the material during the stops, the target loads are approached with a decreasing loading rate.
Using the load cell and the strain gauges data acquired during the loading test, the actual elastic characteristic of the tested alloy has been retrieved and the finite element model updated.

4.3.5 Tensile tests results

The acquired images of every plate are pre-processed in four different ways:

- at every load step, the first image of the acquired set is extracted, resulting in 10 **singly acquired images**;

- at every load step, the first image of the acquired set is extracted and filtered with a gaussian low pass filter, σ=0.75 px, resulting in 10 **singly acquired filtered images**;

- at every load step, the 10 images of the acquired set are pixel by pixel averaged, resulting in 10 **averaged images**;

- at every load step, the 10 images of the acquired set are pixel by pixel averaged and filtered with a Gaussian low pass filter, σ=0.75 px, resulting in 10 **averaged filtered images**;

and consequently four different digital image correlation analyses are carried out for every specimen. In the following, for every specimen the DIC results will be presented and compared with data from the finite element models. Starting from these comparison, the measurement uncertainty will be quantify in order to validate the use of the Gaussian blurring as a method to decrease the measurement uncertainty and quantify the accuracy enhancement associated to image averaging.

Tensile test results: Specimen 1
The first analyzed specimen is the hourglass-shape one characterized by the narrowest minimum resisting section (Fig. 4-4).
In Fig. 4-10 compares the strain profile along the y=0 axis measured by the four different DIC analyses with the reference finite element data. Local strains

measured by the strain gauges are also reported. Data relative to two different loading levels (at the beginning (a) and at the end (b) of the test) are shown. The four different experimental curves represent the four different DIC analyses previously discussed.
Starting from the comparison among measured and reference data of Fig. 4-10, it is possible to have a rough idea of the measurement uncertainty associated to DIC measurements. The average global matching of the nominal value of the strains can be clearly recognized, along with non negligible data dispersion, particularly in the lowest load curve. It is instead more difficult to appreciate and quantify the differences in terms of measurement uncertainty related to the four different DIC analyses.

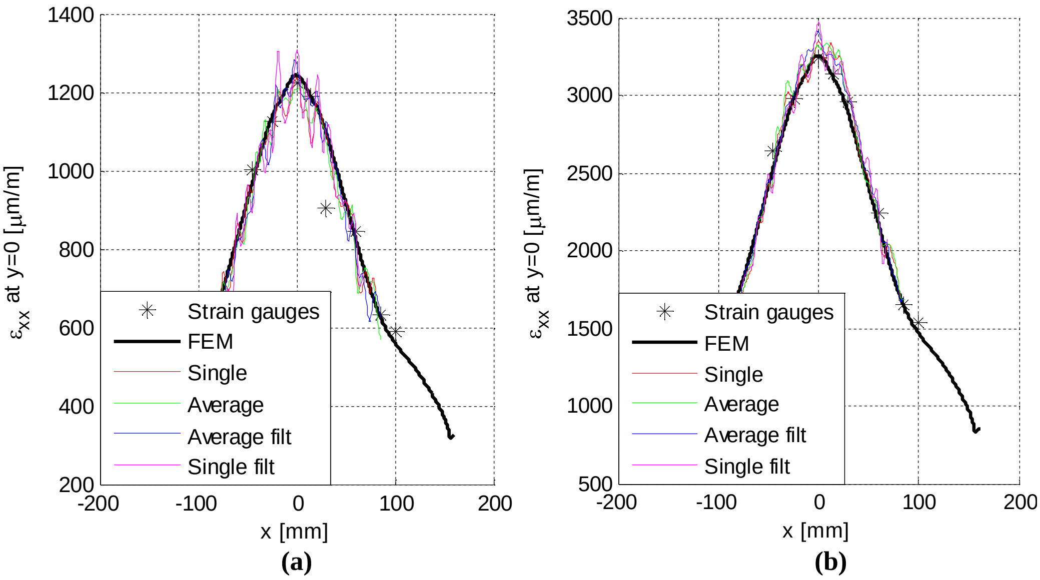

Fig. 4-10 Specimen 1: axial strain profile along the y=0 axis; low loading level (a, 24 kN) and high loading level (b, 63 kN)

In order to better study the influence of the pre-processing on the final accuracy, the root mean squared discrepancy among measured (in the four cases) and reference strain field is computed, extending the analysis to the whole measurement surface:

$$RMSD_{\varepsilon_{XX}} = \sqrt{\sum_{i=1}^{N_R} \sum_{j=1}^{N_C} \left(\varepsilon_{XX,DIC,ij} - \varepsilon_{XX,FEM,ij}\right)^2} \qquad \text{eq. 4-1}$$

The results are reported, for all the tested loading conditions, in Fig. 4-11.

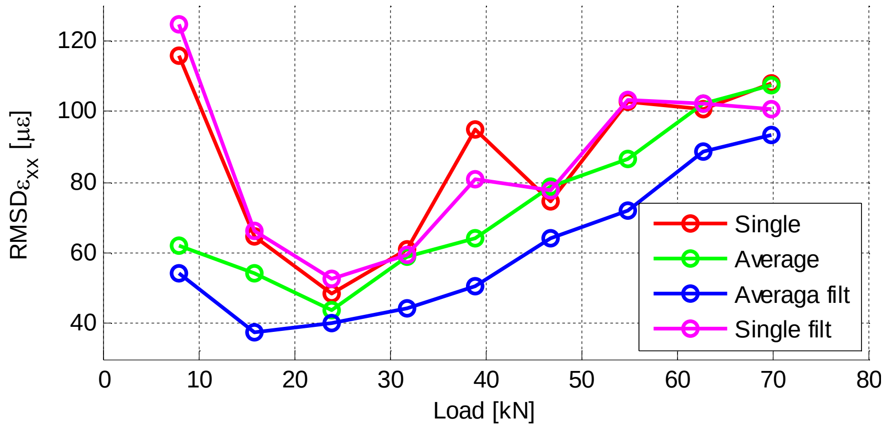

Fig. 4-11 Specimen 1, RMSD ε_{xx} for all the tested loading levels

From the curves of figure Fig. 4-11 it can be clearly noticed how the image averaging is able to reduce, in basically the whole tested range, the measurement uncertainty by increasing the signal to noise ratio of the acquired data and, at the same time, how the image filtering on the averaged images can further increment the DIC performances. The effect of the Gaussian blurring on the singly acquired image is less important: no sensible improvement can be noticed but, at the same time, the pre-processing does not reduce the quality of the computer results. Furthermore, average data are characterized by a smoother trend: the averaging process reduces the influence of external factors in the acquisition process (noise, as explained, but also camera vibration, light fluctuation etc).

The root men squared discrepancies shows a global increase in the measurement uncertainty as the strain become bigger. To better understand this phenomenon, the RMSD has been normalized with respect to the loading level (Fig. 4-12).

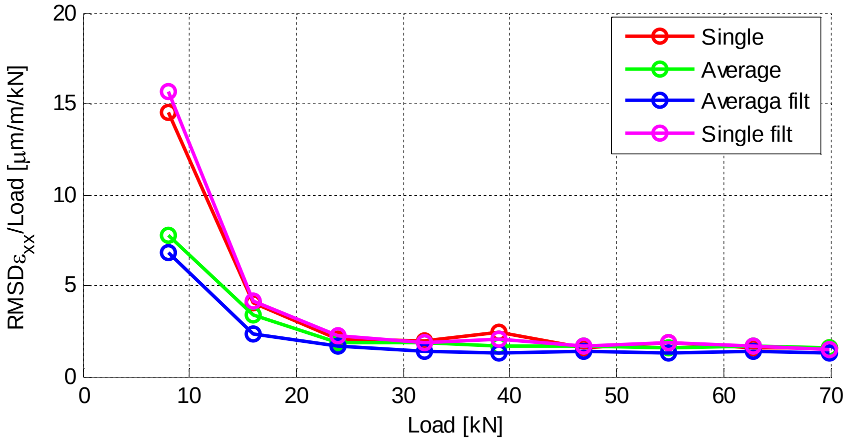

Fig. 4-12 Specimen 1, normalized RMSD ε_{xx} for all the tested loading levels

For low strain levels, the relative contribution of the "ground noise" of the DIC technique is predominant; at the opposite, once a sufficiently high strain level is reached, the uncertainty increases proportionally to the applied load (i.e. to the magnitude of the strain field).

Tensile test results: Specimen 2

Specimen 2 is characterized by geometry similar to the one of Specimen 1, with a less pronounced section reduction in the central area (Fig. 4-4).

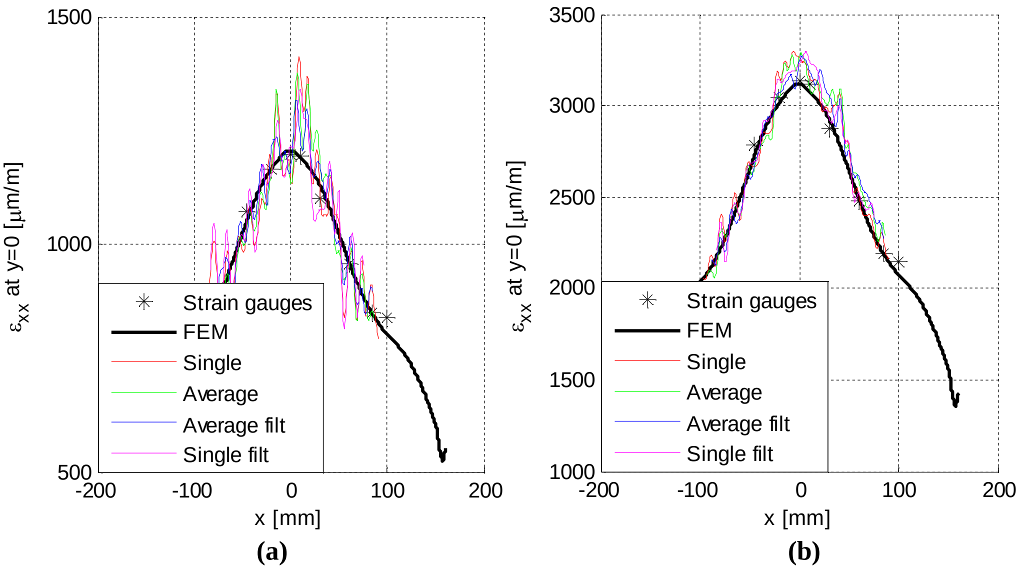

Fig. 4-13 Specimen 2: axial strain profile along the y=0 axis; low loading level (a, 42 kN) and high loading level (b, 109 kN)

In Fig. 4-13 the measured and reference strain profiles in correspondence to the y=0 axis is presented, as in the previous chapter, at two different loading levels of the test. It is worth to notice the high correspondence between finite element results and local strain measured by the strain gauges, as confirm of the fidelity of the f.e. predictions and their use as reference.

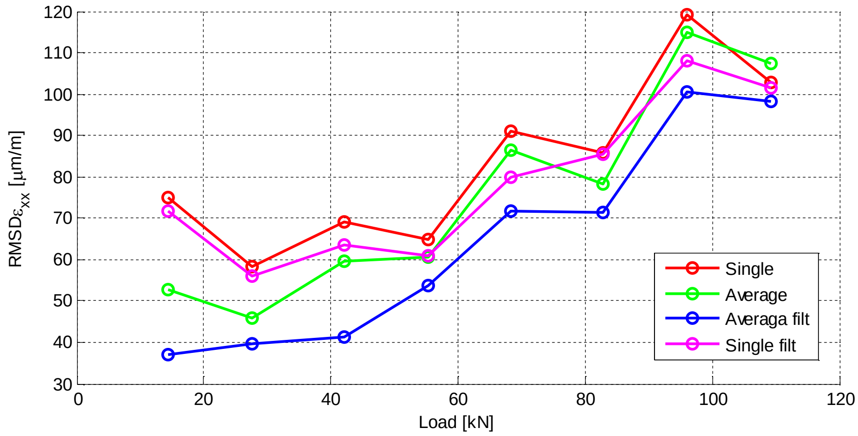

Fig. 4-14 Specimen 2, RMSD εxx for all the tested loading levels

From the RMSD$_{\varepsilon xx}$ analysis of figure Fig. 4-14 it is clearly noticeable how the Gaussian blurring in the image preprocessing is actually able to reduce data dispersion in both the singly acquired analysis (traditional digital image correlation) and in case of image averaging (noise reduction).
In order to better describe the phenomenon, the percentage RMSD$_{\varepsilon xx}$ reduction in case of filtering, average, and filtered average with respect to the singly acquired image with no preprocessing has been computed:

$$RMSD_{\varepsilon_{xx}}\,\text{reduction}\,[\%] = \frac{RMSD_{\varepsilon_{xx}}^{\text{SINGLY ACQ. IMAGES}} - RMSD_{\varepsilon_{xx}}}{RMSD_{\varepsilon_{xx}}^{\text{SINGLY ACQ. IMAGES}}} \cdot 100 \quad \text{eq. 4-2}$$

The data are summarized in Fig. 2-12.

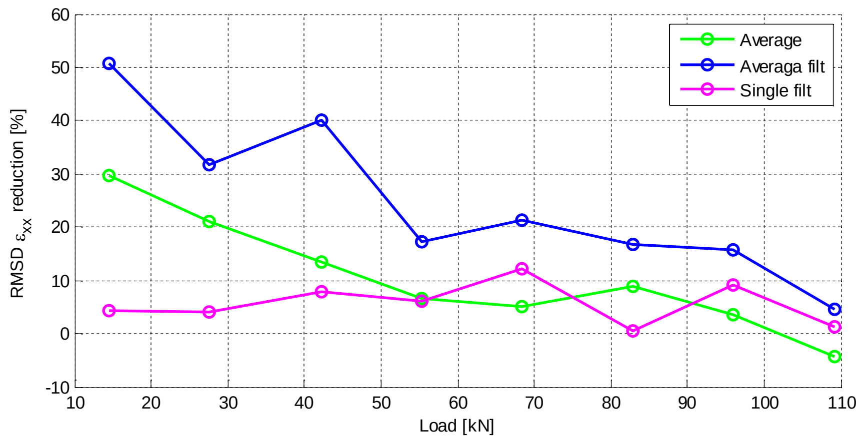

Fig. 4-15 Specimen 2, RMSD εxx reduction for all the tested loading levels

A decrease in the measurement uncertainty of nearly 10% can be observed as a consequence of the only image blurring preprocessing. The combination of filtering and image averaging can lead to reduction of the strain root mean squared discrepancy up to the 50% in case of low strain levels.

Tensile test results: Specimen 3

The third specimen is characterized by traditional dog-bone geometry (Fig. 4-4); Thanks to this characteristic, important considerations about measurement uncertainty will be derived.

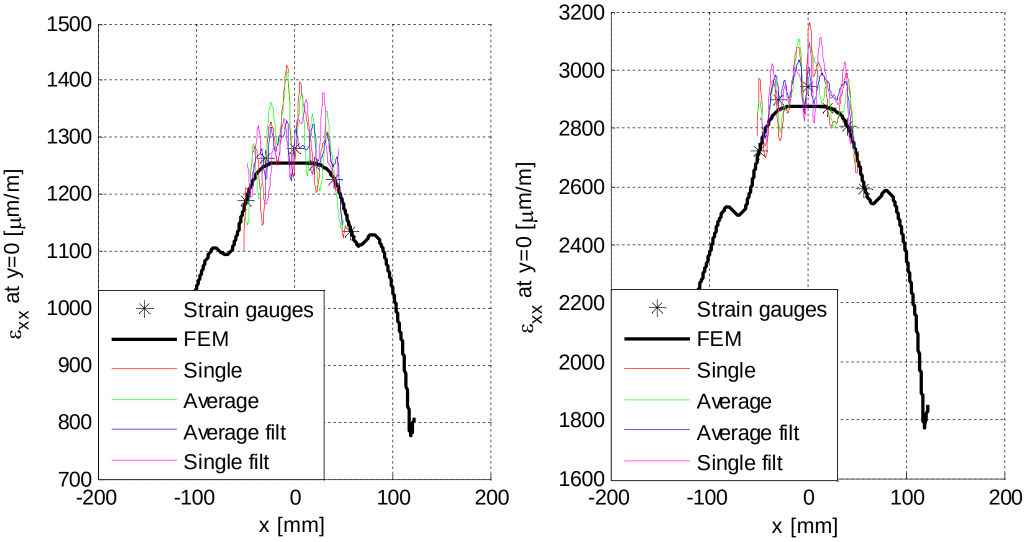

(a) (b)

Fig. 4-16 Specimen 3: axial strain profile along the y=0 axis; low loading level (a, 45 kN) and high loading level (b, 102 kN)

Once again, the predicted versus measured strain profile in the y=0 axis is reported (Fig. 4-16), where it is possible to notice the less variability of the data obtained by the average filtered analysis with respect to the others procedure.

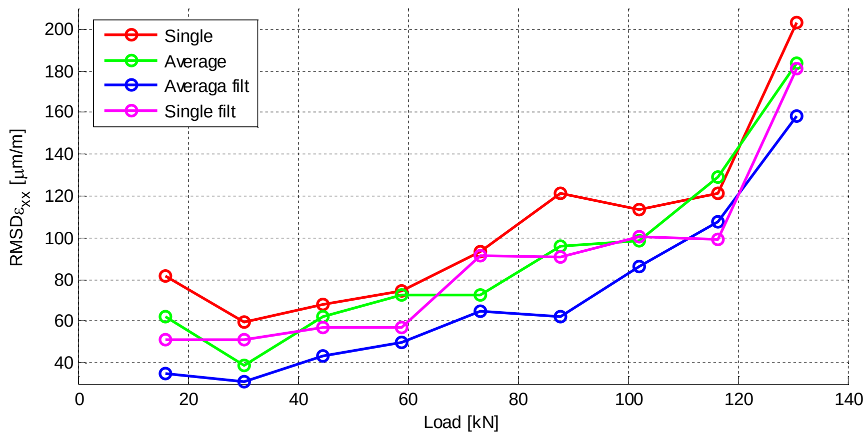

Fig. 4-17 Specimen 3, RMSD εxx for all the tested loading levels

The root mean squared strain discrepancy reported in Fig. 4-17 assumes, in this case, a more important significance with respect to the previous tests: being, in the analyzed area, the strain filed almost uniform, the RMSD$_{\varepsilon xx}$ is able, in this test, not only to provide a quantitative comparison of the average matching

between measured and reference strain field but also to directly quantify the measurement uncertainty.
Once again, the singly acquired non filtered image results in the worst performances, while image filtering is able to increase accuracy both with averaged and non averaged data.
Being the strain field almost uniform in the analyzed area, the strain standard deviation itself can be an important index for the evaluation of the measurement uncertainty associated to the different analyses (Fig. 4-18).

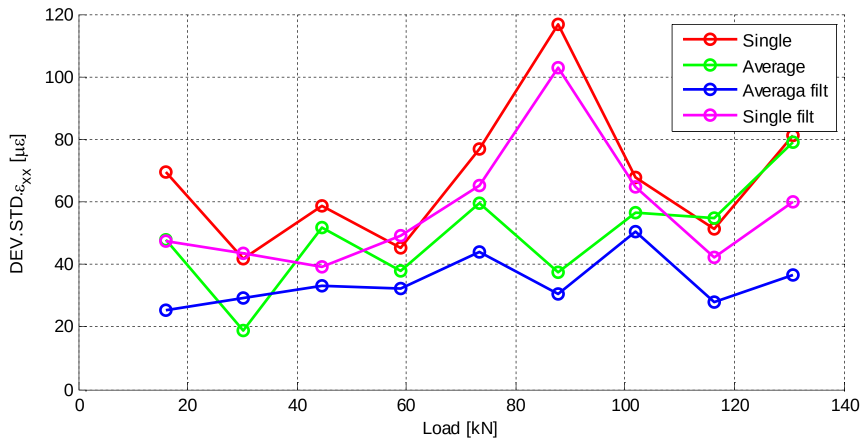

Fig. 4-18 Specimen 3, STD εxx for all the tested loading levels

The lower average values of the data standard deviation in the curves of Fig. 4-18 with respect to the RMSD of Fig. 4-17 indicates that the discrepancy of the measurement results with respect to the reference ones are not only due to data variability, but an average mismatch between the two estimations is preset (mismatch that gets higher increasing the loading level): it is not trivial to attribute this issue to either a bias in the DIC measurements or in error of the f.e. models. Nevertheless, also Fig. 4-18 confirms the capability of image averaging to reduce the measurement uncertainty with respect to singly acquired images; it is worth to notice what happens in the points at 87.7 kN of Fig. 4-18: in the singly acquired images a sudden increase in the data dispersion is present, reasonably associated to issue in the acquired image (vibration of the camera or sudden change in the environmental light) while image averaging does not see this problem. As already noticed, in both the situations image filtering is proven to be effective in reducing the data dispersion.

Tensile test results: Specimen 4
At last, results related to Specimen 4, designed according to U.S. standards for tensile tests, are reported.

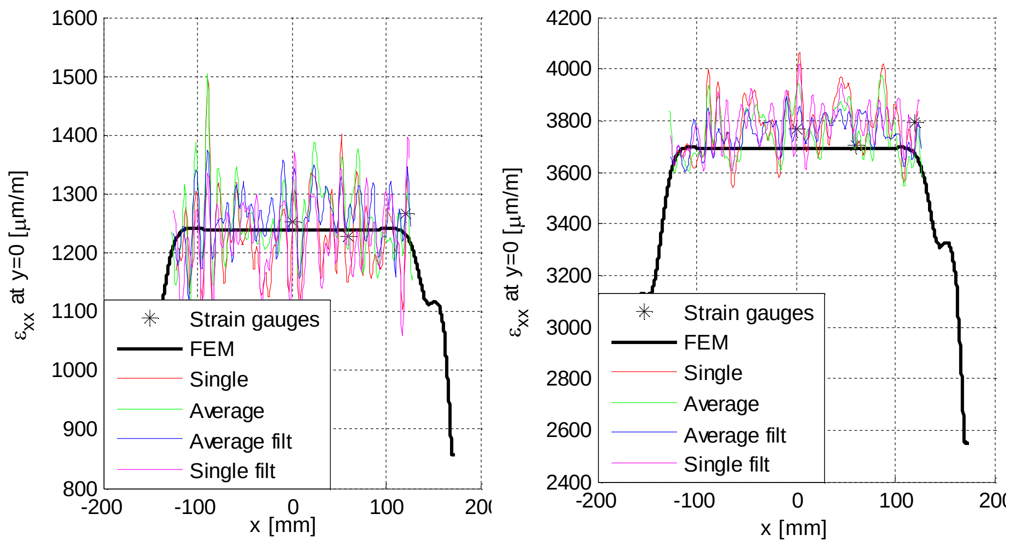

Fig. 4-19 Specimen 4: axial strain profile along the y=0 axis; low loading level (a, 33 kN) and high loading level (b, 98 kN)

A slight mismatch between average estimated and predicted strain is present in this test as well (Fig. 4-19).

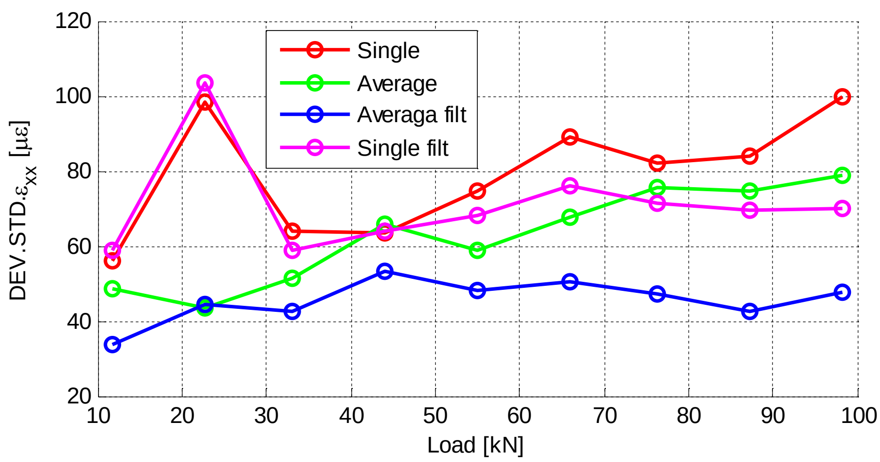

Fig. 4-20 Specimen 4, STD εxx for all the tested loading levels

By looking at the data standard deviation reported in Fig. 4-20, the same consideration reported for the Specimen 3 test can be derived.

4.4 Gaussian blurring in DIC: an application to the study of size effect in GFRP reinforced concrete beams without longitudinal stirrups

The use of corrosion resistant glass fiber reinforced polymer (GFRP) reinforcement in lieu of steel bars is an attractive option for non-prestressed concrete structures that operate in aggressive environments, such as bridges, parking garages, seawalls and docks [121]. Design principles that reflect the peculiar properties of GFRP reinforcement, including its relatively low stiffness and linear elastic behaviour in uniaxial tension up to failure, are fairly well established. Guideline documents [122] followed by codes of practice [123-124] and materials and construction specifications [125-126] have been published in the last decade and are available to practitioners.

The lower axial stiffness of GFRP bars, as compared to steel, results in wider cracks reducing the depth of the uncracked concrete in compression and hindering aggregate interlock along the inclined (shear) cracks, thereby reducing shear strength [127-128]. In addition, size effect, which is defined as the decrease in shear stress at failure at increasing effective depths of the cross section, becomes more of concern [129-131]. Size effect is a widely experimentally studied issue related to reinforced concrete beam without longitudinal stirrups; many empirical laws have been proposed in order to compensate it for from both American and European research groups [132-133] but the reason (i.e. the crack mechanism) of the phenomenon is not yet fully understood.

Two main different theories has been developed in the years by two different research groups to explain this phenomenon and, until now, no final experimental evidences has been reported able to confirm one theory of the other (or both or none of them).

The first is the one proposed in [134-137], where the decrement of the shear resistance in larger beams is explained (both theoretically and by mean of finite element simulations) as a consequence of a modification of the shape of the stress profile in the uncracked part of the structure. In particular, the shear failure mode of a “small beam” most resembles the traditional flexural failure, with an almost uniform stress distribution in the uncracked area while the stress distribution gets steeper and steeper as a consequence of the increment of the size of the beam, leading the structure to a premature failure.

The second theory [138-139] focuses the explanation of the size effect along the crack itself: the interlocking is an important phenomenon in case of small beams, where the aggregate size is comparable with the crack opening while it gets almost negligible for very big beams, where the resulting distance between two faces of the specimen, separated by the cracks, is larger than the aggregates

themselves and the component of the shear load transmitted by interlocking gets null.
In order to deeper investigate the size effect problem in GFRP concrete beams, a joint research between Politecnico di Milano and University of South Carolina has been carried on.
The goal of the research is to tests in 4 point bending beams of different sizes (of the specimen itself and of the aggregate) ad measure on the specimens surfaces the resulting state of strain by means of DIC at various loads in order to:

- qualitatively investigate if there is an actual change in the strain field distribution as a consequence of the change in the specimen dimensions

- quantatively estimate the part of the shear load carried by the uncracked region (numerical integration of the stress profiles obtained coupling the strain profiles measured by DIC and the constitutive law of the material) and, consequently, indirectly evaluate the percentage of the total load transmitted thanks to interlocking

Image blurring as a way to decrease the measurement uncertainty, a critical parameter in an application of DIC on brittle materials (i.e. low strain fields) has been proposed and adopted in these tests.
The whole analysis of the collected data is still a “work in progress” and only preliminary results will be presented here.

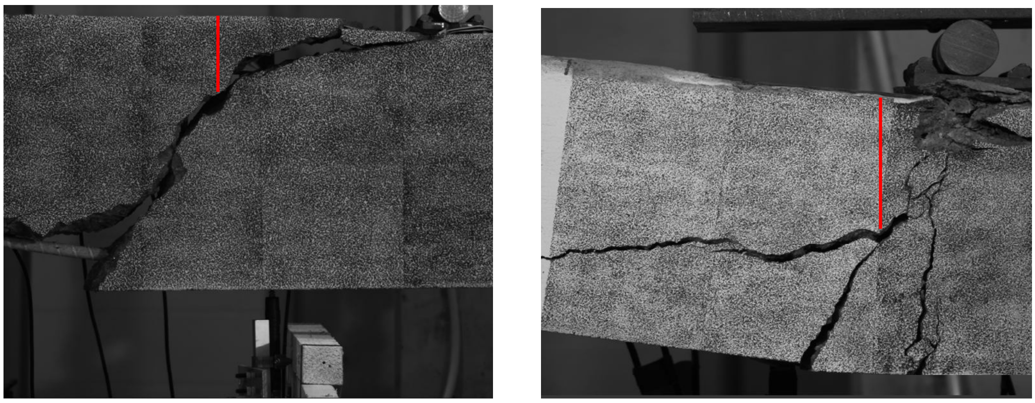

(a) **(b)**

Fig. 4-21 Two tested GFRP reinforced concrete beams at failure: (a) “big beam” (height = 330mm), (b) “small beam” (height = 178mm); in red the position of the extracted strain field profiles

In Fig. 4-21 two tested beams (a “big” and a “small” one) at failure are reported along with the position of the horizontal strain profiles extracted and graphed in Fig. 4-22 where the rainbow colour palette describes the increasing load.

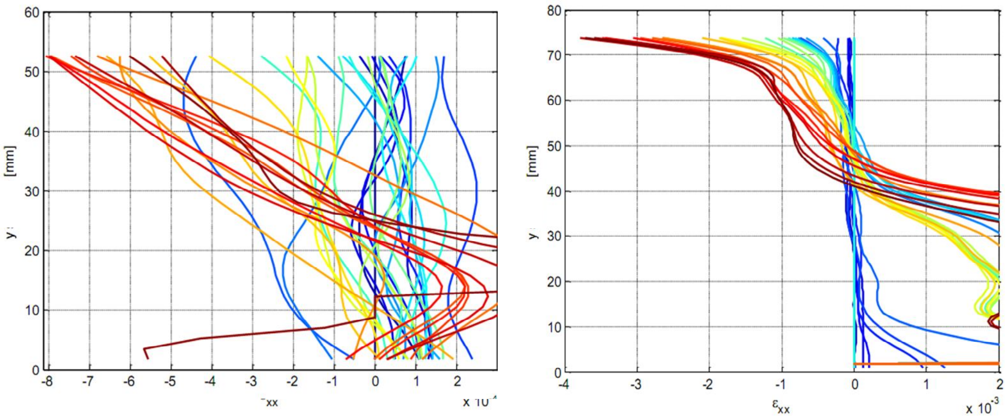

(a) **(b)**

Fig. 4-22 Horizontal strain profiles of two tested GFRP reinforced concrete beams at various loads: (a) “big beam” (height = 330mm), (b) “small beam” (height = 178mm)

It can be macroscopically appreciate the steeper, almost linear, strain profile characterizing the bigger specimen at high loads with respect to the one relative to the smaller beam, where a wider area with a nearly constant state of strain can be easily recognize.
Similar results, obtained from different specimens, seem to confirm the Bazant’s theory but the verification of the percentage of the whole shear load transmitted through the cracks has not be performed yet and will probably return important information in relation to the size effect problem.

4.5 Concluding remarks

In this chapter the use of Gaussian image blurring for uncertainty reduction in digital image correlation, proposed and numerically studied in the previous chapter, has been validate by means of two different experimental tests: rigid motion and controlled strains.
Globally, the reduction in the measurement uncertainty is less pronounced with respect to the results of the simulations. This can be due to both partial blurring in the acquired image (introduced by the optics or inherent in the speckle pattern itself) and external uncontrolled uncertainty sources (camera vibration, out of plane motion, etc.

Nevertheless, a Gaussian low pass filtering of standard deviation equal to 0.75 px has been doubtless identified as an effectively image preprocessing operation able to minimize the resulting measurement uncertainty.

CHAPTER 5

Toner Transfer Technique Applied To Speckle Pattern Realization

5.1 Introduction

As explained in chapter 1, in digital image correlation measurements the measurement surface has to be characterized by a sufficient amount of information, i.e. variation in its colour intensity, in order to allow the algorithm to correctly retrieve its deformation ([1, 3]). This is usually guaranteed by applying, on the measurement surface, an artificial random pattern, “speckle pattern”, generally realized applying small speckles on a uniform background. Speckle pattern characteristics deeply influence digital image correlation accuracy [103-109] and achievable spatial resolution [110, 111] for a given hardware configuration. It does not exist a mathematical formulation of an ideal speckle pattern, that is a “target patter” to be tried to replicate in practice, but many studies suggest important characteristics for a good pattern. For instance, an average diameter of the speckles of few pixels (5-7 px according to [112], 2-5 px in [106], 3 px used in [105]) is known to be sufficient to avoid major aliasing effects in the correlation analysis and still allows to achieve a good spatial resolution. The average percentage of speckles with respect to the background is studied in [107], while in [105] considerations about the grey level distribution of the acquired pattern and its link to measurement accuracy can be found. An alternative approach is proposed in [103], where the average pattern gradient is computed and proved to be directly related to the correlation bias [113] and data dispersion. Different sizes and material of the specimens result in different technological approaches for the realization of the pattern itself, but regardless the techniques, it is non trivial to match in practice the guidelines provided by literature. Spray painting ([3]) is by far the most common technique to speckle pattern realization on medium size specimens (few to some tenth of millimetres): a white paint is applied as background, if necessary, on the specimen and dark speckles are realized by mean of an airbrush (Fig. 5-1). Tuning the viscosity of the ink, the opening of the nozzle and the spraying distance it is possible to vary the resulting speckle size. The density of the speckles is controlled adjusting the spraying time. It is straightforward that such a technique can not allow a real control in the pattern realization. Furthermore, a global match of the specifications in the resulting surface could still imply local areas characterize by low speckles density or, at the opposite, with too clustered blobs (Fig. 5-1). At the same time, skilled users are required to perform the procedure and still the repeatability from one specimen to the other and the quality of the result are difficult to guarantee.

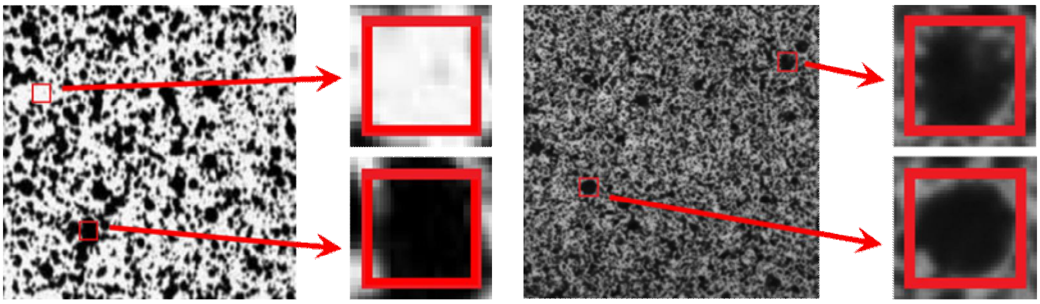

(a) (b)

Fig. 5-1 Spray painted speckle pattern (500x500 px) with low contrast areas, samples of 30x30 px; (a) from Pan et al, [103]; (b) from previous work at Politecnico di Milano

In this chapter, an innovative technique to pattern realization for digital image correlation is presented. The technique is based on the transfer of melted toner from a printed paper to the measurement surface by means of a thermo-mechanical process. The technique is cheap, easy and fast to be applied. The quality of the result is guarantee by a numerical design of the speckle pattern, both in terms of speckle size and density. Furthermore, the procedure ensures a high repeatability of the result. At first, the procedure is fully presented, describing in details all the required steps; then quantitative considerations about the quality of the obtained results are provided; at last, considerations about the applicability of the techniques with respect to specimen dimensions and materials, surface geometry and roughness and testing temperature are provided.

5.2 Toner transfer technique

Toner transfer is a widely diffuse technique in the field of home-making electronic printed circuits boards (pcbs). In this work, the technique is exploited for the first time, as far as the authors known, to provide an efficient method to realize speckle patters on the measurement surface for digital image correlation. At first, the speckle pattern is numerically designed on a calculator. Then the drawing is printed using a common laser printer. Finally the pattern is transferred from the paper to the specimen by mean of a thermo-mechanical process. In the following, all the steps of the procedure will be detailed.

5.2.1 Speckle pattern design

The first step of the procedure implies the speckle pattern design. The speckle shape has been selected to be circular in order to avoid preferential direction of local features. Furthermore, avoiding sharp edges means reducing the high frequency components of the speckle pattern that may alias the measure (during the interpolation of the pattern implied by the correlation algorithm) and, at the same time, it will make easier the pattern realization. An ordinate grid of blobs with a given diameter D_b and center-to-center distance *step*, is numerically generated (Fig. 5-2a). The ordinate grid is then perturbed adding to the horizontal and vertical coordinates of every blob a random amount of noise R extracted by uniform distribution in order to produce an isotropic random pattern (Fig. 5-2b). The approach of perturbing an ordinate grid with respect to randomly placing the speckles in the whole area guarantees a more homogeneous speckle distribution. In the following examples, the diameter D_b is chosen to be equal to 4.5 pixel, as an average of the different recommended values illustrated in literature and previously presented [105, 106, 112]. The grid spacing and the amount of noise are selected in order to match the optimal range of for the covering factor recommended in [107] (40-70%). In particular, a *step* in the ordinate grid equal to 6 pixel and a +/- 2.5 pixel uniform random distribution R result in a covering factor of 42%.

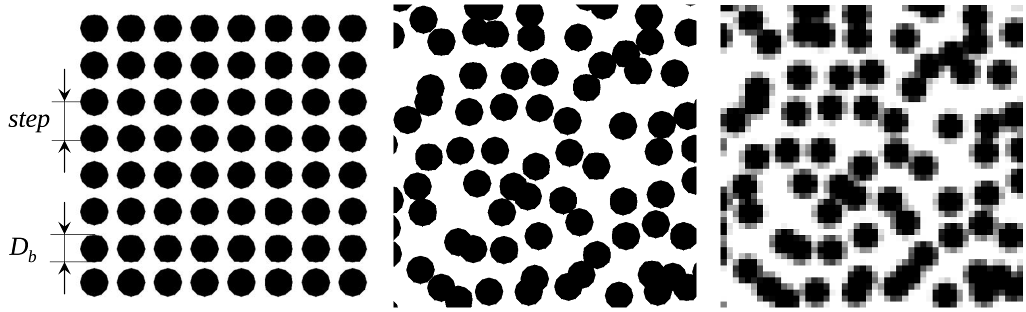

(a) (b) (c)

Fig. 5-2 Speckle pattern design: original ordinate grid (a) and random pattern (b); speckle pattern as it is expected to be framed by the camera (c).

Black speckles on a white background with no intermediate gray levels are designed in order to maximize the pattern contrast, i.e. the signal to noise ration of the measure, and, at the same time, simplify the following steps. It is worth to notice that, even if the pattern is design as binary, this does not imply a binary colours distribution in the final image seen by the camera: the filtering of the optics of the camera combined with a sampling resolution comparable to the blob diameter will smooth the dark to light transition blurring the contours of the speckles. In Fig. 5-2c the generated speckle pattern, as it is expected to be seen by the camera, is reported.
Vectorial image representation has to be preferred to raster during the pattern design in case, in the printing phase, the resulting speckle dimension approaches the limits of the used printer in order to avoid loss of information.

5.2.2 Speckle pattern printing

The second step of the procedure implies the printing of the previously designed pattern. The ratio between camera resolution (pixel) and measurement area (mm) sets the mm to pixel scaling factor.
Any standard laser printer can be exploited; high quality printers (usually characterized by higher dpi resolution) have to be chosen only in case the resulting scaling factor exceeds the resolution limit of standard machine. In the present work, a Lexmark T 653 dn is used. It is suggested to set the highest quality during the printing and to print a test page just before the pattern in order to warm up the printer. If no laser printers are available, the same results can be achieved printing the pattern on an inkjet printer and photocopying it with a laser copier. The printing support has to be carefully selected: the toner has to melt during the printing without straining the sheet and stick on the paper but not penetrate, so that it will be possible to transfer it on the measurement surface in the following step. Typically, glossy photographic papers designed to work with inkjet printers allow to obtain better results.

5.2.3 Toner transfer

The last step is the transfer of the toner from the paper to the measurement surface. The measurement surface has to be smooth and clean (the use of acetone is suggested). In case the material of the specimen is characterized by dark or reflecting texture, it is suggested to spray a thin layer of white opaque enamel to increase the pattern contrast and avoid reflections (the toner itself will be opaque). This operation can be avoided if the base surface is sufficiently light and free form specular reflection. The toner transfer can be done laying down the printed sheet on the specimen and warming it up applying a uniform pressure: the heat will re-melt the toner on the paper and the pressure will force it to adhere on the specimen. Toner powders melt at about 70-90 °C; a temperature slightly over 100°C is sufficient. From a practical point of view, a common iron with the operator pushing on it and a cloth between the hot surface and the specimen is found to be the best solution to carry out the operation. The time required is strongly influenced by the thickness of the specimen and the thermal conductivity of the material: about three minute on a 5mm aluminium plate is found to be a reasonable time interval. At the end of the operation, the specimen can be cooled in cold water: this operation make easier the removal of the original paper.

5.2.4 Procedure calibration

Through the whole process, a slight variation from the design speckle diameter to resulting one may occur. For this reason, it is suggested to perform a calibration of the procedure in order to be able to modify the original design taking into account this bias induce by the procedure. For this porpoise, ordinate grids of blobs with decreasing nominal diameter (from 1.00 to 0.05mm, which was found to be the lower limit with the available hardware) are designed, printed and transferred on the final surface. Successively, the surfaces are scanned with a high resolution scanner and a particle analysis is performed on the blobs. The average equivalent diameter of every blob in a grid and its range of variability are computed for every nominal diameter.

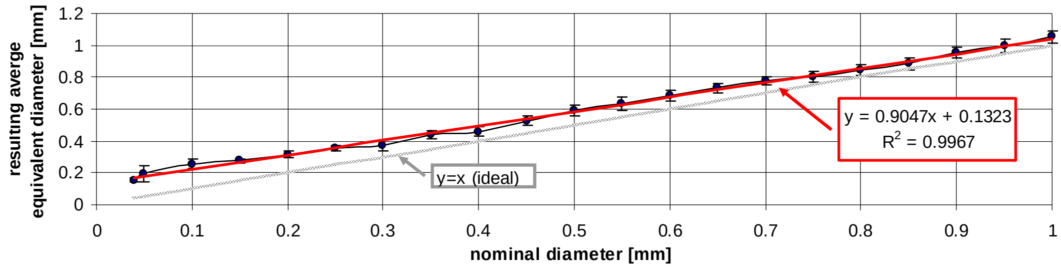

Fig. 5-3 Toner transfer calibration

The results are graphed in Fig. 5-3, where the error bars represent the data standard deviation. An average increase with respect to the nominal diameter can be noticed, and its magnitude increases as the speckle dimension decreases. A least squared regression curve is computed: the inverse of the curve is used to compensate the speckle pattern design.

5.3 Toner transfer: quality assessment

The previously designed speckle patter, correcting the diameters according to the procedure calibration, is printed at the four different scale levels, summarized in Table 5-1 (setting a speckle diameter of 4.5 px, as previously discussed):

	Scale factor [px/mm]	Blob diameter [mm]
Pattern 1	3.75	1.2
Pattern 2	5.00	0.9
Pattern 3	7.50	0.6
Pattern 4	15.0	0.3

Table 5-1 Scale factor of the tested specimens

Successively, the patterns are reported on four aluminium specimens. The base surface has been previously spray painted with a light film of white opaque enamel to increase the resulting pattern contrast. The specimens are framed with a digital gray-scale 8-bit camera preserving the px/mm scale factor reported in Table 5-1. Particular attention has been paid during the image acquisition not to locally saturate the sensor. A sample of 100x100 px for every realized pattern is reported in Fig. 5-4.

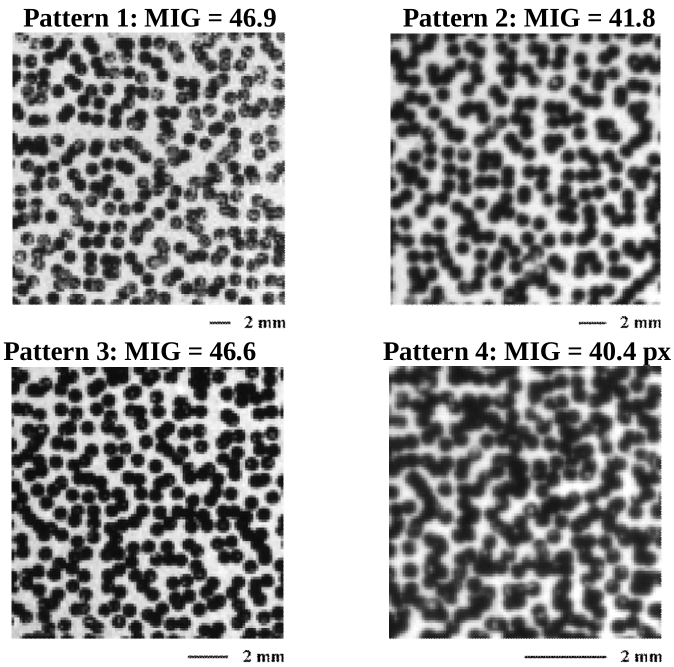

Fig. 5-4 Speckle patters realized at four different scale levels; samples of 100x100 px

The high quality of the obtained speckle patterns is clearly visible, in terms of image contrast, pattern details and uniformity. In order to provide a quantitative evaluation of their quality, the mean intensity gradient coefficient [103] is computed.

The modulus of the local gradient intensity vector of a gray-scale image can be defined as:

$$\left|\nabla f\left(x_{ij}\right)\right| = \sqrt{f_x\left(x_{ij}\right)^2 + f_y\left(x_{ij}\right)^2} \qquad \text{eq. 5-1}$$

where $f_x(x_{ij})$ and $f_y(x_{ij})$ are the x- and y-directional intensity derivates at pixel x_{ij}, computed using central difference approach. The mean intensity gradient is consequently defined as:

$$MIG = \sum_{i=1}^{W} \sum_{j=1}^{H} \frac{\left|\nabla f\left(x_{ij}\right)\right|}{W \cdot H} \qquad \text{eq. 5-2}$$

where W and H are image width and height (in px). This parameter has been introduced for the first time in [103] and was proved to be an effective global parameter to asses the quality of the speckle pattern for digital image

correlation. In particular, higher values of the MIG coefficient imply lower bias and less dispersion in the DIC measurements.
The MIG coefficient is computed for the four realized specimens and is reported in Fig. 5-4. Pattern 1 and Pattern 2 show very similar values of MIG, about 47. The other two patterns result in slightly lower values (about 41), probably related to the soft blurring present in the acquired image due to a non perfect focus of the optics. In any case, in all the specimens, the resulting MIG coefficient is higher than 40 pixels: this value is above the best pattern tested in [103], realized with standard technology (spray painting).
As explained, the MIG coefficient is a parameter able to characterize the pattern quality of the whole framed image. Further investigations of the pattern quality are required with standard techniques ([110, 111]), where a high value of the MIG coefficient could still hide small local areas characterized by very low contrast (e.g. areas with not enough or too close speckles, that may result by the random process of a spray painting technique). With the pattern realization technique proposed in this work, the uniformity of the obtained speckles in the whole working area is instead guaranteed by the numerical design of the pattern, that is once the required characteristics are matched locally, it is easy to extend them to the whole area.
It is worth noticing that the designed pattern is, in this example, numerically built according to the guidelines articulated at the beginning of the previous paragraph, and recommended in literature; being able, by means of toner transfer, to realize every designed patter, it could be possible to optimize the pattern design, for instance maximizing the MIG coefficient or with similar approaches. It is not the aim of this paper to face pattern optimization but to provide a technique able to generate a high quality fully controlled patter.

5.4 Toner transfer limits: material, surface characteristics, speckle size and temperature

To create the speckle pattern with the technique proposed in this work, the surface of the specimen has to be heated at about 100°C for few minutes, so toner transfer can be obviously exploited only if this operation does not modify the material properties. The technique has been successfully applied to various metals (iron, aluminium, manganese and copper alloys) and to concrete (Fig. 5-5a in a high resolution picture) and mortar specimens.
In order to apply the procedure, small surface roughness is required by the transfer phase. In the examples showed in the previous paragraph, plate specimens were considered. The technique can be easily applied on cylindrical specimens as well, simply rotating the heating source along the measurement

surface (Fig. 5-5b, on a 16 mm diameter beam), where traditional spray painting is generally non trivial.

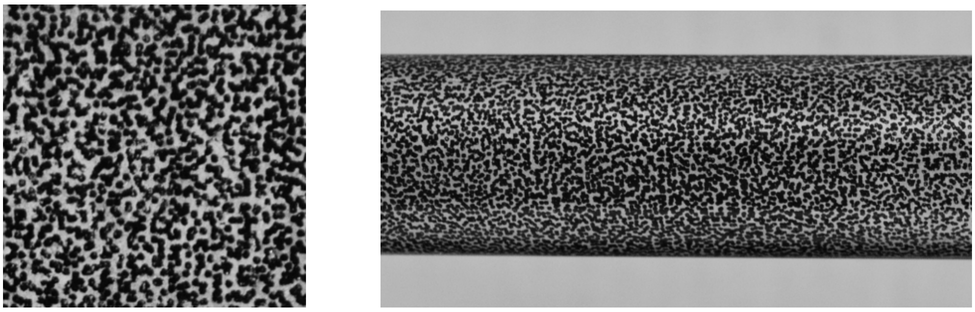

(a) (b)

Fig. 5-5 Toner transfer apply on a concrete surface (a) and on a aluminium cilinder (b)

In theory, there are no limitations to the maximum size of the speckle pattern that can be obtained with the proposed procedure. Nevertheless, for very large specimens (order of magnitude of 1 m and more) the toner transfer may required a lot of time to be applied with no sensible expected improvements with respect to traditional techniques: for a given hardware, and increase of the measurement area results in lower pixel/mm scaling, i.e. bigger speckle that can be effectively realized using spray painting with stencils. At the opposite, a lower boundary of the proposed technique is drawn by the minimum speckle diameter that can be effectively printed by the printer. As shown during the procedure calibration, for the tested hardware the minimum speckle size is found to be about 0.15 mm; associating to it an equivalent diameter of 4.5 pixel, this lead to a scale factor of 30 pixel / mm, i.e. a framed area of about 7 x 3.5 cm for a 2Mpixel camera; this result is obviously function of the dpi resolution of the printer, but its order of magnitude can be an useful information for standard machines. The whole range of applicability (from few tens to some hundreds of mm) is particularly attractive for full filed strain measurements because it matches the most common dimension of samples tested in a tensile machine as well as standard concrete cylinders used for compression tests.

Speckle pattern realized by means of toner transfer has been successfully exploited for high temperature application: the experimental evaluation of heat induced strains in an aluminium plate in the temperature range between 22 and 450 °C (70% of its nominal melting temperature). The plate specimen is placed in an oven, which is opened at given temperature steps during the test to allow image acquisition (13 steps in total). In order to avoid drops in the temperature of the plate, the specimen is protected by a glass-ceramic box and its actual temperature is monitored using thermocouple inside a hole in the plate itself. The used camera is able to acquire images at 200 Hz at VGA resolution (640x480 pixel); a blue band pass (450-490 nm) optical filter is mounted in front of the optics in order to avoid issues related to specimen emission in the near infrared during the test as suggested in [140] and lighted by means of led white light (presenting a peak in the emission spectrum in correspondence of the bandwidth of the filter, [141]).

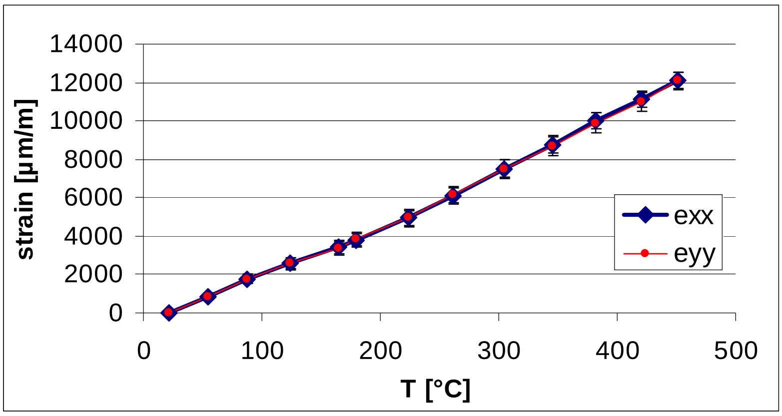

Fig. 5-6 Temperature induced strains in a aluminium plate

Before the test, 400 frames (2 s of acquisition) of the surface are acquired and their average is used as the reference image for the following steps; this procedure is implemented in order to reduce the noise in the reference image [142]. At every temperature step, 400 images are acquired and the digital image correlation resulting strain matrixes are averaged element by element in order to suppress the fictitious strain contribution associated to image distortions induce by the hot air flows [143]. The selected subset size is equal to 21x21 pixel, step of 5 pixel (i.e. overlap of 75%). In Fig. 5-6 the results of the test are reported for both horizontal and vertical strains. The error bars are computed, at every step, as standard deviation of the resulting average strain matrices. Thanks to the high quality and stability of the pattern, the DIC analysis has been carried out in the whole range (strains up to 1.2%) without the need to perform incremental correlation.

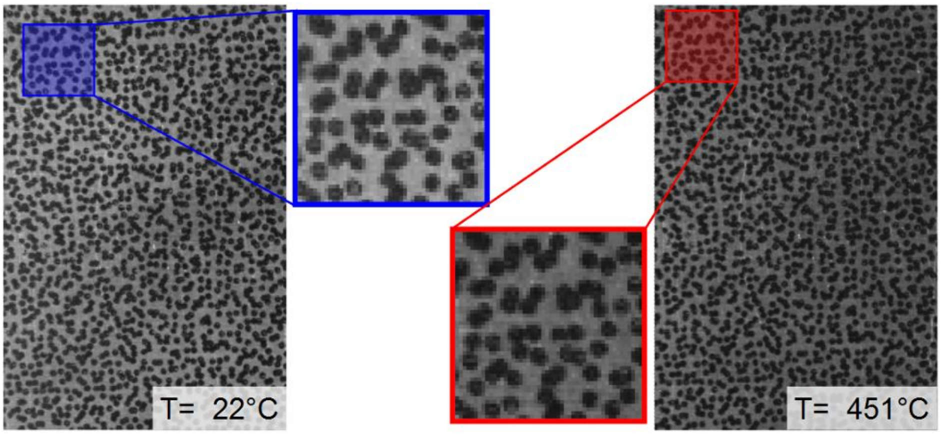

(a) **(b)**

Fig. 5-7 Speckle pattern realized by toner transfer during a high temperature test: 300x200 px samples of the reference image at room temperature (a) and of the frame acquired at the highest tested temperature (b); zoomed area of 50x50 px

The test lasted about 3 hours; in Fig. 5-7 two images acquired by the camera, one at the beginning and one at the end of the test, are reported. Comparing the two images, no degradation of the pattern due to the exposure to high temperature can be observed. At the same time, a global offset in the image intensity can be appreciated: this is a consequence of the change of the environmental light during the three hours. This problem, common in DIC measurements, is well known in literature and can be easily handled during the correlation process using the zero-normalized cross-correlation (ZNCC) [1, 3, 144]. Since that the MIG index is sensitive to the modifications in lighting conditions, it was not used in this situation.

In order to assess the stability of the speckle pattern characteristics during the test, an approach derived by the zero-normalization of the DIC correlation criterion was used: considering one acquired image, every subset is extracted and zero-normalized subtracting the average intensity value and dividing the result by the intensity standard deviation:

$$S_{ZN}(i,j) = \frac{S(i,j) - \bar{S}}{\sigma_S} \qquad \text{eq. 5-3}$$

where $S(i,j)$ represent the intensity value of a pixel of a (2M+1)x(2M+1) squared subset, $S_{ZN}(i,j)$ its normalized version, $\bar{S}$ the average subset intensity and σ_S its intensity standard deviation:

$$\bar{S} = \frac{1}{(2M+1)^2}\sum_{i=-M}^{M}\sum_{j=-M}^{M} S(i,j) \qquad \text{eq. 5-4}$$

$$\tilde{S} = \sqrt{\frac{1}{(2M+1)^2 - 1}\sum_{i=-M}^{M}\sum_{j=-M}^{M}\left[S(i,j) - \bar{S}\right]^2} \qquad \text{eq. 5-5}$$

Successively, the MIG parameter is computed separately for every normalized subset. In this way, on one hand it is possible to quantitatively estimate the quality of the speckle pattern getting rid of the lighting problems thanks to the zero-normalization and, on the other hand, for every frame the average value of the mean intensity gradients of the about 5000 normalized subsets can be computed along with the associated variability range. If the variability within the single frame exceeds the differences of the average values between one frame and the others, it can reasonably be stated that no significant variation occurred.

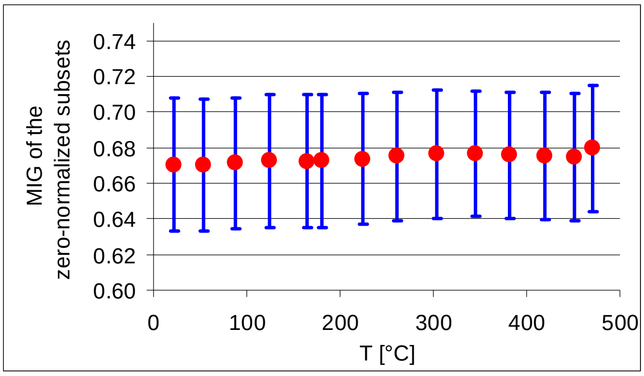

Fig. 5-8 High temperature test: Mean Intensity Gradient of the zero-normalized subsets

By looking at the results of this approach graphed in Fig. 5-8 (where the subset dimension and step have be naturally selected equal to the ones of the DIC analysis), it can be noticed at first the different order of magnitude with respect to the value of the MIG coefficient presented in the previous paragraph: this is a natural consequence of the normalization process, the values computed with the presented procedure are not directly comparable with the ones obtained by the standard MIG computation. By comparing the average computed values at different temperature in Fig. 5-8, it can be clearly observed that the differences among different frames are negligible with respect to the variability inside a given image: it is consequently possible to state that no sensible pattern worsening occur as a result of the heating process.

5.5 Concluding remarks

Speckle pattern characteristics are proven to deeply influence digital image correlation measurement accuracy. Commonly exploited technologies for its realization are hardly able to guarantee a high quality results. In this work toner transfer, an innovative technique for DIC speckle pattern realization, is presented together with some application in different experimental conditions. The technique implies a first step where the pattern is numerically designed; in this phase, the desired characteristics of the resulting pattern can be tuned both in terms of speckle size and dispersion. After that, the designed pattern is printed and transferred on the measurement surface. The proposed technique has been proven to be able to guarantee high quality results and their repeatability. The main limitations of the technique are linked to the necessity to heat the measurement surface to apply the patter at about 100°C for a few minutes. When this aspect does not represent an issue, toner transfer has been proved to be a fast and easy method to realize the high quality speckle patterns. The technique is flexible in specimen dimension, material and surface shape. Furthermore, its exploitability in high temperature tests (up 450°C in the application described in this chapter) has been presented; a very good stability of the MIG of the normalized subsets demonstrate that the pattern did not undergo to appreciable degradation when exposed to high-temperature, as it was reasonable to hypothesize by looking at the images of Fig. 5-8.

CHAPTER 6

Speckle Pattern Optimization

6.1 Introduction

In the introduction to the previous chapter, paragraph 5.1, it has been extensively explained how, according to the recent literature, the quality of the speckle patter deeply influences the final accuracy and the achievable spatial resolution of measurements made by means of digital image correlation.

An innovative technique for the realization of speckle patterns, “toner transfer”, has been proposed in paragraph 5.2. The technique has been proven to be simple, cheap, fast and flexible in terms of testing temperature range and materials, dimensions and geometrical characteristics of the tested surface. It was also proved that toner transfer allows the realization of high quality speckle patterns. An important characteristic of the proposed technique is that the final pattern is numerically designed and it can be consequently optimized, further increasing the measurement accuracy.

In this chapter, the optimization of the speckle pattern, aimed to the reduction of the measurement uncertainty, is addressed. In paragraph 6.2 a theoretical study is presented, where the optimized geometrical characteristics (speckle size and density) are derived on the basis of detailed assumptions, maximizing the mean

intensity gradient, M.I.G., of the speckle pattern. This coefficient has been introduced in [103], where it is proved to be an effective global parameter to asses the quality of the speckle pattern for digital image correlation, and has already been mentioned in paragraph 5.3. In the optimization process, the results related to image filtering presented in chapters 3 and 4 are fundamental.
These results of the optimization are experimentally verified in chapter 6.3 by means of in plane translation tests similar to the ones presented in paragraph 4.2. In particular, the robustness of the theoretically obtained characteristics with respect to the signal to noise ratio in the collected data is proven to be an important parameter for speckle pattern quality assessment.

6.2 Speckle pattern optimization: theoretical study

In this paragraph, the speckle pattern design is optimized. The pattern performances are evaluated, varying speckle diameter and density, on synthetic images and the optimization is carried out maximizing the resulting mean intensity gradient [103].

6.2.1 Model hypotheses

The optimization is performed starting from the following hypotheses:

a) **The pattern is random;** this consideration is obvious, considering the working principle of digital image correlation (paragraph 1.3), but state of the art parameters for speckle pattern quality assessment consider the pattern randomness an hypothesis itself and do not verify it.

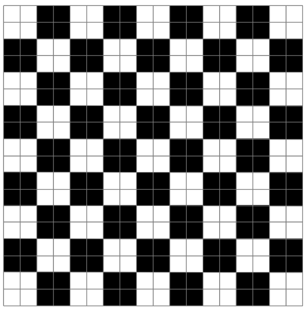

Fig. 6-1 Example of non random pattern: a two-px ordinate grid

For instance, the M.I.G. coefficient of the two-px width ordinate grid of Fig. 6-1 is about 180 px, i.e. more than three times the best pattern tested in paragraph 5.3, but it is obviously unsuitable for a DIC application.

b) **The pattern is binary,** i.e., ideally, with pure black speckles on a pure white background with no intermediate grey levels in the design. This hypothesis is link to the will to maximise the MIG coefficient and, at the same time, maintain as easy as possible the speckle pattern realization. As explained in paragraph 5.2.1 a binary design does not imply a binary colours distribution in the final image seen by the camera: the filtering of the optics combined with a sampling resolution comparable to the blob diameters smoothes the dark to light transition and blurs the contours of the speckles. Furthermore, the image blurring proposed in chapter 3 and here implemented increases this effect.

c) **The speckles are circular;** this hypothesis is made, as in paragraph 5.2.1, in order to avoid directionality of the local features and high frequency components in the resulting pattern that may alias the DIC analysis and, at the same time, simplify the pattern realization.

d) **All the speckles have the same diameter;** in order to simplify the analysis the randomness of the pattern is guarantee randomly distributing the speckles, not changing their shape or dimension. Furthermore, only fixing a diameter for a given a pattern it is possible to study which is the optimal one.

e) **The speckles are not in contact with each other;** this assumption obviously increases the resulting mean intensity gradient by assuring the maximum number of dark to light transition. It is worth noticing that this is the main difference between the patterns analyzed in this chapter and the ones presented in paragraph 5.2.1.

6.2.2 Pattern design and rendering

Starting from the mentioned hypotheses, a family of synthetic speckle pattern is created, varying the nominal diameter and the average distance among speckles, and the mean intensity gradient of every pattern is computed.

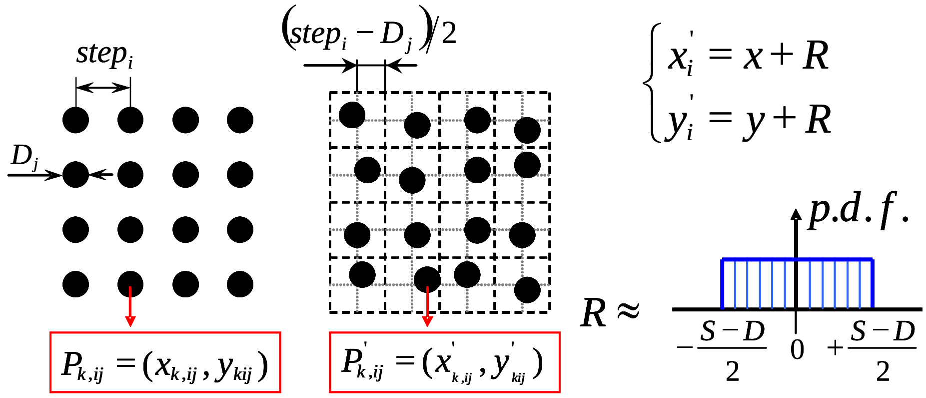

Fig. 6-2 Pattern design: initial ordinate grid (a) and perturbed grid (b), with maximum allowable amount of perturbation

The implemented simulation strategy is described in Fig. 6-2. At first, for a given speckle diameter D_j and grid step $step_i$, an ordinate grid of blobs is created (Fig. 6-2a). In order to satisfy the first hypothesis (random pattern) preserving the last one (the speckles are not in contact with each other), the position $P_{k,ij} = (x_{k,ij},y_{k,ij})$ of every k-th speckle is perturbed by adding to every blob coordinate a random amount extracted from an uniform distribution R of amplitude $step_i$-D_j (Fig. 6-2b). In this way, $step_i$ and D_j are the only degrees of freedom of the model.

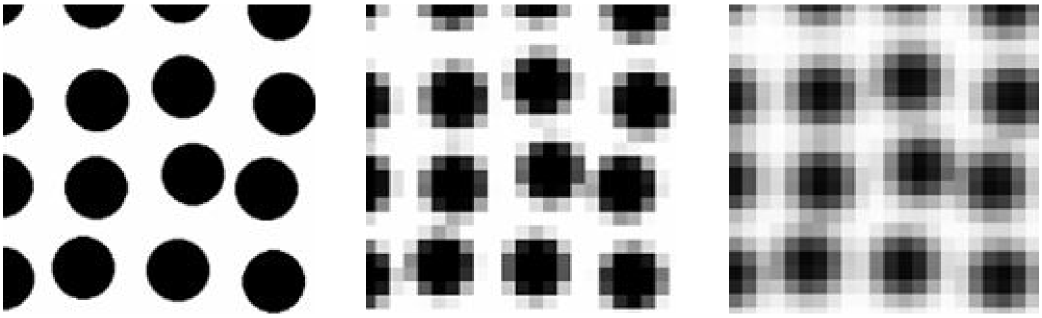

(a) **(b)** **(c)**

Fig. 6-3 Rendered high resolution image (a), actual resolution image (b), and blurred image (c)

The images are rendered at 10 times their target resolution (Fig. 6-3a), following the same approach presented in chapter 3.2, in 10000x10000 px raster images. These high resolution patterns are then anti-aliasing filtered and down-sampled to their actual resolution (Fig. 6-3b, resulting in a 1000x1000 px image), and eventually blurred by means of a Gaussian filter, σ = 0.75 px. The last operation is fundamental for the correct estimation of the pattern quality: high frequency components may increase the average image gradient but were proven to be misinterpreted by digital image correlation algorithms. For this reason, the analyzed patterns are blurred according to the optimal filter level obtained in chapter 3.

Diameters D_j from 2 to 20 px, increment 0.5 px, are tested. For every diameter, a $step_i$ ranging from D_j + 0.2 px to D_j+2.2 px is investigated. Smaller steps imply nearly regular grids that result in a wrong estimation of the initial guess by the DIC algorithm. Bigger steps decrease the density of the speckles, i.e. the resulting pattern gradient.

6.2.3 Optimization results

1147 high resolution patterns are rendered, down-sampled and blurred and for every resulting 1000x1000 px image the mean intensity gradient is computed.

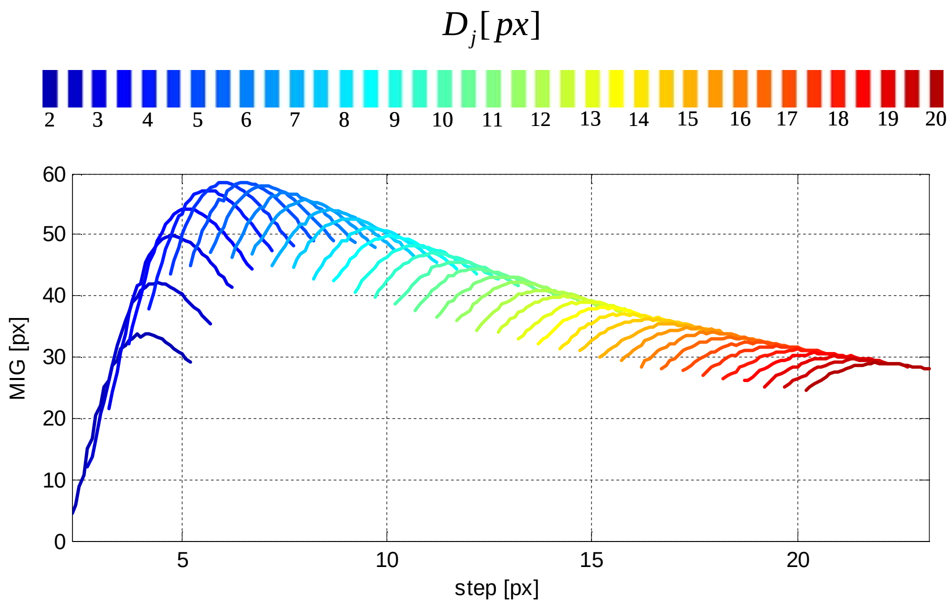

Fig. 6-4 Pattern optimization: MIG coefficient varying speckle diameter and pattern step

The results are graphed in Fig. 6-4. Different curves (different colours) are related to different speckle diameter, as explained in the graph legend. For every diameter, the respective curve describes the variation of the mean intensity gradient of the synthetic pattern with respect to the grid step. The highest MIG coefficient is obtained for a speckle diameter equal to 4.5 px and a grid step equal to 6 px. These characteristics represent the best speckle pattern under the previously explained hypotheses according to the presented analysis. It is possible to notice that the MIG coefficient decreases steeply for steps and diameters lower that the optimal ones, while the decrement is less important for bigger and more separated speckles.

6.3 Experimental validation

In order to validate simulation strategy presented in paragraph 6.2 and confirm the obtained results, experimental tests has been designed and carried out. Seven patterns among the ones numerically generated in the previous paragraph are printed on a rigid surface and framed by a digital camera. By moving the camera parallel to the surface, it is possible to replicate a rigid in-plane movement of the patterns. In this way, all the points of the surface are subjected to the same amount of translation. Analyzing, for every printed pattern, the dispersion of the digital image correlation displacement data resulting by the analysis of the acquired images, an uncertainty of the measurements associated to every pattern can be computed. In this way, it is possible to verify if the MIG is actually able to provide correct information about the way to minimize the measurement uncertainty and validate the results of the theoretical analysis.

6.3.1 Tests design and realization

Seven points, i.e. seven differently designed patters, are selected (Fig. 6-5) from the data presented in Fig. 6-4.

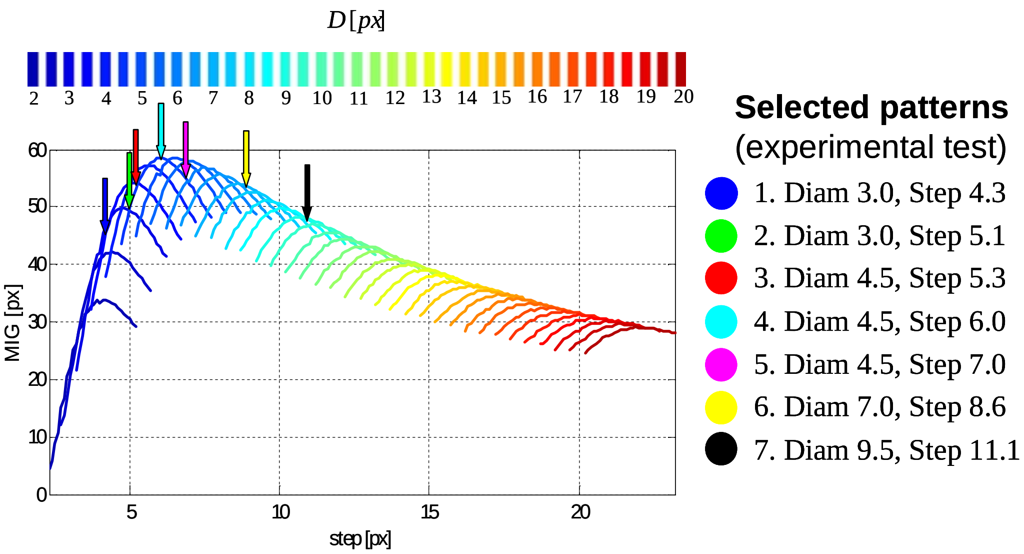

Fig. 6-5 Experimental tests: selected patterns

The first selected pattern (number 4, 4.5 px diameter and 6 px step point) is the one characterized by the highest value of the MIG coefficient, so theoretically the best one for a DIC application, able to minimize the measurement uncertainty. Other two patterns are extracted from the 4.5 px curve: number 3 and number 5, respectively at a lower (5.3 px) and higher (7.0 px) steps with respect to the maximum of the 4.5 px diameter curve. Patterns number 2 (*D*=3 px, *step*=5.1 px) and number 7 (*D*=9.5 px, *step*=8.6 px) are extracted from lower values of the MIG curves and number 1 (*D*=3 px, *step*=4.3 px) and number 7 (*D*=9.5 px, *step*=11.1 px) represent the solutions farthest from the optimal area that will be here considered. An additional pattern is included in the following tests (“old patter”): it is designed according to the guidelines provided in paragraph 5.2.1 of the previous chapter, i.e. without respecting the last hypothesis (“the speckles are not in contact with each other”) of paragraph 6.2.1. The rendered high resolution images of the selected patterns are printed on an A3 (297 x 420 mm) sheet (Fig. 6-6) and fixed on a rigid surface.

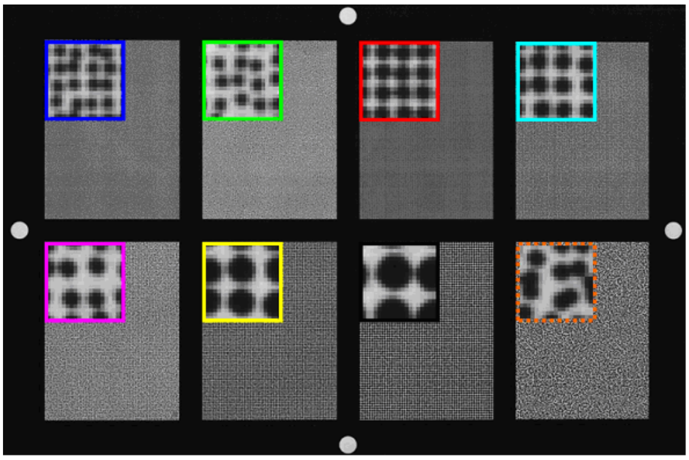

Fig. 6-6 Printed A3 sheet with the 8 selecetd patterns for a rigid motion test

A 3296 x 2472 px greyscale digital camera frames the printed sheet (the figure Fig. 6-6 is actually a frame grabbed by the camera). The four white big blobs of Fig. 6-6 are used to place the sensor of the camera parallel to the printed surface using the pose estimation algorithm presented in chapter 2. The distance between the camera and the target (about 1.5m with a 55mm optics) is tuned in order to match the nominal diameter of the speckles in the patterns. Every patter is contained in an area of about 600 x 800 px. The optimal focus is estimated by means of the MF-DCT algorithm of paragraph 2.3. The resulting scaling factor is about 10 px/mm.
The camera is mounted on a micrometric slide (Fig. 6-7).

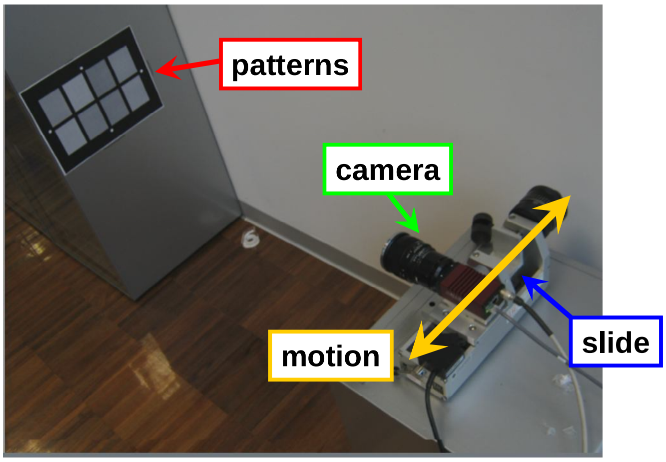

Fig. 6-7 Rigid motion test

By rotating the micrometric screw, it is possible to translate the camera on a plane parallel to the one of the patterns. This motion of the camera can be used to simulate a rigid in-plane translation of the target.
51 different displacements, from 0 to 0.25mm, 0.005 mm step (i.e. from 0 to 2.5 px, step 0.1px) are imposed to the camera and for every position one image is acquired. All the collected images are then filtered with a σ=0.75 px Gaussian filter, according to the results of chapter 3, in order to reduce the measurement uncertainty and eliminate the subpixel bias of the following DIC analysis.

6.3.2 Tests results

The filtered images are processed by a digital image correlation algorithm in order to estimate, at every step, the apparent motion of the target. The analysis is carried out with a 21 x 21 px subset size, overlap 66.7% (i.e. a 7 px step between subsets) [3]. An eight-tap optimized interpolation method is implemented and a zero-normalized sum of squared difference correlation criterion is selected to compensate for the scaling and offset in the intensity pattern [3]. The results are 51 displacements matrices, one for every displacement imposed to the camera, and the analysis is repeated 8 times, one for every pattern. Every displacement matrix includes about 10000 measurement points (resulting by a 600x800 px area analyzed with a step of 7 px).

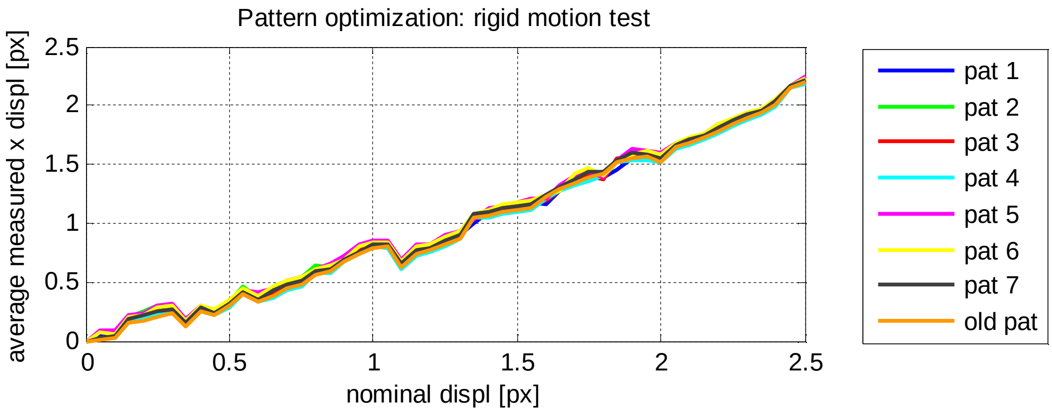

Fig. 6-8 Pattern optimization, rigid motion tests: average measured displacements along the x direction for every pattern

The average value of every displacement matrix is computed for every pattern. The results are graph in Fig. 6-8 with respect to the nominally imposed translation. It possible to see how the exploited hardware is not able to guarantee a real low uncertainty reference: relatively high discrepancies can be notice between imposed and measured displacements. These can be reasonably attributed to plays in the micrometric screw and vibrations of the support of camera. Anyhow, the reason to use a micrometric slide was to be able to test the whole subpixel region, not really to impose exact displacements as in chapter 4, and this result is undoubtedly achieved: 51 samples, nearly uniformly spread in a 2.5 px range, are collected.

The really important information of Fig. 6-8 is that the displacement data of all the patterns results in the same average value for every position: all the curves are perfectly overlying. This means that the fundamental hypothesis of the test (the camera is moving parallel the measurement surface, so every point is subjected to the same apparent displacement) has been respected. In this way, being the motion field uniform, it is possible to compute, for every pattern, the dispersion of the associated data and provide information related to how the measurement uncertainty varies changing the pattern design.

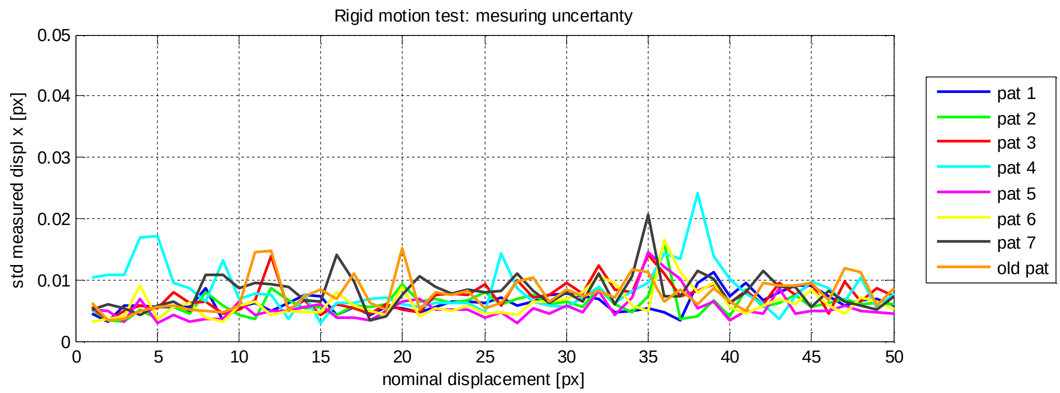

Fig. 6-9 Pattern optimization, rigid motion tests: standard deviation of every measured displacement matrix

The standard deviation of every x displacement matrix is computed for every pattern. The results are graphed in Fig. 6-9. The resulting uncertainty can be quantified in the order of 0.01 px, regardless the analyzed pattern. This means that, in the performed test, no differences can be really appreciated varying the pattern design: the measurement uncertainty seems not to be related to the mean intensity gradient of the pattern and, regardless the characteristics of the framed area, the dispersion around the average value appears constant.

To deeply investigate the obtained results, a percent additive Gaussian noise Γ=5% (previously introduced in chapter 3) is added to the sampled images, in order to test if the presented behaviour is confirmed also in a noisier situation. Γ=5% is, in absolute, a high amount of noise considering the whole range of a digital camera but it ca be easily reached in digital image correlation measures in case of low contrasted pattern where the real exploited dynamic range is strongly reduced.

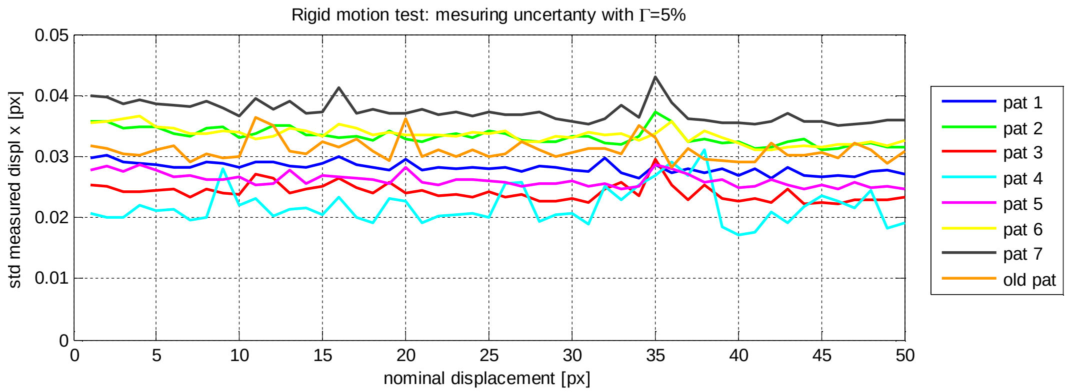

Fig. 6-10 Pattern optimization, rigid motion tests: standard deviation of every measured displacement matrix in case of Γ=5% noise

The same analysis previously presented has been performed on the noisy images; the data are presented in Fig. 6-10. An overall increment of the measurement uncertainty can be noticed. Furthermore, in this case, different values for the data standard deviations are associated to different patters. In order to summarize the results, the average measured uncertainty is computed for every pattern as the root mean squared of the collected data (i.e. averaging the variances of the date and computing the resulting mean standard deviation).
The results are presented in Fig. 6-11.

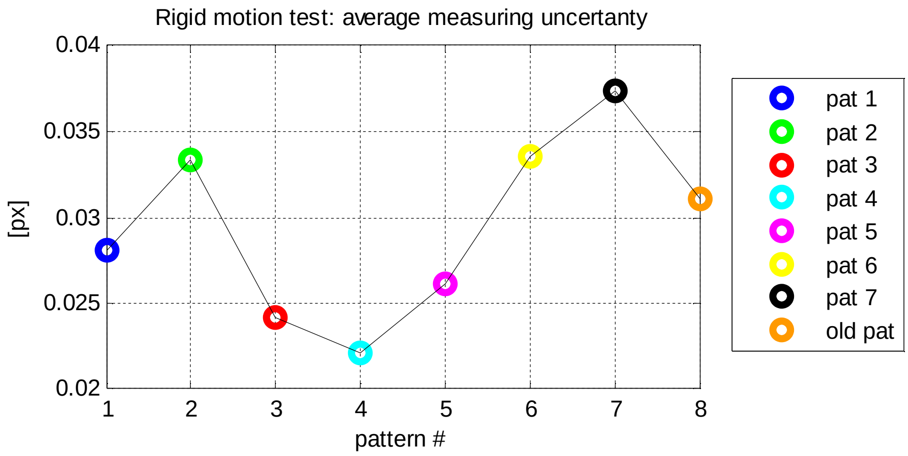

Fig. 6-11 Pattern optimization, rigid motion tests: average measurement uncertainty for every tested pattern

The pattern number 4, i.e. the one with associated the highest value of the mean intensity gradient from the theoretical analysis, is actually the pattern with associated the lowest measurement uncertainty, about 0.022 px. Furthermore, comparing the results in Fig. 6-11 with the respective MIG coefficients of Fig. 6-5 it can be noticed that not only the best pattern is confirmed, but the whole trend is respected. Globally, the data dispersion spans from 0.022 px of pattern 4 (the best one) to 0.037 px of pattern 7 (the worst tested one), i.e. a variation of about 70% in the measurement uncertainty simply related to different designs of the speckle pattern. Also considering the so called “old pattern”, a reduction in the data dispersion has been obtained after the design optimization.
The only discrepancy with respect to the theoretical model is the first point of the curve of Fig. 6-11 (pattern number 1, *D*=3 px, *step*=4.3 px). In this case, the performances of the design result better that expected looking at its MIG coefficient. This can be reasonably explained by looking to its position in the MIG graph: the pattern is in the highest gradient area of the curves and a slight variation of the scaling factor during the experimental tests could result in a sensible change in the pattern performances.

6.4 Optimized speckle pattern realized by toner transfer: an application

A small scale application of optimized speckle pattern realized by means of toner transfer to 3D DIC measurements is here reported.

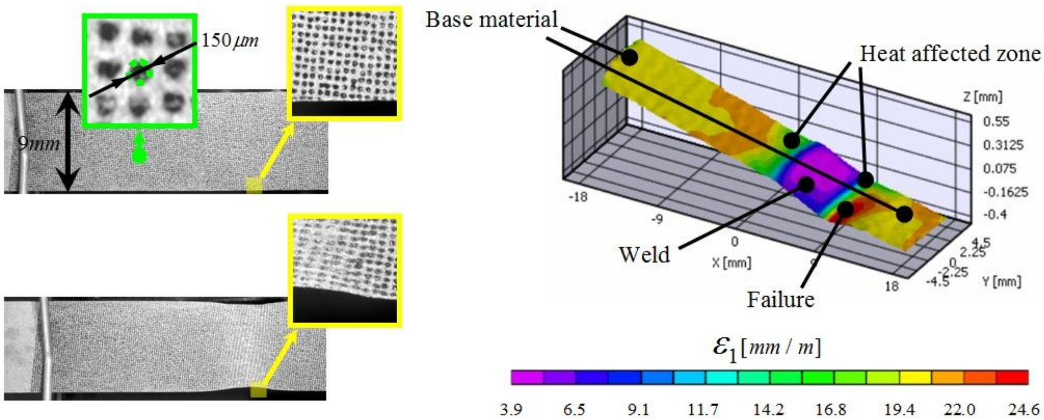

Fig. 6-12 Toner transfer: application to the study of elasto-plastic behaviour of Q&P martensite welded plates; acquired images (a) and analyzed data (b)

In Fig. 6-12a two acquired image, at the beginning and at the end of the tensile test of a Q&P (quenched and partitioned) martensite welded plate are shown. The specimen surface has been sandblasted: with this operation a sufficiently bright background has been obtained, avoiding the use of white enamel to increase the contrast of the pattern. The sample is about 9 mm wide, with a welded area of few millimetres to be inspected. In order to maximize the spatial resolution in the analysis, the smallest blob dimension achievable with the available hardware (about 150 µm) has been designed. It is possible to notice the high quality of the initial pattern in the first image and how it is able to correctly strain accordingly to the specimen with very low degradation, making possible to perform the measure until the end of the plastic test, when local strain exceed 100%. Digital image correlation analysis on the strained speckle pattern allowed the estimation of the elastic stiffness (Young's modulus and Poisson's ratio) of the welded area and the heat affected zones with respect to the base material and the study of the plastic behaviour of the alloy. Fig. 6-12b shows the principal measured strain during the test: the three different areas can be easily identified, together with the nucleation of the final failure, and the non perfect surface planarity arisen form the welding process can be recognized.

6.5 Concluding remarks

In the previous chapter, an innovative technique for speckle pattern realization for digital image correlation measurements has been proposed. The technique, “toner transfer”, was proven to be fast and cheap and, at the same time, capable to guarantee high quality and repeatability in the results. An important advantage of toner transfer is the possibility to numerically design the resulting speckle pattern on a computer.

In this chapter, the problem of the pattern design optimization is faced, in order to reduce the resulting measurement uncertainty and increase the stability of the results.

At first, a theoretical study is carried out: the design is optimized under detailed hypotheses, maximizing the mean intensity gradient of the resulting pattern varying speckle size and average distance. A pattern with speckle diameter of 4.5 px and average distance among blobs of 6 px resulted the one characterized by the highest value of the MIG coefficient.

In order to confirm the theoretical study, a rigid motion test has been performed: 7 patterns are selected among the ones tested in the MIG analysis, printed on a rigid surface and framed by a digital camera. By moving the camera on a plane parallel to the patterns one, it is possible to simulate rigid in-plane translation. In this way, a uniform motion field is imposed to the measurement surface and the dispersion of the data resulting by a DIC analysis is purely associated to measurement uncertainty.

No remarkable differences in the performances of the different patterns can be notice at this stage.

In order to investigate the robustness of the obtained results, Gaussian noise is added to the images acquired by the digital camera and the DIC analysis is repeated.

In this case, sensible differences in the dispersion of data related to different patterns can be appreciated: in particular, not only the 4.5 px diameter - 6 px step pattern is confirmed to be the one able to minimize the measurement uncertainty, in agreement with the theoretical study, but the whole trend confirms the simulations.

CHAPTER 7

On the field uncertainty estimation in 2D digital image correlation using fictitious strains

7.1 Introduction

As already discussed in the first chapter of this work, uncertainty estimation in digital image correlation measurements is a non-trivial and still partially unsolved issue. A theory has been developed in order to quantify the uncertainty in the computed displacement field ([113], already recalled in the introduction of chapter 3), but the derivation of the data variability associated to strains is not straightforward, due to the least squared fitting of the displacement field applied before the gradient computation (see paragraph 1.3.5).
In DIC applications, measurement uncertainty is related to a number of variables that can be grouped in four different categories:

- **Speckle pattern characteristic**, in terms of speckle size and distribution, contrast, gradient and gray intensity distribution; all these issue have been deeply investigated in the first part of this work.

- **Analysis parameters**, i.e. selected correlation criterion, implemented shape functions and intensity interpolation algorithm, subset size and overlap and strain kernel size; in other words, all the parameters that characterize the digital image correlation procedure described in paragraph 1.3.

- **Acquisition hardware**, that defines the resulting noise level in the acquired images, the measurement resolution, the optical distortions and, in case the acquisition rate is sufficiently higher than the analyzed phenomenon, the possibility to apply image averaging to noise reduction.

- **Environmental conditions**, such as temperature (hot waves problem, increase in the camera noise), lighting conditions, camera tripod vibration etc.

just to name the main influential parameters.
If, on one hand, the experimenter can not manage to fully control some of these variables (noise, temperature, vibrations …), on the other hand the selection and the tuning of others (as the analysis parameters) is not unique and strongly related to the given application. It is consequently difficult to develop a theory able to take in account such a large amount of variables and return a resulting data dispersion parameter. For this reason a different path has been followed, developing a new approach base on simple tests.
In this chapter, an innovative “on the filed” technique for strain uncertainty estimation in 2D digital image correlation will be presented and developed. The intention is to provide a method able to easily estimate the measurement uncertainty of a given setup (i.e. given textured specimen, hardware, environment and correlation algorithm) once the test has been prepared. The method will rely on the so called “fictitious strains” already introduced in chapter 2.

7.2 Uncertainty estimation using fictitious strains: ideal situation

As already deeply discussed in paragraph 2.2.1, in two dimensional digital image correlation applications the investigated problem is needed to be planar (in terms of both measurement surface and induced displacements / strains) in order to allow the algorithm to correctly compute the resulting displacement field. Out of plane movements are misinterpreted by the algorithm as in plane deformations. The idea proposed in this chapter is to exploit out of plane motion to easily generate controlled and known strain field and use them to evaluate the digital image correlation uncertainty.

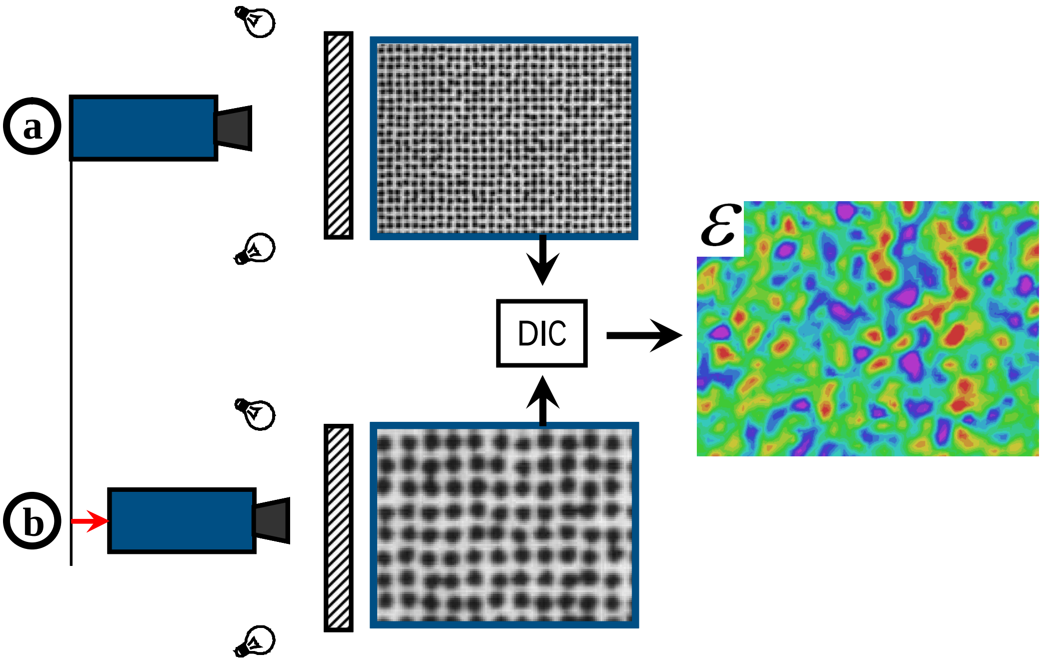

Fig. 7-1 Fictitious strains for uncertainty estimation: ideal situation

In Fig. 7-1a a traditional DIC measurement setup is sketched: a digital camera frames a flat textured surface. The sensor of the camera is parallel to the specimen and the resulting framed image is reported in the blue box. In order to estimate the measurement uncertainty of this given setup, an easy operation can be done: before running the actual test, the camera is moved, along its optical axis, towards the specimen and a new image is acquired (Fig. 7-1b). This corresponds to a simulated uniform two dimensional tension strain field. Running a digital image correlation analysis between the two images, the resulting strain map (either horizontal or vertical) will be characterize by a uniform strain level randomly perturbed by the data variability associated to the measurement uncertainty of the technique.

The uncertainty can consequently be easily computed as the standard deviation of the measured strain map. Compression strain fields can be simulated as well, turning away the camera from the specimen and the level of the fictitious deformation can be easily tuned, being it a linear function of the imposed displacement according to eq. 2.1 of paragraph 2.2.1.

This approach allows computing the measurement uncertainty on one hand taking in account basically all the uncertainty contributions described in the previous paragraph and, on the other hand, the actual realization of controlled strain fields (which is a non-trivial and a time consuming operation) is not required. Furthermore the technique does not require destroying the specimen to simulated high strain fields.

Unfortunately, the technique can not be easily implemented as presented due to the hypotheses implied by the method itself:

- the camera has to be initially perfectly parallel to the measurement surface
- the motion of the camera has to be perfectly parallel to the optical axis

A real time pose estimation algorithm, as the one presented in paragraph 2.2, could be exploited in order to meet the first requirement and assist the user during the camera movement but this would strongly complicate the practical application of the described procedure.
On the other hand, if the presented hypotheses are not fully satisfied, the resulting strain field will be characterized by non-linear strain trends along the whole map merged together with the data variability itself (Fig. 7-2) and the standard deviation of the computed deformation could no longer be considered an effective estimation of the measurement uncertainty.

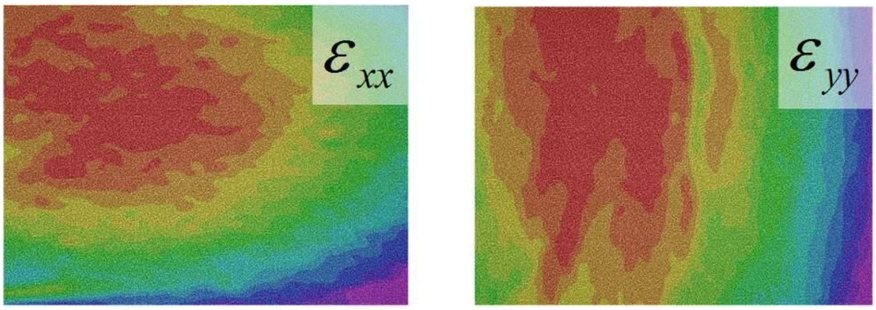

Fig. 7-2 Resulting fictitious strains in case of non ideal camera movement

In the following paragraph, a modified version of the presented procedure will be suggested in order to tackle the mentioned issues.

7.3 Uncertainty estimation using fictitious strains: real situation

The previously presented procedure can still be applied also in cases where the highlighted hypotheses can not be satisfied, providing that the theoretical fictitious strain fields are known. If this is true, it is consequently possible to compare theoretical and measured strain maps and evaluate an average measurement uncertainty as the root mean squared of the discrepancy map.
In order to be able and compute the theoretical fictitious strain fields, two hypotheses need to be fulfilled:

- the <u>initial</u> (3D) positions of the specimen surface with respect to the camera has to be known.

- the <u>final</u> (3D) positions of the specimen surface with respect to the camera has to be known.

In the following, it will be proven that these data, along with the results of a digital image correlation analysis between the two acquired images, are enough to estimate the fictitious strain fields. Two different methods will be introduced to accomplish the two tasks, in order to be able to propose a method as easy and fast as possible for the final user, and a procedure to extract the theoretical fictitious strain fields will be presented.

7.3.1 Estimation of the 3D initial position of the measurement surface with respect to the camera

Two-dimensional camera calibration is a standard procedure that needs to be carried out before a DIC analysis in order to:

- estimate the px to mm scaling factor in case the interest is focussed in the displacement fields (no calibration is needed for the strains computation: being the variable non-dimensional, µpx / px = µm / m)

- estimate the optical distortions introduced by the optics to compensate them for

The procedure consists in the acquisition of a flat regular grid, as the one of Fig. 7-3, placed on the measurement surface before the test is run.

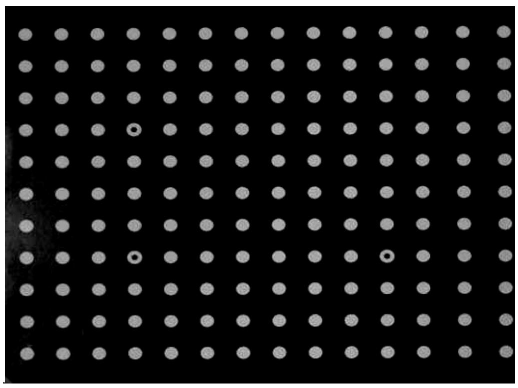

Fig. 7-3 Calibration grid of a 2D DIC analysis

The physical grid spacing is known and the coordinates of the centroid of every white circle is computed with a standard blob analysis image processing technique. It is consequently possible to estimate an average mm to px scaling factor and polynomial function that describes the variation of this scaling factor along the x and y axis of the image, i.e. evaluate the optical distortions.
The same data (blobs centroids coordinates) exploited for the camera calibration can be used in order to retrieve the initial position of the measurement surface with respect to the camera. The camera is framing an object of known geometries: exploiting the same pose estimation code presented in paragraph 2.2 the 3D position and orientation of the measurement surface with respect to the camera reference system can be readily obtained.

7.3.2 Estimation of the 3D initial position of the subset centroids

As already recalled in paragraph 1.3.4, in the first step of a digital image correlation algorithm an ordinate grid is of subsets is generated on the reference image (see Fig. 1-5): these points are the ones whose displacement will be tracked.

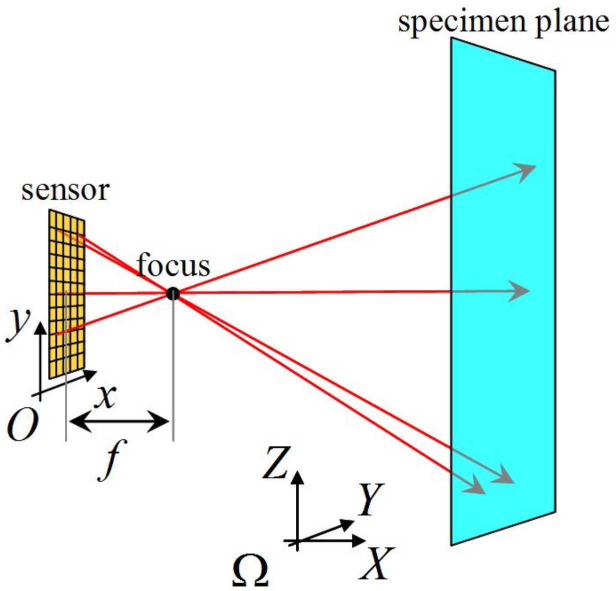

Fig. 7-4 Subsets centroids back-projection

Starting from the coordinates of the centre of every subset, it is straightforward to compute their physical position on the sensor of the camera knowing the physical dimension of every pixel (either from the manufacturer or thanks to a Zang calibration of the camera [90]). It is consequently possible to back-project

them in the real world intersecting the lines passing trough the points on the sensor and the focus of the optics with the plane representing the position of the measurement surface identified in the previous paragraph (Fig. 7-4).
With this operation, the initial position of the points, tracked by the DIC algorithm, in a camera based 3D reference system is known.

7.3.3 Estimation of the 3D final position of the subset centroids

An approach similar to the one proposed for the computation of the 3D position of the subsets of the first image could be exploited for the second one, but this would required an additional calibration image to be acquired, slowing down the procedure.
In order to avoid this, a different approach will be followed for the evaluation of the 3D final position of the subsets centroids.
Providing that:

- the initial position of the subset centroids is known in a 3D camera-based reference system (as explained in the last two paragraph)

- the horizontal and vertical displacement maps of the subsets centres are known in the 2D reference system of the camera sensor (from a 2D DIC analysis)

it will be demonstrated that is possible to estimate the theoretically imposed fictitious displacement field, considering that:

1) even in case when the motion imposed to the camera does not act perfectly along the optical axis, the resulting fictitious displacement field can not be totally arbitrary but it is always a consequence of a plane surface that that does not undergoes to shape and size changes, rigidly moved in a 3D volume and re-projected on a 2D sensor (the motion is actually imposed to the camera but, being the position estimation relative, there is no difference at all)

and

2) at the same time, the in plane displacements computed by the DIC code can be considered globally bias-less: if, on one hand, the single subset correlation is subjected to the characteristic subpixel bias describe in chapters 3, on the other hand different subsets sample the deterministic zero-mean bias curve of Fig. 3-5 in different points and consequently the deterministic subpixel effect becomes a globally random contribution in

case the displacement field is not constant. Furthermore, the image blurring presented in chapter 3 was proven to be able to delete the bias effect.

Thus, for a given set of the 3 translation (x,y and z) and 3 rotations (roll, yaw and pitch) of the object in the space, it is possible to rigidly move the original subsets in a 3D reference system and, after that, reproject them on the sensor of the camera. The motion of a rigid object in a 3D space is a well studied problem, usually implemented using homogeneous coordinates [91], while the reprojection can be easily simulated using an ideal pinhole camera model [3, 91] once the camera is calibrated (i.e. the optical distortion are considered and compensated for).
The mean squared discrepancy, between the subsets 2D coordinates resulted by rototranslation and reprojection and the subsets 2D coordinates estimated by the digital image correlation analysis performed from the first acquired image to the second one, can be readily computed. This parameter can be considered an index of the agreement between the 3D motion of the measurement surface with respect to the camera simulated with the rototranslation and the actual relative motion imposed physically moving the camera.
A non linear optimization algorithm can consequently be exploited in order to iteratively rototranslate the initial set of subsets coordinates in order to minimize the mean squared reprojection error, following an approach very similar to the one presented in paragraph 2.2.7 for the self developed pose estimation code.

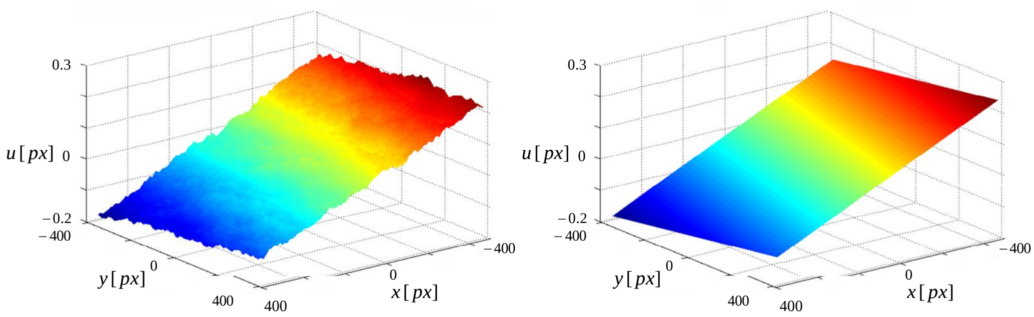

(a) **(b)**

Fig. 7-5 Horizontal displacement map u resulting by an out of plane motion of the measurement surface: estimated by a DIC algorithm (a) and resulting by rigid rototranslation and reprojection of a given set of subsets (b)

In this way two displacement fields are available:

- the first is the one computed by the DIC algorithm

- the second is the one associated to the rototranslation and reprojection of the original set of coordinates able the minimize the root mean squared reprojection error

where the second one is computed under the hypothesis that the fictitious motion field is a consequence of a rigid plane surface that rototranslate in the space. An example of the results obtained by this approach is reported in Fig. 7-5, where it is possible to notice the shape agreement between computed and fitted surfaces, with the absence of noise induced data variability in the latter.
Once the vertical and horizontal fitted motion fields are known, it is possible to numerically differentiate them in order to compute the theoretically imposed fictitious strain fields and compare them with the ones computed by the digital image correlation algorithm in order to evaluate the strain measurement uncertainty of the given setup.

7.3.4 Uncertainty estimation using fictitious strains: results

A series of image of a speckle pattern macroscopically translating along the optical axis of a camera has been acquired and the proposed method has been applied in order to estimate the strain uncertainty of the given DIC setup.
In order to apply fictitious strains, the speckle pattern is mounted on a slide (Fig. 7-6a), one initial calibration image is acquired (Fig. 7-6b) and several image of the pattern at different distance from the camera are collected (Fig. 7-6c).
The camera is initially at about 2 m from the target and displacements from few micrometers to some centimetres are imposed to the pattern.

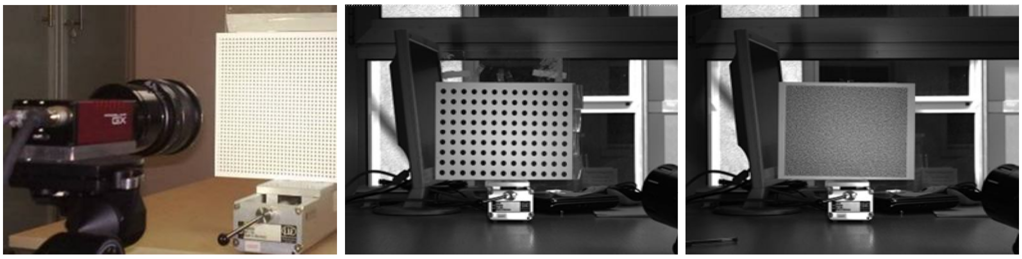

(a) **(b)** **(c)**

Fig. 7-6 Uncertainty estimation by means of fictitious strains: setup (a), acquired calibrating image (b) and acquired speckle pattern (c)

The procedure presented in the previous paragraphs is applied to every acquired image and the horizontal and vertical strains fields, both evaluated by the DIC code and estimated using the rigid plane motion fitting, are computed. Successively, the discrepancy strain maps, i.e. the point by point differences of the theoretic and measured strain fields are evaluated (Fig. 7-7).

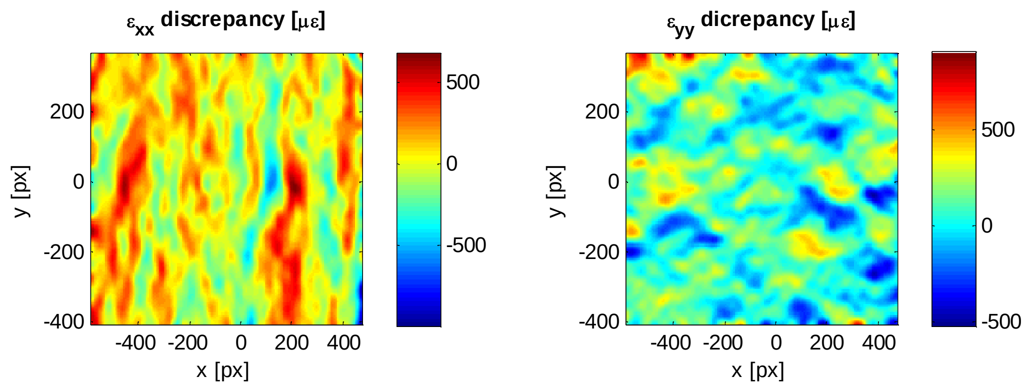

Fig. 7-7 Point by point discrepancy between theoretical and estimated strain maps

As can be noticed by the results of Fig. 7-7, the discrepancy maps are globally trendless: the developed model is actually able to globally fit the fictitious strain field and the resulting variability is only due to DIC measurement uncertainty.
The average strain maps discrepancy for every acquired image is graphed in Fig. 7-8 along with the root mean squared strain discrepancy.

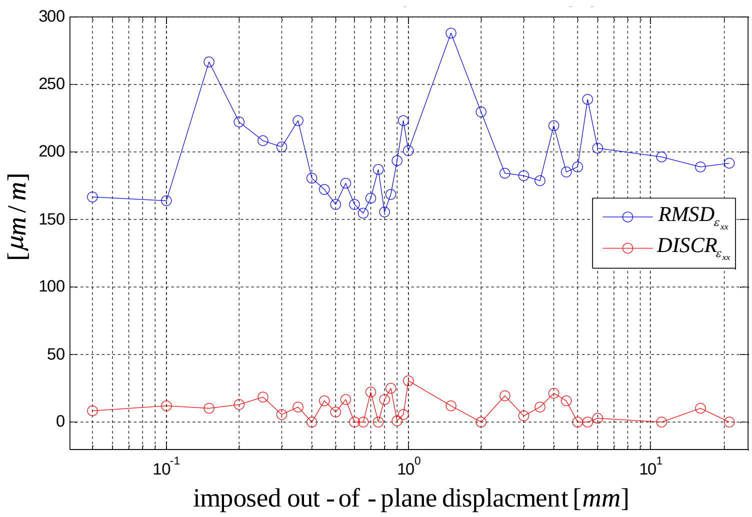

Fig. 7-8 Uncertainty estimation using fictitious strains: results

It can be noticed that the average discrepancy values DISCR$_{\varepsilon xx}$ are about 1 order of magnitude smaller than RMS ones: this means the accuracy of the fitting procedure that allows to estimate the target motion is a lot higher than the inherent data variability due to the DIC algorithm and the residual mismatching can be considered negligible.
The blue curve of in Fig. 7-8 can be consequently trusted as an effective estimation of the strain measurement uncertainty; being the imposed motion macroscopically acting along with the optical axis, the simulated strain fields are

characterized by low gradients (only due to the non-ideal motion) and consequently the computed root mean squared discrepancy value can be considered an effected estimation of the measurement uncertainty in case of uniform strain field, about 200 µm/m in the tested setup.

7.3.5 Uncertainty estimation using fictitious strains: fast approach

The procedure, as presented in the previous paragraphs, implies at first the acquisition of a calibration grid and then the camera movement. However, in this way the camera is moved after the calibration is performed and consequently a new calibration image is needed to be acquired before the test is run as a reference for the DIC analysis.
For this reason, it is suggested to apply the proposed procedure in reverse: place at first the camera farther (or closer) to the measurement surface with respect to the ideal position, acquire several images moving the camera toward the final position and at the end acquire the calibration grid.
Simply analyzing the last acquired image as first it is possible to directly apply the proposed method without performing the calibration twice.

7.4 Concluding remarks

Strain uncertainty estimation in digital image correlation measurements is a non-trivial issue, due to its strong relation the characteristics of the given measurement setup. In this chapter, an innovative procedure for “on the field” uncertainty evaluation in case of 2D measurements has been presented.
The procedure requires to the final user only simply out of plane camera movements and image acquisition that can be performed by the experimenter before the actual test is done.
On one hand, camera movements imply the simulation of fictitious strain fields on the given specimen in the given hardware measurement condition and, on the other hand, the theoretical induced strain maps can be retrieved starting from the DIC analysis itself.
The comparison between theoretical and measured strain maps has been proven to be an effective approach to quantify the measurement uncertainty including all the major influence parameters.

CHAPTER 8

Conclusions

Digital Image Correlation is increasingly widespread vision based measurement technique for full field motion and strain estimation.
Firstly proposed in the early ‘80s, it has undergone a great development in the last decade, pushed by the synergic improve of vision hardware and computing power performances, both in terms of analysis algorithms and fields of application. Nowadays DIC-based testing activities spans from micro-electro-mechanical-systems to full-scale civil structures testing, in a variety of temperature ranges (that can easily overcome the melting limit of many metal alloys), materials (from nano-reinforced mortars through composite multilayer material to organic tissues) and dynamic capabilities (static to blasting tests).
Out of the main critical issues still associated to digital image correlation applications highlighted in the most recent scientific literature, this worked has tried to face the problems linked to the probably most important metrological parameter for a measurement system: the associated uncertainty, i.e. a synthetic index of the attended dispersion of the probability function describing the measured quantity.
On one hand, the full field measurement capabilities of the most modern DIC systems has to face a resulting measurement uncertainty that can not yet compete with the ones of traditional pointwise state of the art approaches (e.g.

strain gauges based measurements), and this is generally a problem in case brittle material testing and elastic strain evaluation, where the resulting signal to noise ratio may not be sufficient. On the other hand, the quantification of the uncertainty associated to DIC strain measurements is by itself a non-trivial aspect: no theories exist able to quantify the main uncertainty contribution and return an estimation of resulting strain data dispersion.
The first aspect, i.e. the necessary reduction of the measurement uncertainty, has been faced in this work from two independent points of view.
In the first part, image blurring has been proposed, studied, tuned and successively validated as an effective procedure to reduce the measurement uncertainty: high spatial frequency components in the acquired images are proven to be misinterpreted by state of the art DIC analysis algorithm and consequently low pass filtering has been implemented and studied as a method to remove these components and improve the codes performances. The theoretical study of the problem has been carried out on synthetic (i.e. numerically generated) images, where the effects of image blurring on the resulting measurement uncertainty has been tested on more and more complex simulated displacement and strain fields. The stability of the obtained results has consequently been proven at first adding noise to the acquired data, varying the main DIC analysis parameters and the characteristic of the numerically built speckle patterns (i.e. the characteristic textured surfaces required for DIC analyses). Successively, experimental tests have been carried out in order to verify the validity of the implemented simulation strategy and confirm the obtained results. A Gaussian low pass filtering of standard deviation equal to 0.75 px has been doubtless identified as an effectively image preprocessing operation able to minimize the resulting measurement uncertainty.
In the second part of the work the speckle pattern creation and optimization has been faced. An innovative technique, “toner transfer”, has been proposed for the proper texturization of the measurement surface. Toner transfer has been proven to be cheap, fast and repetitive technology, able to generate, with respect to the traditionally exploited techniques, higher quality textures (i.e. speckle patterns able to increase the resulting measurement resolution and decrease the associated uncertainty). Furthermore, its flexibility in terms of material, geometry and size of the measurement surface and its suitability in case of high temperature tests has been presented and verified. With toner transfer, the resulting speckle pattern is numerically generated thus allowing the optimization of its design in terms of reduction of the resulting measurement uncertainty. A “quality parameter” of the resulting pattern, largely accepted in the scientific literature, has been numerically maximized varying the main characteristics of the speckle pattern design. The capability of the optimized speckle pattern to reduce the resulting measurement uncertainty, in particular in case of high noise

level or low intensity gradients in the acquired images, has been experimentally validated.
The last part of the work dealt with the second of the previously named problems associated to uncertainty in digital image correlation: its quantification in relation to strain measurements. An innovative fast procedure to estimate "on the field" this metrological parameter in case of 2D analyses, taking into account all the major uncertainty sources, is proposed. The technique relies on the generation of known controlled fictitious strain field by means of out of plane camera-specimen motion. The theoretically imposed fictitious strain fields are retrieved using two different version of a pose estimation algorithm (previously developed for simple camera placement) and compared with the ones measured by the DIC code in order to quantify the expected data variability for the given measurement setup.

References

1. B Pan, K Qian, H Xie, A Asundi. Two-dimensional digital image correlation for in-plane displacement and strain measurement: A review, Measurement Science and Technology. 20 (2009).
2. PK Rastogi. Photomechanics, Topics in Applied Physics. (2000)
3. MA Sutton, JJ Orteu, HW Schreier, Image Correlation for Shape, Motion and Deformation Measurements; Basic Concepts, Theory and Applications, Springer (2009).
4. WH Peters, WF Ranson. Digital imaging techniques in experimental stress analysis. Optical Engineering. 21 (1982) 427-431.
5. TC Chu, WF Ranson, MA Sutton. Applications of digital-image-correlation techniques to experimental mechanics, Exp.Mech. 25 (1985) 232-244.
6. M Sutton, C Mingqi, W Peters, Y Chao, S McNeill. Application of an optimized digital correlation method to planar deformation analysis, Image Vision Comput. 4 (1986) 143-150.
7. WH Peters, WF Ranson, MA Sutton, TC Chu, J Anderson. Application of digital correlation methods to rigid body mechanics. Optical Engineering. 22 (1983) 738-742.
8. MA Sutton, SR McNeill, JD Helm, YJ Chao. Advances in two-dimensional and three-dimensional computer vision, Photomechanics. 77 (2000) 323-372.
9. HW Schreier. Investigation of two and three dimensional image correlation techniques with application in experimental mechanics. PhD Thesis. (2003).
10. D Zhang, X Zhang, G Cheng. Compression strain measurement by digital speckle correlation, Exp.Mech. 39 (1999) 62-65.
11. P Zhou, KE Goodson. Subpixel displacement and deformation gradient measurement using digital image/speckle correlation (DISC), Optical Engineering. 40 (2001) 1613-1620.
12. BK Bay. Texture correlation: A method for the measurement of detailed strain distributions within trabecular bone, Journal of Orthopaedic Research. 13 (1995) 258-267.
13. DJ Chen, FP Chiang, YS Tan, HS Don. Digital speckle-displacement measurement using a complex spectrum method, Appl.Opt. 32 (1993) 1839-1849.

14. GR Gaudette, J Todaro, IB Krukenkamp, F- Chiang. Computer aided speckle interferometry: A technique for measuring deformation of the surface of the heart, Ann.Biomed.Eng. 29 (2001) 775-780.
15. M Sjödahl, LR Benckert. Electronic speckle photography: Analysis of an algorithm giving the displacement with subpixel accuracy, Appl.Opt. 32 (1993) 2278-2284.
16. M Sjodahl, LR Benckert. Systematic and random errors in electronic speckle photography, Appl.Opt. 33 (1994) 7461-7471.
17. M Sjodahl. Electronic speckle photography: increased accuracy by nonintegral pixel shifting, Appl.Opt. 33 (1994) 6667-6673.
18. M Sjödahl. Accuracy in electronic speckle photography, Appl.Opt. 36 (1997) 2875-2885.
19. MA Iadicola, RS Zobel, JM Ocel, Quantitative evaluation of digital image correlation as applied to large-scale gusset plate experiments, Bridge Maintenance, Safety, Management, Resilience and Sustainability - Proceedings of the Sixth International Conference on Bridge Maintenance, Safety and Management. (2012) 1436-1443.
20. B LeBlanc, C Niezrecki, P Avitabile, J Chen, J Sherwood, S Hughes, Full-field inspection of a wind turbine blade using three-dimensional digital image correlation, Proceedings of SPIE - The International Society for Optical Engineering. 7979 (2011).
21. S Ri, T Numayama, M Saka, K Nanbara, D Kobayashi. Noncontact deflection distribution measurement for large-scale structures by advanced image processing technique, Materials Transactions. 53 (2012) 323-329.
22. Z Sun, JS Lyons, SR McNeill. Measuring Microscopic Deformations with Digital Image Correlation, Optics and Lasers in Engineering. 27 (1997) 409-428.
23. MC Pitter, CW See, JYL Goh, MG Somekh. Focus errors and their correction in microscopic deformation analysis using correlation, Optics Express. 10 (2002) 1361-1367.
24. D Zhang, M Luo, DD Arola. Displacement/strain measurements using an optical microscope and digital image correlation, Optical Engineering. 45 (2006).
25. TA Berfield, JK Patel, RG Shimmin, PV Braun, J Lambros, NR Sottos. Fluorescent image correlation for nanoscale deformation measurements, Small. 2 (2006) 631-635.
26. C Franck, S Hong, SA Maskarinec, DA Tirrell, G Ravichandran. Three-dimensional full-field measurements of large deformations in soft materials using confocal microscopy and digital volume correlation, Exp.Mech. 47 (2007) 427-438.

27. N Sabaté, D Vogel, A Gollhardt, J Keller, C Cané, I Gràcia, et al. Residual stress measurement on a MEMS structure with high-spatial resolution, J Microelectromech Syst. 16 (2007) 365-372.
28. J Kang, M Jain, DS Wilkinson, JD Embury. Microscopic strain mapping using scanning electron microscopy topography image correlation at large strain, J.Strain Anal.Eng.Des. 40 (2005) 559-570.
29. MA Sutton, N Li, DC Joy, AP Reynolds, X Li. Scanning electron microscopy for quantitative small and large deformation measurements Part I: SEM imaging at magnifications from 200 to 10,000, Exp.Mech. 47 (2007) 775-787.
30. MA Sutton, N Li, D Garcia, N Cornille, JJ Orteu, SR McNeill, et al. Scanning electron microscopy for quantitative small and large deformation measurements Part II: Experimental validation for magnifications from 200 to 10,000, Exp.Mech. 47 (2007) 789-804.
31. S Cho, JF Cárdenas-García, I Chasiotis. Measurement of nanodisplacements and elastic properties of MEMS via the microscopic hole method, Sens Actuators A Phys. 120 (2005) 163-171.
32. S Chang, CS Wang, CY Xiong, J Fang. Nanoscale in-plane displacement evaluation by AFM scanning and digital image correlation processing, Nanotechnology. 16 (2005) 344-349.
33. Y Sun, JHL Pang, W Fan. Nanoscale deformation measurement of microscale interconnection assemblies by a digital image correlation technique, Nanotechnology. 18 (2007).
34. G Vendroux, WG Knauss. Submicron deformation field measurements: Part 1. Developing a digital scanning tunneling microscope, Exp.Mech. 38 (1998) 18-23.
35. G Vend Roux, WG Knauss. Submicron deformation field measurements: Part 2. Improved digital image correlation, Exp.Mech. 38 (1998) 86-92.
36. G Vendroux, N Schmidt, WG Knauss. Submicron deformation field measurements: Part 3. Demonstration of deformation determinations, Exp.Mech. 38 (1998) 154-160.
37. F Barthelat, Z Wu, BC Prorok, HD Espinosa. Dynamic torsion testing of nanocrystalline coatings using high-speed photography and digital image correlation, Exp.Mech. 43 (2003) 331-340.
38. F Yang, X He, C Quan. Characterization of dynamic microgyroscopes by use of temporal digital image correlation, Appl.Opt. 45 (2006) 7785-7790.
39. T Sibert, T Becker, K Spiltthof, I Neumann, R Krupka. High-speed digital image correlation: Error estimations and applications, Optical Engineering. 46 (2007).

40. V Tiwari, MA Sutton, SR McNeill. Assessment of high speed imaging systems for 2D and 3D deformation measurements: Methodology development and validation, Exp.Mech. 47 (2007) 561-579.
41. F Grytten, H Daiyan, M Polanco-Loria, S Dumoulin. Use of digital image correlation to measure large-strain tensile properties of ductile thermoplastics, Polym.Test. 28 (2009) 653-660.
42. Y Han, AD Rogalsky, B Zhao, HJ Kwon. The application of digital image techniques to determine the large stress-strain behaviors of soft materials, Polym.Eng.Sci. 52 (2012) 826-834.
43. S Mzabi, D Berghezan, S Roux, F Hild, C Creton. A critical local energy release rate criterion for fatigue fracture of elastomers, J.Polym.Sci.Part B. 49 (2011) 1518-1524.
44. L Chevalier, S Calloch, F Hild, Y Marco. Digital image correlation used to analyze the multiaxial behavior of rubber-like materials, European Journal of Mechanics, A/Solids. 20 (2001) 169-187.
45. P Leplay, J Réthoré, S Meille, M- Baietto. Identification of asymmetric constitutive laws at high temperature based on Digital Image Correlation, Journal of the European Ceramic Society. 32 (2012) 3949-3958.
46. MD Novak, FW Zok. High-temperature materials testing with full-field strain measurement: Experimental design and practice, Rev.Sci.Instrum. 82 (2011).
47. B Pan, D Wu, L Yu. Optimization of a three-dimensional digital image correlation system for deformation measurements in extreme environments, Appl.Opt. 51 (2012) 4409-4419.
48. M Touboul, J Crepin, G Rousselier, F Latourte, S Leclercq. Identification of Local Viscoplastic Properties in P91 Welds from Full Field Measurements at Room Temperature and 625 °C, Exp.Mech. (2012) 1-14.
49. A Giachetti. Matching techniques to compute image motion, Image Vision Comput. 18 (2000) 247-260.
50. W Tong, H Tao, N Zhang, LG Hector Jr. Time-resolved strain mapping measurements of individual Portevin-Le Chatelier deformation bands, Scr.Mater. 53 (2005) 87-92.
51. B Pan, H Xie, Z Guo, T Hua. Full-field strain measurement using a two-dimensional Savitzky-Golay digital differentiator in digital image correlation, Optical Engineering. 46 (2007).
52. HW Schreier, MA Sutton. Systematic errors in digital image correlation due to undermatched subset shape functions, Exp.Mech. 42 (2002) 303-310.

53. H Lu, PD Cary. Deformation measurements by digital image correlation: Implementation of a second-order displacement gradient, Exp.Mech. 40 (2000) 393-400.
54. WG Knauss, I Chasiotis, Y Huang. Mechanical measurements at the micron and nanometer scales, Mech.Mater. 35 (2003) 217-231.
55. HW Schreier, JR Braasch, MA Sutton. Systematic errors in digital image correlation caused by intensity interpolation, Optical Engineering. 39 (2000) 2915-2921.
56. Z- Zhang, Y- Kang, H- Wang, Q- Qin, Y Qiu, X- Li. A novel coarse-fine search scheme for digital image correlation method, Meas J Int Meas Confed. 39 (2006) 710-718.
57. F Hild, B Raka, M Baudequin, S Roux, F Cantelaube. Multiscale displacement field measurements of compressed mineral-wool samples by digital image correlation, Appl.Opt. 41 (2002) 6815-6828.
58. B Pan, H Xie, Y Xia, Q Wang. Large-deformation measurement based on reliable initial guess in digital image correlation method, Guangxue Xuebao/Acta Optica Sinica. 29 (2009) 400-406.
59. B Pan, H- Xie. Digital image correlation method with differential evolution, Guangdianzi Jiguang/Journal of Optoelectronics Laser. 18 (2007) 100-103.
60. P- Hung, AS Voloshin. In-plane strain measurement by digital image correlation, Journal of the Brazilian Society of Mechanical Sciences and Engineering. 25 (2003) 215-221.
61. HA Bruck, SR McNeill, MA Sutton, WH Peters III. Digital image correlation using Newton-Raphson method of partial differential correction, Exp.Mech. 29 (1989) 261-267.
62. B Pan. Reliability-guided digital image correlation for image deformation measurement, Appl.Opt. 48 (2009) 1535-1542.
63. J Luo, K Ying, P He, J Bai. Properties of Savitzky-Golay digital differentiators, Digital Signal Process Rev.J. 15 (2005) 122-136.
64. J Luo, J Bai, P He, K Ying. Axial strain calculation using a low-pass digital differentiator in ultrasound elastography, IEEE Trans.Ultrason.Ferroelectr.Freq.Control. 51 (2004) 1119-1127.
65. MA Sutton, JL Turner, HA Bruck, TA Chae. Full-field representation of discretely sampled surface deformation for displacement and strain analysis, Exp.Mech. 31 (1991) 168-177.
66. LB Meng, GC Jin, XF Yao. Application of iteration and finite element smoothing technique for displacement and strain measurement of digital speckle correlation, Optics and Lasers in Engineering. 45 (2007) 57-63.
67. CC- Wang, J- Deng, GA Ateshian, CT Hung. An automated approach for direct measurement of two-dimensional strain distributions within

articular cartilage under unconfined compression, J.h.Eng. 124 (2002) 557-567.

68. B Wattrisse, A Chrysochoos, J- Muracciole, M Némoz-Gaillard. Analysis of strain localization during tensile tests by digital image correlation, Exp.Mech. 41 (2001) 29-39.
69. W Tong, H Tao, N Zhang, LG Hector Jr. Time-resolved strain mapping measurements of individual Portevin-Le Chatelier deformation bands, Scr.Mater. 53 (2005) 87-92.
70. O.Faugeras, F.Devernay. Computing Differential Properties of 3D shapes from Stereoscopic Images without 3D Models.Technical Report 2304, INRIA (France), 1994.
71. H Lu, X Zhang, WG Knauss. Uniaxial, shear, and poisson relaxation and their conversion to bulk relaxation: Studies on poly(methy methacrylate), Polym.Eng.Sci. 37 (1997) 1053-1064.
72. BA Wasil, DC Merchant. Plate-deflection measurement by photogrammetric methods - Photogrammetric techniques which have successfully been used to obtain accurate topographic maps from aerial photographs are applied to the task of measuring deflections in a laterally loaded plate, Exp.Mech. 4 (1964) 77-83.
73. F Ackermann. Digital image correlation: performance and potential application in photogrammetry. Photogramm.Rec. 11 (1984) 429-439.
74. F Boochs. Off-line compilation of photogrammetric stereo models using digital image correlation, Photogrammetria. 41 (1987) 183-199.
75. UV Helava. Digital correlation in photogrammetric instruments, Photogrammetria. 34 (1978) 19-41.
76. ZL Kahn-Jetter, TC Chu. Three-dimensional displacement measurements using digital image correlation and photogrammic analysis, Exp.Mech. 30 (1990) 10-16.
77. Y Morimoto, M Fujigaki. Automated analysis of 3-D shape and surface strain distributions of a moving object using stereo vision, Optics and Lasers in Engineering. 18 (1993) 195-212.
78. P.F.Luo, Y.J.Chao, M.A.Sutton. Application of stereo vision to three-dimensional deformation analyses in fracture experiments. Optical Engineering, 33(3) :981–990,1994.
79. P.F.Luo, Y.J.Chao, M.A.Sutton, W.H.Peters. Accurate measurement of three-dimensional deformations in deformable and rigid bodies using computer vvision. Experimental Mechanics,33(2):123–132,June1993.
80. J. D. Pack, F. Noo, R. Clackdoyle. Cone beam reconstruction using the back projection of locally filtered projections. Medical Imaging, 24(1):70–85, 2005.
81. M.Devy, V.Garric, J.-J.Orteu. Camera calibration from multiple views of a 2D object using a global non linear minimization method.In

International Conference on Intelligent Robots and Systems (IROS'97), Grenoble, France, September 1997.
82. J. M. Lavest, M. Viala, M. Dhome. Do we really need an accurate calibration pattern to achieve a reliable camera calibration? In Proceedings of European Conference on Computer Vision, pages 158–174, Frieburg, Germany, 1998.
83. D. Garcia, J.-J.Orteu, M.Devy. Accurate calibration of a stereo vision sensor: comparison of different approaches. In Proceedings of 5th Workshop on Vision, Modeling, and Visualization (VMV'2000), pages 25–32, Saarbrücken, Germany, November 2000.
84. H Haddadi, S Belhabib. Use of rigid-body motion for the investigation and estimation of the measurement errors related to digital image correlation technique, Optics and Lasers in Engineering. 46 (2008) 185-196.
85. MA Sutton, JH Yan, V Tiwari, HW Schreier, JJ Orteu. The effect of out-of-plane motion on 2D and 3D digital image correlation measurements, Optics and Lasers in Engineering. 46 (2008) 746-757.
86. I De Baere, W Van Paepegem, N Lammens, P Lava, D Debruyne, C Cofaru, et al., Experimentally induced errors in Digital Image Correlation measurement of small strains with large gradients, Emerging Technologies in Non-Destructive Testing V - Proceedings of the 5th Conference on Emerging Technologies in NDT. (2012) 441-446.
87. NA Hoult, W Andy Take, C Lee, M Dutton. Experimental accuracy of two dimensional strain measurements using Digital Image Correlation, Eng.Struct. 46 (2013) 718-726.
88. YG Wang, W Tong. A high resolution DIC technique for measuring small thermal expansion of film specimens, Optics and Lasers in Engineering. 51 (2013) 30-33.
89. G.-L. Shan, B. Ji, Y.-F. Zhou, A review of 3D pose estimation from a monocular image sequence, 2nd International Congress on Image and Signal Processing, Tianjin, 2009.
90. Z. Zhang, A flexible new technique for camera calibration, IEEE Transactions on Pattern Analysis and Machine Intelligence, 22(11):1330-1334, 2000.
91. Y. Ma, S. Soatto, J. Kosecka, S. Sastry, An Invitation to 3D Vision, Springer, Heidelberg, 2001.
92. C.-P. Lu, G.D. Hager, E. Mjolsness, Fast and globally convergent pose estimation from video images; IEEE Transactions on Pattern Analysis and Machine Intelligence, Vol 22 Issue 6, pp 610 – 622 (2000).
93. G. Pisinger, G. Maier, Re-projective Pose Estimation of a Planar Prototype, Proc. 4th Int. Conf. on Computer Vision/Computer Graphics, Belgium 2009.

94. G. Schweighofer, A. Pinz, Robust pose estimation from a planar target, IEEE Transactions on Pattern Analysis and Machine Intelligence, Vol 28 Issue 12, 2006.
95. J. Nocedal, S.J. Wright, Numerical Optimization, Springer, Berlin, Heidelberg, New York, 2006.
96. IS0 12233: Photography - Electronic still picture camera - resolution measurement, 2000
97. J. M. Tenenbaum, Accommodation in Computer Vision, Ph.D. dissertation, Dept. of Comput. Sci., Stanford Univ., Stanford, CA, 1970.
98. S. K. Nayar and Y. Nakagawa, Shape from focus, IEEE Trans. Pattern Anal. Mach. Intell., vol. 16, no. 8, pp. 824–831, Aug. 1994.
99. M. Subbarao and J. K. Tyan, "The optimal focus measure for passive autofocusing and depth-from-focus," in Proc. SPIE. Videometrics IV, Oct. 1995, pp. 89–99.
100. K. S. Choi, J. S. Lee, and S. J. Ko, "New autofocus technique using the frequency selective weighted median filter for video cameras," IEEE Trans. Consumer Electron., vol. 45, no. 3, pp. 820–827, Aug. 1999.
101. G. Yang and B. J. Nelson, "Wavelet-based autofocusing and unsupervised segmentation of microscopic images," in Proc. IEEE/RSJ Int.Conf. Intelli. Robots Syst., Oct. 2003, pp. 2143–2148.
102. S- Lee, Y Kumar, J- Cho, S- Lee, S- Kim. Enhanced autofocus algorithm using robust focus measure and fuzzy reasoning, IEEE Transactions on Circuits and Systems for Video Technology. 18 (2008) 1237-1246.
103. B Pan, Z Lu, H Xie. Mean intensity gradient: An effective global parameter for quality assessment of the speckle patterns used in digital image correlation, Optics and Lasers in Engineering. 48 (2010) 469-477.
104. D Lecompte, A Smits, S Bossuyt, H Sol, J Vantomme, D Van Hemelrijck, et al. Quality assessment of speckle patterns for digital image correlation, Optics and Lasers in Engineering. 44 (2006) 1132-1145.
105. J Chen, G Jin, L Meng. Applications of Digital Correlation Method to Structure Inspection, Tsinghua Science and Technology. 12 (2007) 237-243.
106. P Zhou, KE Goodson. Subpixel displacement and deformation gradient measurement using digital image/speckle correlation (DISC), Optical Engineering. 40 (2001) 1613-1620.
107. D Lecompte, H Sol, J Vantomme, A Habraken, Analysis of speckle patterns for deformation measurements by digital image correlation, Proceedings of SPIE - The International Society for Optical Engineering. 6341 (2006).

108. B Pan, K Qian, H Xie, A Asundi, On errors of digital image correlation due to speckle patterns, Proceedings of SPIE - The International Society for Optical Engineering. 7375 (2009).

109. M Bornert, F Brémand, P Doumalin, J- Dupré, M Fazzini, M Grédiac, et al. Assessment of digital image correlation measurement errors: Methodology and results, Exp.Mech. 49 (2009) 353-370.

110. S Yaofeng, JHL Pang. Study of optimal subset size in digital image correlation of speckle pattern images, Optics and Lasers in Engineering. 45 (2007) 967-974.

111. B Pan, H Xie, Z Wang, K Qian, Z Wang. Study on subset size selection in digital image correlation for speckle patterns, Optics Express. 16 (2008) 7037-7048.

112. C Niezrecki, P Avitabile, C Warren, P Pingle, M Helfrick, A review of digital image correlation applied to structural dynamics, AIP Conference Proceedings. 1253 (2010) 219-232.

113. YQ Wang, MA Sutton, HA Bruck, HW Schreier. Quantitative error assessment in pattern matching: Effects of intensity pattern noise, interpolation, strain and image contrast on motion measurements, Strain. 45 (2009) 160-178.

114. Berg AC, Malik, J (2001) Geometric blur for template matching. Proc. 2001 IEEE Computer Society Conference on Computer Vision and Pattern Recognition (CVPR 2001):I-607–I-614.

115. Cantatore A, Cigada A, Sala R, Zappa E (2009) Hyperbolic tangent algorithm for periodic effect cancellation in sub-pixel resolution edge displacement measurement. Measurement 42:1226–1232.

116. International Organization for Standardization (2011) ISO 16610-21:2011 Geometrical product specifications (GPS) – Filtration – Part 21: Linear profile filters: Gaussian filters. ISO, Geneva, Switzerland.

117. P.L. Reu, Experimental and Numerical Methods for Exact Subpixel Shifting, Experimental Mechanics (2011) 51:443–452

118. Aubury M, Luk W (1996) Binomial filters. J VLSI Signal Process 12:35–50.

119. International Organization for Standardization (2008) ISO/IEC Guide 98-3:2008 Uncertainty of measurement – Part 3: Guide to the expression of uncertainty in measurement (GUM:1995). ISO, Geneva, Switzerland.

120. ASTM E8 / E8M - 11 Standard Test Methods for Tension Testing of Metallic Materials

121. Matta F (2008) Industry/University Cooperative Research on Advanced Composite Reinforcement for Concrete: Translating Innovation into Sustainable Engineering Practice. Proc. NSF

International Workshop on the Use of Fiber Reinforced Polymers for Sustainable Structures, Cairo, Egypt, May 22, CD-ROM, pp 13
122. American Concrete Institute (ACI) Committee 440 (2006) Guide for the Design and Construction of Structural Concrete Reinforced with FRP Bars—ACI 440.1R-06. ACI, Farmington Hills, MI
123. Canadian Standards Association (CSA) (2006) Canadian highway bridge design code—CAN/CSA-S6-06. CSA, Mississauga
124. American Association of State Highway and Transportation Officials (AASHTO) (2009) AASHTO LRFD bridge design guide specifications for GFRP-reinforced concrete bridge decks and traffic railings, 1st edn. AASHTO, Washington
125. American Concrete Institute (ACI) Committee 440 (2008) Specification for carbon and glass fiber-reinforced polymer bar materials for concrete reinforcement—ACI 440.6-08. ACI,Farmington Hills, MI
126. American Concrete Institute (ACI) Committee 440 (2008) Specification for construction with fiber-reinforced polymer reinforcing bars—ACI 440.5-08. ACI, Farmington Hills, MI
127. Gross SP, Yost JR, Dinehart DW, Svensen E, Liu N (2003) Shear Strength of Normal and High Strength Concrete Beams Reinforced with GFRP Bars. ASCE Special Publication: Proceedings of the International Conference on High Performance Materials in Bridges and Buildings, Kona, Hawaii, pp 426–437
128. Tureyen AK, Frosch RJ (2003) Concrete shear strength: another perspective. ACI Structural Journal 100(5):609–615
129. Matta F, Mazzoleni P, Zappa E, Sutton A, ElBatanouny M, Larosche A, Ziehl P (2012) Shear strength of FRP reinforced concrete beams without stirrups: verification of fracture mechanics formulation. ACI Special Publication Spring Convention 2012, Dallas, TX
130. Bentz EC, Massam L, Collins MP (2010) Shear strength of large concrete members with FRP reinforcement. J Compos Construct 14(6):637–646
131. Matta F, El-Sayed AK, Nanni A, Benmokrane B (2012) Size Effect on Concrete Shear Strength in Beams Reinforced with FRP Bars. In press ACI Structural Journal
132. A.Nanni, T.M.Hernandez, B.Benmokrane F.Matta, Scaling of strenght of FRP reinforced concrete beams without shear reinforcement, in Fourth International Conference on FRP Composites in Civil Engineering, Zurich, Swizerland, 2008.
133. D. A. Kuchma, K. S. Kim, S. Marks K. H. Reineck, Shear database for reinforced concrete members without shear reinforcement, ACI struct J, vol. 2, no. 100, pp. 240-249, 2003.

134. J. K. Kim, Z.P. Bazant, Size effect in shear failure of longitudinally reinforced beams, ACI Journal, vol. 5, no. 81, pp. 456-468, 1984.
135. Q. Yu Z. P. Bazant, Designing Against Size Effect on Shear Strenght of Reinforced Concrete Beams Without Stirrups: I. Formulation, Journal of structural engineering, December 2005.
136. Q. Yu Z. P. Bazant, Designing Against Size Effect on Shear Strenght of Reinforced Concrete Beams Without Stirrups: II. Verification and Calibration, Journal of structural engineering, December 2005.
137. M. T. Kazemi Z. P. Bazant, "Size effect in diagonal shear failure of beams without stirrups," ACI Struct. J., vol. 3, no. 88, pp. 268-276, 1991.
138. D. Kuchma M. P. Collins, "How safe are our large, lightly reinforced concrete beams, slabs and footings? ," ACI Struct. J., vol. 4, no. 96, pp. 482-490, 1999.
139. E. C. Bentz, and M. P. Collins D. Angelakos, "Effect of concrete strenght and minimum stirrups on shear strenght of large members," ACI Struct. J., vol. 3, no. 98, pp. 290-300, 2001.
140. B Pan, D Wu, Y Xia. An active imaging digital image correlation method for deformation measurement insensitive to ambient light, Opt.Laser Technol. 44 (2012) 204-209.
141. Y Narukawa. White-Light LEDs, Opt.Photonics News. 15 (2004) 24-29.
142. G Dusserre, F Nazaret, L Robert, T Cutard. Applicability of image correlation techniques to characterise asymmetric refractory creep during bending tests, Journal of the European Ceramic Society. 33 (2013) 221-231.
143. JS Lyons, J Liu, MA Sutton. High-temperature deformation measurements using digital-image correlation, Exp.Mech. 36 (1996) 64-70.
144. W Tong. An evaluation of digital image correlation criteria for strain mapping applications, Strain. 41 (2005) 167-175.